# Nanostructured composites as electrochemical catalysts for Li-air batteries

by

Hey Woong Park

A thesis
presented to the University of Waterloo
in fulfillment of the
thesis requirement for the degree of
Doctor of Philosophy
in
Chemical Engineering

Waterloo, Ontario, Canada 2014

# Author's Declaration

This thesis consists of material all of which I authored or co-authored: see Statement of Contributions included in the thesis. This is a true copy of the thesis, including any required final revisions, as accepted by my examiners.

I understand that my thesis may be made electronically available to the public

# Statement of Contributions

I co-authored the work presented in Chapter 4 by contributing to the experimental design and the synthesis of graphene materials to investigate their catalytic activity. In addition, I conducted electrochemical tests to determine of the optimum condition for the catalyst.

I hereby declare that I am the sole author of the rest of this thesis.

# Abstract

Advanced energy conversion and storage systems are drawing tremendous research attention as the energy demand for portable electronics and electric vehicle (EV) applications continues to increase. Although lithium (Li) ion batteries are currently used for various applications, including EVs, these batteries are still unable to fulfill the ultimate driving range requirements. Li-air batteries are an attractive alternative due to their extremely high theoretical energy density; however some technical hurdles remain, including insufficient cycle stability, low energy efficiency and poor rate capability. These challenges are directly related to the sluggish oxygen reduction reaction (ORR) and oxygen evolution reaction (OER), which are the two main reactions that govern the discharge and charge processes, respectively. Therefore, the development of a highly efficient bi-functional catalyst active towards both ORR and OER is a significantly important research area to commercialize Li-air batteries.

In the first part of this study, a facile method which utilizes one-step rapid heating is introduced to synthesize reduced graphene oxide with heterogeneously doped nitrogen atoms (NRGO), with the morphology and nitrogen doping investigated by electron microscopy and x-ray photoelectron spectroscopy, respectively. Electrochemical half-cell experiments show that NRGO has comparable ORR activity to that of state-of-the-art commercial Pt/C catalysts. Next, by combining NRGO synthesized via the facile method with $La_{0.5}Sr_{0.5}Co_{0.8}Fe_{0.2}O_3$ perovskite oxide with a porous rod morphology prepared by electrospinning (LSCF-PR), a novel composite catalyst (LSCF-PR/NRGO) is created. Electrochemical testing of the LSCF-PR/NRGO composite in alkaline medium shows that it has excellent ORR and OER activities, verifying the

effectiveness of the composite for bi-functional activity. These results highlight the importance of morphology on the catalytic activity for metal-air battery applications. Next in the study, one-dimensional carbon nanotube-based composite catalysts have been investigated such as ethylene diamine (EDA)-based nitrogen-doped carbon nanotubes (NCNT) synthesized on RGO, prepared by chemical vapor deposition (CVD). The NCNT/RGO composites exhibit ORR performance similar to that of commercial Pt/C catalysts, with much superior OER activity. Last in the study, a one-pot facile synthetic is developed to prepare advanced bi-functional composite catalysts (op-LN), which combine NCNT and perovskite oxide $La_{0.5}Sr_{0.5}Co_{0.8}Fe_{0.2}O_3$ nanoparticles (LSCF-NP). Electron microscopy confirms that NCNTs are densely grown on the metal oxide. Half-cell experiments show that the synergy of combining LSCF-NP with NCNT yields good bi-functionality towards both ORR and OER, attributed to the synergistic effects arising from the two component species. op-LN has been evaluated in a practical rechargeable Li-air battery and demonstrated superior charge and discharge performance and cycle stability compared to those of LSCF-NP, NCNT and Pt/C. Based on the excellent results, the simple route to prepare op-LN is very attractive for obtaining a highly effective and durable bi-functional catalyst for potential commercialization of rechargeable metal air batteries.

# Acknowledgements

First of all, I have to thank my supervisors, Prof. Zhongwei Chen and Prof. Linda F. Nazar, for their wonderful mentorship, guidance and remarkable support. I was always happy to discuss research with them. Also, I would like to thank my PhD thesis examination committee composed of Prof. Mark Pritzker, Prof. Yuning Li, Prof. Vivek Maheshwari and Prof. Steen Brian Schougaard.

I would like to show my deepest gratitude to my lovely wife Kyong Hwa Jung and children, Jiwon and Jisung and my family in Korea. Without their support, it would have been difficult to complete my degree.

Special thanks to all of my labmates for their support and assistance. I will never forget their kindness and enthusiasm for their research. Furthermore, I would like to express my gratitude to friends Tae-jung Kwon, Sung-ho Park, Hoonsub Song, Hyunki Bae and Youngjae Kim. They made my life in Canada much more enjoyable and unforgettable.

# Table of Contents

# List of Figures

# List of Tables

# 1. Introduction

## 1.1 Introduction

The increasing prices of fossil fuels and the environmental issues associated with the global warming have driven us to look into the development of sustainable energy, such as solar and wind power, and the energy storage and generation systems such as batteries and fuel cells. Although engineers and scientists have made great advances modern technology, the major source of energy is still the old-fashioned combustion of fossil fuels for energy demanding applications. According to a report from U.S. Energy Information Administration, it is anticipated that consumption of the fossil fuel to generate electricity will keep increasing until 2040. The U.S. Environmental Protection Agency reported that one of the major sources of greenhouse emission (GHE) is transportation **(Figure 1.1)**, since conventional energy sources such as combustion engines are mostly used in automotive vehicles. They have contributed to global warming through air pollution, leading to an unnecessary spending in attempts to reduce environmental damage. Moreover, the price of the fuels is projected to only increase due to the limitation of reserves.

The advent of mobile devices has also increased energy consumption, again compelling the development of advanced systems with higher energy density. To date, lithium (Li) ion batteries are attractive energy storage devices for applications such as portable electronic devices, electric vehicles and sustainable energy generation due to their high gravimetric and volumetric

energy densities compared to other alternatives such as lead acid, Ni-Cd and Ni-MH batteries **(Figure 1.2)**.[1-3]

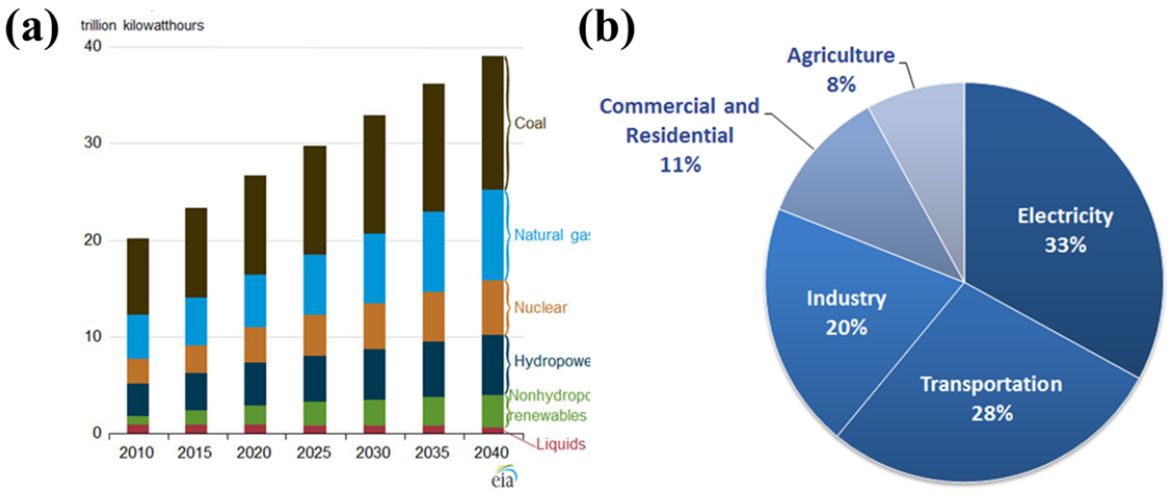


**Figure 1.1** (a) World net electricity generation by energy source, 2010-2040 U.S. Energy Information Administration and (b) total U.S. greenhouse gas emissions by economic sector in 2012 from U.S. Environmental Protection Agency.

However, the materials employed in the current Li-ion batteries, which operate according to an intercalation mechanism, are impendent to increasing energy density and so such batteries do not satisfy the requirements for use in electric vehicles.[4] While it is anticipated that the energy density of future Li-ion batteries may double that of current devices through the use of high voltage and capacity cathode materials and anode alloy materials, this may still not fulfill the requirements for a high-end market. For example, to be competitive for combustion-engine vehicles, the battery should be able to attain a driving range of at least 600 km from the fully charged state. However, it is estimated that future Li-ion batteries will only be able to drive ~

200 km on a single charge **(Figure 1.2)**. Additionally, the cost of the battery system should not be neglected even if the advent of electric vehicles will reduce transportation expenses.

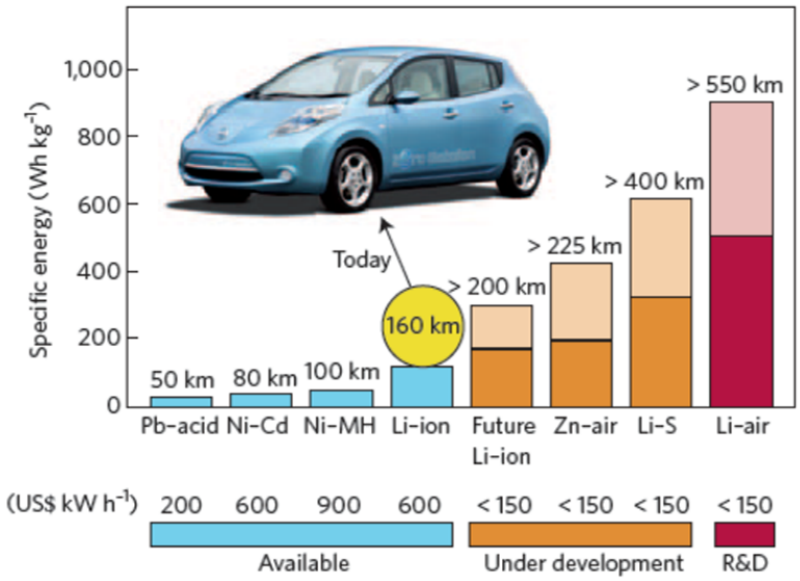


**Figure 1.2** Practical specific energies density for rechargeable batteries. A range of anticipated specific energies density is given as shown by the lighter color on the bars in the chart for future technologies under Research & Development. The driving ranges are based on the minimum specific energy for each technology and scaled according to the specific energy of the Li-ion cells (140 Wh $kg^{-1}$) and driving range (160 km) of the Nissan Leaf. The prices for technologies under development represent goals suggested by the US Advanced Battery Consortium. Reprinted from reference [4].

Alternatively, metal-air batteries technologies have recently attracted much attention as possible alternatives due to their outstanding energy density. **Figure 1.2** shows a comparison of specific energy densities for several types of rechargeable batteries. While the energy density of Li-air batteries remains uncertain due to several fundamental challenges, the estimated practical specific energy density of Li-air batteries can potentially reach up to 900 Wh $kg^{-1}$, which is six

times higher than that of current Li-ion batteries (140 Wh $kg^{-1}$). This energy density will allow the driving range to be extended to more than 550 km. For these reasons, Li-air batteries are regarded as one of the best candidates for future energy source in EV applications as well as a fascinating opportunity for researchers to be innovative in the field of batteries and fuel cells.

Conspicuous characteristics of Li-air batteries that distinguish them from conventional Li-ion batteries are the skeleton and the active cathode material, which allow the inflow of air to utilize oxygen as the source of energy along with Li oxidation. In principle, Li-air batteries are designed such that oxygen is reduced at the cathode as the associated half-cell reaction to combine with electrons produced at the Li metal anode. As a result, the Li-air battery relies on the oxygen reduction reaction (ORR, $O_2 + 2H_2O + 4e^- \rightarrow 4OH^-$ in alkaline medium) to generate the electrical energy, which usually controls its performance due to the slow kinetics during discharge.[1, 3] Oxygen evolution (OER, $4OH^- \rightarrow O_2 + 2H_2O + 4e^-$ in alkaline medium) takes place during charging. OER determines the charging performance due to its sluggish reaction and possible side reactions.[5, 6] To achieve practical performance ORR and OER catalysts in the cathode are essential to speed up the electrochemical reactions and obtain sufficient power and energy. It is worth noting that the reaction potential for OER overlaps that for the corrosion of carbon which is widely used as a catalyst support. Thus stable catalyst support materials must be developed for long-term cycle stability of Li-air batteries.[7]

## 1.2 Motivation

To date, carbon-supported precious metal catalysts such as platinum (Pt/C) and iridium (Ir/C) have demonstrated high electrocatalytic activity toward ORR and OER, respectively, in aqueous electrolytes for energy conversion for large power and energy demand applications.[6, 8-13] However, to commercialize such energy systems, several challenges such as high cost and poor durability need to be addressed.[6] Also, the precious metals are found only in limited areas around the world and current reserves may be insufficient for large scale applications. This is a critical hurdle for widespread application and commercialization of energy technologies for the future. Above all, the critical issue of these state-of-the-art catalysts is their uni-functional catalytic activity toward either ORR or OER, which does not meet the requirement for rechargeable air battery systems. Moreover, using two types of catalysts to achieve effective rechargeable system in the battery makes battery design complicated and increased material costs.[6, 14] To address these issues, advanced catalysts with bi-functional activity towards both ORR and OER and excellent electrochemical durability must be developed. Once such advanced catalysts are developed, they can be used as cost-effective bi-functional catalysts for Li-air batteries.

Carbon-based support materials are vital for oxygen electrochemistry in order to maximize the catalytic activity as found in the state-of-the-art Pt/C and Ir/C catalysts. Thus, the development and application of new materials using supports has been the focus of much research on improving catalytic activity and durability. One-dimensional (1-D) and two-dimensional (2-D) graphitic carbon materials such as graphene and carbon nanotubes (CNT) have been investigated in this study because these materials possess large surface area, relatively

high chemical resistance and high electrical conductivity. In addition to these favorable characteristics, once these graphitic carbon materials are doped with nitrogen, they demonstrate excellent ORR activity in alkaline electrolytes. These advantages are highly encouraging for producing effective nitrogen-doped reduced graphene (NRGO) support and novel bi-functional catalysts through the combination of NRGO with metal oxide catalyst. The role of nitrogen doping in graphitic carbon with metal oxide further motivates the incorporation of NCNT into metal oxide to develop effective bi-functional catalyst via novel engineering methods.

The replacement of precious metal catalysts with effective perovskite oxides is a promising approach for the development of cost-effective and bi-functional catalysts since a number of perovskite oxides have been proposed in the literature as ORR and OER catalysts in alkaline electrolyte.[15-21] According to the previous reports, the appropriate oxidation states of the transition metal in the oxide phase which are associated with substitution by other metal elements enhance the catalytic activities. Suntivich J. et al.[21] suggested the composition of $Ba_{0.5}Sr_{0.5}Co_{0.8}Fe_{0.2}O_3$ (BSCF) as the best catalyst amongst various perovskite oxides in their study and also proposed that a high surface area perovskite oxide could enhance the catalytic activity. This idea has spurred the research to develop another type of perovskite oxide, $La_{0.5}Sr_{0.5}Co_{0.8}Fe_{0.2}O_3$ (LSCF) which has demonstrated remarkable activity, especially for OER. In addition to the optimum composition of the oxide phase, an increase in the surface area of the metal oxide is key to exposing a large number of the active sites to reactants to enhance the overall catalytic activity. In this study, electrospinning has been applied to obtain a homogeneous morphology of the perovskite oxide with large surface area since this technique is expected to facilitate production of one-dimensional porous-structured catalysts. Despite all the possible approaches available to produce bi-functional catalyst of the perovskite oxide so far, catalysis

toward ORR still must be improved while OER activity could reach that possible using the state-of-the-art precious metal catalysts. Therefore, it is worthwhile to incorporate NRGO or NCNT into the perovskite oxide to obtain excellent bi-functional catalyst.

Lastly, a single-cell Li-air battery prototype has been designed and fabricated by the author in order to investigate the performance of the developed catalyst. The realistic performance obtained during this battery testing demonstrates practical catalytic activity utilizing air in ambient conditions and provides clues to better understanding the battery system itself.

## 1.3 Research objectives

The goal of this research is to develop an effective bi-functional catalyst for the oxygen reactions as well as developing a method for synthesis based on perovskite oxide and 1- (1-D) and 2-dimensional (2-D) graphitic carbon such as nanotubes and graphene. The developed catalyst was applied to a practical Li-air battery prototype to characterize catalyst activity and battery performance. The following tasks were completed to achieve the research objectives:

- Proposing facile synthetic method to produce nitrogen-doped RGO (NRGO) from graphite powder and then investigating its characteristics and catalytic activity towards ORR.
- Proposing effective bi-functional composite catalyst that combines the porous rod-structured perovskite oxide synthesized by electrospinning and NRGO, studying the effect of increased surface area of the perovskite oxide and proving the excellent ORR and OER performances of the composite catalyst.

- Investigating the electrocatalytic activities of nitrogen-doped CNTs (NCNT) directly deposited on RGO. In this study, a facile synthesis method to prepare a composite catalyst is proposed and studied the advantages of its novel morphology.
- Proposing a one-pot engineering-friendly synthesis method for bi-functional catalyst which produces a perovskite oxide-NCNT composite and investigating its activity towards the ORR and OER in a half-cell set-up and its performance in a custom-made Li-air battery.

## 1.4. Thesis outline

This thesis consists of 8 chapters organized as follows:

- Chapter 1introduces the present work, its motivation and research objectives.
- Chapter 2 provides the background information on Li-air batteries and material components of this study such as perovskite oxide, graphene and carbon nanotubes.
- Chapter 3 provides descriptions of the experimental procedures including the synthesis methods for the catalysts and testing methods for electrochemical behavior in half-cell set-up. This chapter also includes the physicochemical and electrochemical characterization methods and their operating principles.
- Chapter 4 describes the fabrications of highly active nitrogen-doped graphene nanosheets prepared via extremely rapid heating into efficient ORR catalyst.
- Chapter 5 presents the method to produce electrospun porous perovskite oxide/nitrogen-doped graphene composites as bi-functional catalysts for metal-air batteries

- Chapter 6 focuses on bi-functional nitrogen-doped CNT (NCNT)/graphene composites as highly active and durable electrocatalysts for metal-air battery applications.
- Chapter 7 introduces one-pot synthesis of perovskite oxide-based NCNT composites as bi-functional catalysts for Li-air battery.
- Chapter 8 lastly presents the conclusions of the current study and recommendations for further study to improve the performances of the catalysts.

# 2. Background and Literature Review

## 2.1 Lithium air batteries

Electrochemical energy conversion systems based on metal and oxygen electrochemical reactions, called metal-air batteries, are very attractive because of their unique active cathode material which reacts with oxygen available in the air with virtually unlimited amounts. A few systems with different metal anodes such as Li, Ca, Al and Zn have been proposed and commercialized as a primary battery. According to the operating mechanism, the metal-air battery performance relies on the rates of oxygen reduction and oxidation at the cathode and metal oxidation and reduction at the metal anode, respectively. The half-cell reaction in alkaline medium at the air electrode is expressed as:

$$\mathbf{O_2 + 2H_2O + 4e^- \leftrightarrows \ 4OH^-} \qquad \mathbf{E^0_{cathode} = +0.401V} \tag{2. 1}$$

$E^0_{cathode}$ represents the standard potential of oxygen reduction in alkaline medium versus standard hydrogen electrode (SHE), while $E^0_{anode}$ is variable depending on the metal anode. The oxidation reaction of metal at the anode can be written as:

$$\mathbf{M \leftrightarrows \ M^{n+} + ne^-} \tag{2. 2}$$

where M denotes the metal used for anode and the value of *n* depends on the valence change due to the oxidation of the metal and the standard potential relies on the metal. Since the difference of the theoretical electrode potentials of the cathode and the anode and the valence change (*n*) determine the battery voltage and capacity, respectively, the theoretical cell voltage and energy density depend on the different metal anodes, as summarized in **Table 2.1**. However, the

practical operating voltage and energy density mostly relies on the cathode because its reaction kinetics is much slower than that at the anode.

**Table 2.1** Characteristics of metal-air cells (in alkaline electrolyte).[22]

| Metal anode | Electrochemical equivalent of metal (Ah $g^{-1}$) | Theoretical cell voltage (V) | Valence change | Theoretical specific energy (kWh $kg^{-1}$) |
|---|---|---|---|---|
| Li | 3.86 | 3.4 | 1 | 13.0 |
| Ca | 1.34 | 3.4 | 2 | 4.4 |
| Mg | 2.20 | 3.1 | 2 | 6.8 |
| Al | 2.98 | 2.7 | 3 | 8.1 |
| Zn | 0.82 | 1.6 | 2 | 1.3 |

Li anode is able to deliver the highest energy density since it has the most negative standard reduction potential and the lightest weight. However, the handling of Li anodes to prepare the test batteries needs special care to prevent Li oxidation in the open atmosphere and has compelled researchers to propose several types of battery designs. Based on the architecture of Li-air batteries, they are commonly divided into three types as shown in **Figure 2.1**. These three types of batteries are distinguishable according to the electrolytes used. The electrolytes include (i) a non-aqueous electrolyte, (ii) an aqueous electrolyte, and (iii) a hybrid electrolyte system in which aqueous catholytes and non-aqueous anolytes are used. All three batteries use Li metal as the anode material and a cathode material on a carbon support. On the other hand, Li-air

batteries can be also categorized differently into two types, based on the reaction principles on the cathode. The main difference is that the discharge product in the non-aqueous system is an insoluble insulator $Li_2O_2$, while the aqueous system generates soluble LiOH (in alkaline medium) during discharge.[23] The detailed description of the battery designs will be dealt with in this chapter.

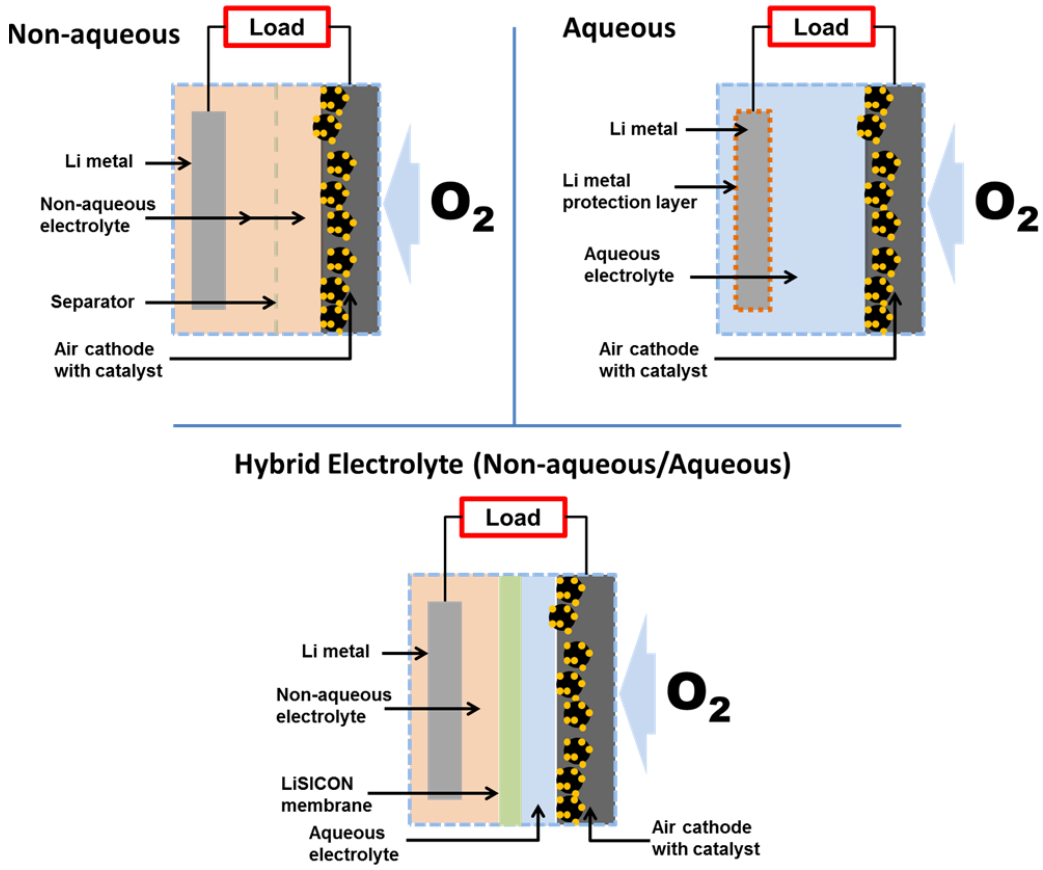


**Figure 2.1** Three different types of Li-air batteries.[2]

### 2.1.1 Non-aqueous Li-air battery

While the operation of a Li-air battery was first demonstrated in an aqueous electrolyte system in 1976 by Galbraith for electric vehicles,[24] Abraham et al. introduced a practical rechargeable Li-air battery using non-aqueous polymer electrolyte in 1996.[25] Later Bruce et al. proposed a viable battery incorporating a non-aqueous electrolyte traditionally used for Li-ion battery prompted the research effort in Li-air batteries as a major stream.[26] Since then, the attention on Li-air batteries has grown rapidly with numerous high impact publications. One significant advantage of a non-aqueous Li-air battery over an aqueous Li-air battery is the formation of a solid electrolyte interphase (SEI). Once a Li metal anode comes into contact with a non-aqueous electrolyte, a SEI is formed on the surface of Li anode, which enables subsequent reactions to occur without any additional protective layer such as a solid electrolyte membrane on the surface of the Li anode.[2, 3, 23] Furthermore, a non-aqueous electrolyte system may not need a specialized membrane to protect Li metal from moisture depending on the battery design.[27]

The configuration of the non-aqueous electrolyte system consists of a Li metal anode, air-cathode material, electrolyte and a separator, which are very similar to the components found in a typical Li-ion battery. The air-cathode is commonly composed of large surface area carbon black and catalyst composites. The role of the cathode is significant because it has to catalyze the ORR and OER to reduce the overpotential of the battery and accommodate as much solid discharge product ($Li_2O_2$) as possible to increase the practical capacity.[28-32] **Figure 2.2** presents a schematic of the reaction and the most recently proposed reaction mechanism of a non-aqueous Li-air battery although the exact mechanism is still under investigation. During discharge, the oxidation of Li metal anode produces $Li^+$ ions ($Li \rightarrow Li^+ + e^-$). The electrons from

the anode travel through the external circuit to the cathode, which combines with the lithium ions from the anode to reduce oxygen thereby forming $Li_2O_2$ on the cathode as a discharge product. The charging process is the in reverse to that of discharging.

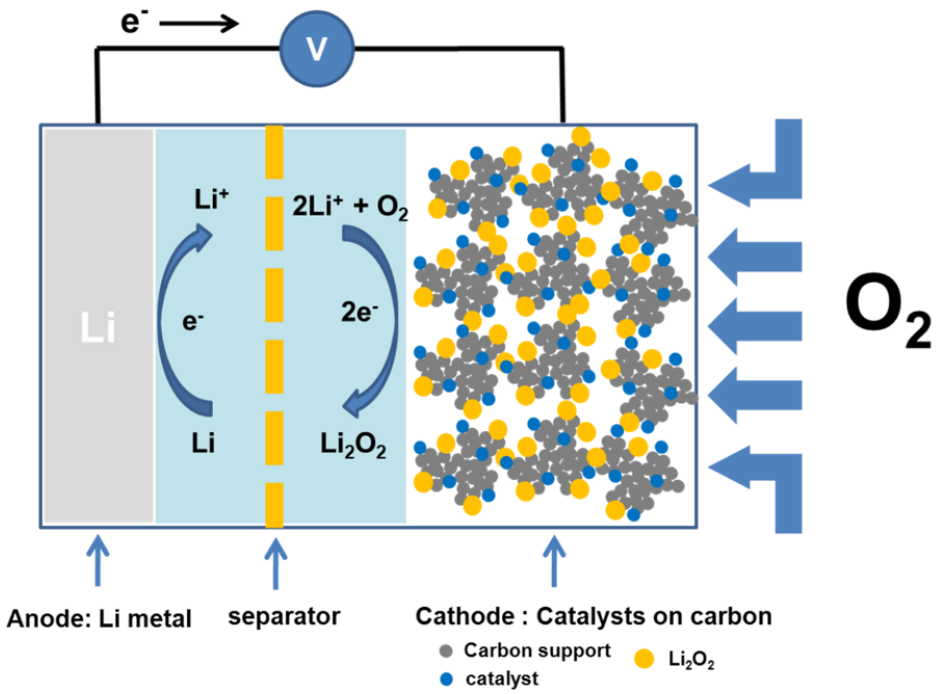


$$\mathbf{Li^+ + e^- + O_2 \rightarrow LiO_2} \quad (2.3)$$

followed by

$$\mathbf{2LiO_2 \rightarrow Li_2O_2 + O_2} \quad \textbf{(disproportional reaction, chemical reaction)} \quad (2.4)$$

or

$$\mathbf{Li^+ + e^- + LiO_2 \rightarrow Li_2O_2} \qquad \mathbf{E^o = 2.96\ V\ vs\ .\ Li/Li^+} \quad (2.5)$$

**Figure 2.2** Schematic view of reaction mechanism of non-aqueous Li-air battery.[3]

Stepwise reactions are involved in oxygen reduction which is the sluggish step in the overall electrochemical process, as shown in the proposed mechanism above. As expressed in equation (2.3), oxygen is first reduced to $O_2^-$ with one electron to form $LiO_2$. This lithium

superoxide disproportionates to $Li_2O_2$ and $O_2$ without an electron transfer reaction as in equation (2.4) or is further reduced to form $Li_2O_2$ as in equation (2.5) following a two electron reduction process. Oxygen can potentially be reduced in a four-electron process generating $Li_2O$; however, this reaction will not be considered due to its lower reduction potential and the difficulty in reversing the reaction.[3, 23]

The development of favorable electrochemical catalysts in a non-aqueous system is important for reducing the overpotential of the ORR and OER.[33, 34] Initially, Bruce and co-workers screened various metal oxide catalysts, and found that α-$MnO_2$ nanowires demonstrated superior cycle durability for 10 cycles due to its crystalline structure.[28, 30] The Shao-Horn et al prepared various novel metal catalysts as well as metal alloy-carbon composites for ORR and OER.[13, 31] Other groups also introduced metal oxides, graphene-based materials including heteroatom-doped graphene sheets, metal oxide/graphene composites as catalysts for non-aqueous Li-air batteries.[35-40] However, all of these catalysts showed insufficient rate capability and lack of cycle stability of their maximum capacity to satisfy the requirement of the ultimate applications. Thus, it is crucial that effective catalysts be found in order to make Li-air batteries feasible.

One of the critical issues of non-aqueous Li-air batteries stems from the electrolyte. As mentioned above, the first reported non-aqueous Li-air battery employed polymer electrolytes based on polyacrylonitrile, ethylene carbonate (EC) and propylene carbonate (PC) with $LiPF_6$ as a salt.[25] Also, other pioneering groups used carbonate-based liquid electrolytes such as EC, PC and diethyl carbonate (DEC) in non-aqueous Li-air batteries.[30, 38, 41] However, recently it was revealed that carbonate-based electrolytes do not produce $Li_2O_2$ primarily, but rather undergo decomposition reactions with superoxide ions to form lithium carbonate ($Li_2CO_3$).[23,

42] Furthermore, instead of evolving oxygen during the charging process, $CO_2$ is generated from the decomposition of the carbonate.[43, 44] This means that the battery does not follow in a stable reversible cycle, and is not rechargeable. In order to avoid the electrolyte decomposition, noncarbonated electrolytes containing ethers, ionic liquid, acetonitrile, etc have been studied.[45, 46] Dimethoxyethane (DME) and tetraglyme (TEGDME), which are ether-based electrolytes, were explored as possible replacements for carbonate-based electrolytes. The discharge product in the ether-based electrolytes has been identified as $Li_2O_2$ by spectroscopic methods. However, during charging in a DME electrolyte, recent reports have claimed that the number of electrons involved in the OER is higher than the desired number of electrons, indicating that the cycling efficiency is low (approx. 60 %).[44] In addition, Freunberger et al. demonstrated that tetraglyme also undergoes electrolyte decomposition during discharge even though the main discharge product is identified as $Li_2O_2$.[47] Alternately, an ionic liquid has been studied; however, its ionic conductivity is too low for the use in a practical Li-air cell. Acetonitrile is also a feasible candidate as an electrolyte as it has been shown to promote reversible oxygen reduction and evolution, but its volatility limits its usage in practical Li-air batteries.

Other challenges to overcome for non-aqueous electrolyte Li-air batteries are that the discharge product deposits on the surface of the cathode form a passive layer and limit the capacity and reaction kinetics of the battery since the discharge product $Li_2O_2$ is an insoluble insulator. This decreases the electrical conductivity of the cathode, and increases the overpotential. Moreover, the discharge product blocks the micropores as well as mesopores of the cathode. The blockage of the cathode by $Li_2O_2$ limits accessibility of reactants such as Li ion and oxygen that are required for the desired reaction as shown in **Figure 2.3**.[23] Therefore, besides developing the electrochemical bi-functional catalysts for ORR and OER, passivation by

the discharge product and electrolyte decomposition must be prevented to improve the cycle stability and energy density of non-aqueous electrolyte Li-air batteries.

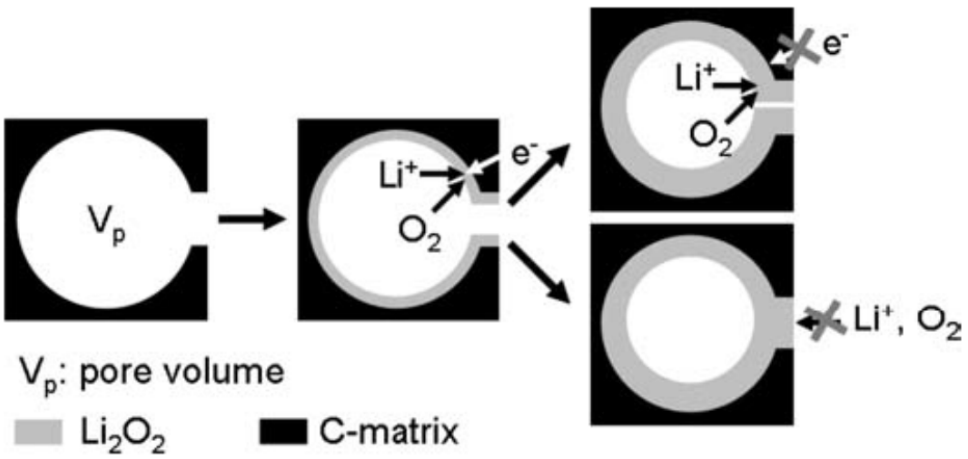


**Figure 2.3** Schematic view of $Li_2O_2$ growing in the pore during discharge. Top right presents cathode passivation by electrical insulation and bottom right indicates pore blocking. Reprinted from reference [23].

### 2.1.2 Aqueous Li-air batteries

The concept of an aqueous Li-air battery was suggested in 2004 by the PolyPlus Battery Company, employing a Li electrode protected by a Li ion conducting ceramic film to prevent the vigorous reaction between Li metal and water.[48] The main advantage of an aqueous Li-air battery (strictly speaking, hybrid electrolyte Li-air battery will be dealt with in this study) is the solubility of the discharge product LiOH in the alkaline electrolyte, contrary to the product of non-aqueous Li-air batteries. However, the management of the discharge product due to its limited solubility, developing a stable separator against both the Li metal anode and aqueous

electrolyte and effective catalysts for ORR and OER for rechargeability still remains critical problems. Zhou and co-workers demonstrated another type of aqueous Li-air battery which consists of both organic and aqueous electrolytes called a hybrid electrolyte Li-air battery. It is worth noting that this battery follows the same ORR and OER mechanisms as in pure aqueous air batteries since the cathode reaction occurs in an aqueous electrolyte while Li metal is oxidized and reduced in organic (non-aqueous) electrolyte during battery operation.[23, 49, 50] The operating principle and chemical reactions of the hybrid electrolyte Li-air battery in detail are shown schematically in **Figure 2.4**.

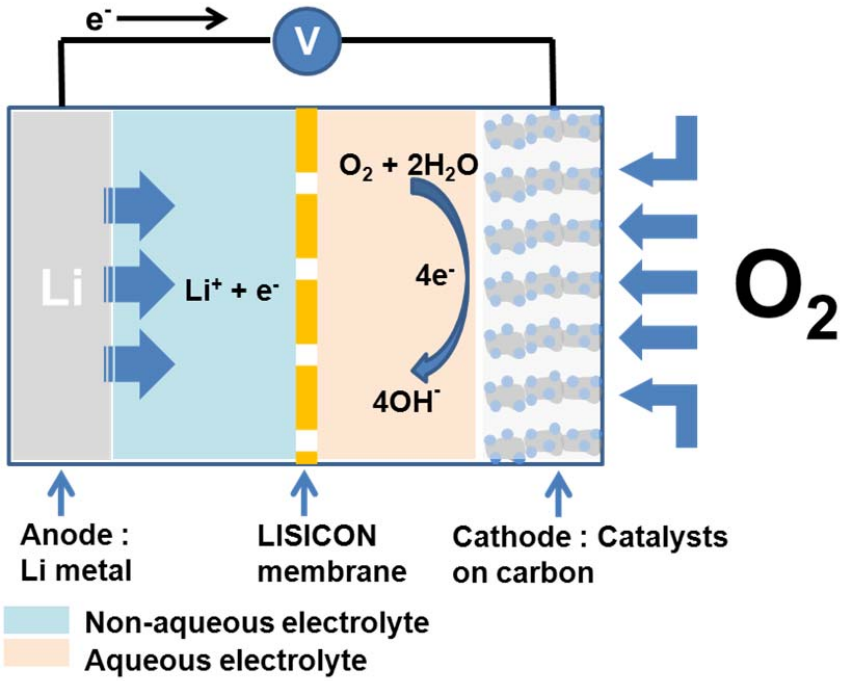


$$\textbf{Positive electrode: } O_2 + 4e^- + 2H_2O \leftrightarrow 4OH^- \qquad E^o = +0.40\ V \qquad (2.6)$$

$$\textbf{Negative electrode: } Li \leftrightarrow Li^+ + e^- \qquad E^o = -3.04\ V \qquad (2.7)$$

$$\textbf{Overall: } 4Li + O_2 + 2H_2O \leftrightarrow 4LiOH \qquad E^o = +3.44\ V \qquad (2.8)$$

**Figure 2.4** Schematic view and reaction mechanism in alkaline media of aqueous (hybrid electrolyte) Li-air battery.[50]

As shown in **Figure 2.4**, the vigorous reaction between metallic Li anode and the aqueous electrolyte can be prevented by employing a lithium superionic conductor (LISICON) film, which also conducts Li ions and remains stable in the aqueous electrolytes. Beyond the LISICON membrane, the most significant component of the battery is the catalyst in the air cathode to reduce the activation barriers for both ORR and OER. This challenge is then the same as in other metal-air batteries since Li metal anode reacts in the organic electrolyte, while the catalytic reduction and evolution of oxygen occurs on the air cathode in the aqueous electrolyte.

In an aqueous Li-air battery, the O-O bond is broken during the discharge process, generating hydroxyl anions ($OH^-$) through the ORR. On the other hand, during the charge process, oxygen is formed by the combination of $OH^-$ through the OER. The mechanism for reduction process involves the following steps:

$$\mathbf{O_2(g) + H_2O(l) + e^- \leftrightarrow OOH^* + OH^-} \quad (2.9)$$

$$\mathbf{OOH^* + OH^- + e^- \leftrightarrow O^* + 2OH^-} \quad (2.10)$$

$$\mathbf{O^* + H_2O(l) + 2OH^- + e^- \leftrightarrow [OH]^* + 3OH^-} \quad (2.11)$$

$$\mathbf{[OH]^* + 3OH^- + e^- \leftrightarrow 4OH^-} \quad (2.12)$$

*: expresses the adsorbed species on the catalyst surface.

As the mechanism of the ORR is complex and depends on catalysts, it has been proposed that two mechanisms occur based on the number of electrons involved in the reaction pathway. One is a four-electron pathway that directly reduces oxygen to $OH^-$; the other is a two-electron pathway, in which oxygen is indirectly reduced to $OH^-$ via the formation of peroxide ($HO_2^-$).[3,

51, 52] It has been reported that the two-electron process is more favorable on mercury, gold, carbon substrates and most transition metal oxide catalysts, while the four-electron process is more dominant in an alkaline electrolyte on precious metals such as Pt and some transition metal oxides.[23] To prevent unwanted effects such as the corrosion of the electrode materials by the peroxide intermediate in the two-electron pathway, the four-electron pathway is highly desirable. Therefore, highly active catalysts, which fulfill the conditions for the four-electron pathway reaction, are required to reduce the overpotential.[3, 23] Developing inexpensive and suitable catalysts beyond the noble metal remains an interesting challenge for researchers to address. An advantage of a rechargeable Li-air battery is in its ability to store energy through the OER, which is the reverse reaction of ORR. In addition to the slow kinetics, the mechanism of OER is still not well understood, making a rechargeable Li-air battery highly intricate and sophisticated system. Jorissen suggested that the OER mechanisms rely on the electrode potential and proposed that the rate determining step is the generation of adsorbed OH radicals on the cathode via oxidation of $OH^-$ on metallic catalysts.[53] On the other hand, the rate determining step on metal oxide catalysts has been reported to be the formation of the intermediate $H_2O_2$.[54] While Pt catalyst is widely known as the most effective catalyst for ORR, ruthenium (Ru) and iridium (Ir)-based catalysts have been introduced as the best OER catalysts.[55, 56] This might be an indication that for rechargeable Li-air batteries to be feasible, separate ORR and OER catalysts may need to be utilized in the air cathode. However, the presence of two different types of catalyst in a single cathode may create unwanted complexity in the battery system. Although some reports have suggested that an alloy of precious metals may be a suitable bi-functional catalyst,[13] the catalyst may be too expensive for commercialization. Moreover, most metal and metal oxide catalysts have been practically utilized in combination with carbon black supports to

improve the electrical conductivity and reduce the amount of catalyst loaded into the electrode. However, the potential during OER is high enough to cause carbon corrosion which adversely affects its rechargeability. Therefore, developing inexpensive and effective catalysts and robust carbon supports for practical usage in a multitude of applications still remain as urgent and active research areas.

**Table 2.2** shows a comparison between two different types of Li-air batteries. Aqueous Li-air battery system has a number of electrochemical advantages. First, the reaction kinetics is faster due to the higher ionic conductivity of the electrolyte and the soluble discharge product. Second, the standard reaction potential of the cathodic reaction in aqueous electrolyte is higher, resulting in higher power produced by the battery. Third, the aqueous system can utilize oxygen directly from air rather than from an installed oxygen reservoir which results in significant decrease in the energy density of the total battery system. Therefore, despite their own challenges (e.g. developing practically effective LISICON membrane), aqueous Li-air batteries are more promising for the next generation of energy systems. Hence the focus of the research is on the development of bi-functionally active electrocatalyst towards both ORR and OER in aqueous media.

**Table 2.2** Summary and comparison of the two types of Li-air batteries

| | Non-aqueous Li-air battery | Aqueous Li-air battery |
|---|---|---|
| Standard cell voltage | 2.96 V | 3.43 V |
| Discharge product | Insoluble $Li_2O_2$ | Soluble LiOH (or $LiOH \cdot H_2O$) |
| Oxygen source | Oxygen reservoir | Atmospheric air |
| Cell design | Relatively easy | Complication due to Li metal protection and LISICON membrane |

## 2.2 Nanostructured electrocatalysts for oxygen reactions

### 2.2.1 Perovskite oxide catalyst

Transition metal-based oxide materials have been explored for electro-catalytic reactions due to their favorable catalytic performances involved oxygen. Early transition metals such as Mn, Fe, Co and Ni have multiple oxidation states, forming various oxides with different crystal structures.[1] These different structures and oxidation states of the transition metal oxides give opportunities for researchers to investigate their electro-catalytic activities for the ORR and OER.

Among the metal oxide catalysts, perovskite oxides have received attraction in the field of electrocatalysis due to their interesting intrinsic properties. The standard molecular formula consists of $ABO_3$ in which A site is occupied by a rare-earth metal ions and B site is occupied by transition-metal ion **(Figure 2.5)**. The compounds can be tailored by partial substitution with other metal ions to improve their catalytic activity by forming $AA'BB'O_3$ perovskite oxides. In addition, oxygen vacancies in perovskite oxides influence catalytic activity for ORR and OER. Generally, when a cation of A or B site in perovskite oxides are partially substituted by lower valence cations (i.e. La is replaced by Sr), oxygen ion vacancies in the lattice are formed to keep the electrical neutrality of the crystal.[57] Zhou et al.[58] reported the increased oxygen vacancy in perovskite $(Ba_{0.5}Sr_{0.5})_{1+x}Co_{0.8}Fe_{0.2}O_{3-\delta}$ could facilitate the oxygen adsorption process which finally enhanced the catalytic activity for ORR. Du et al.[59] studied a facile strategy to improve the electrocatalytic activity of perovskite $CaMnO_3$ by introducing oxygen defects. The nonstoichiometric $CaMnO_{3-\delta}$ ($0 < \delta \leq 0.5$) was synthesized via thermal reduction of pristine perovskite oxide. The nonstoichiometric $CaMnO_{3-\delta}$ with $\delta$ close to 0.25 and an average Mn valence close to 3.5 displayed the highest ORR activity from electrochemical tests. Furthermore, density functional theory (DFT) studies and electrical conductivity measurement demonstrated increased ORR kinetics upon $\delta$ value optimization, which is attributed to facilitated oxygen activation and enhanced electrical properties. Other attractive properties include their relatively high electrical conductivity, defect structure and good cation ordering which provide disorder-free channels of oxygen vacancies to enhance the mobility of oxygen ions. These properties benefit electrocatalysis for ORR and OER in energy conversion systems. Recently, trends in ORR and OER activities of perovskite materials have been introduced correlating to the electron occupation in the $e_g$ orbital of transition metals and transition metal-oxygen covalency as

'activity descriptor'.[15, 21] The research found a relationship between experimental ORR activity and the number of d-electrons of B cation. This revealed that a B cation with a configuration of $d^4$ and $d^7$ of B cation could obtain maximum catalytic activity for ORR according to the 'M' shape trend as shown in **Figure 2.6(a)**. This volcano shape trend can be presented in terms of the number of $e_g$ electrons in B ion **(Figure 2.6(b))**. Conclusively, this correlation revealed that anion with ~ 1 $e_g$ electron has the maximum ORR activity. In addition, increasing the covalency of the metal 3d orbital and oxygen 2p orbital should also improve ORR activity. Researchers claimed that some perovskite oxides could have comparable ORR activity to that of state-of-the-art Pt/C catalysts in alkaline media. However, most of the reports on ORR catalysts with perovskite oxides have indicated that their performance is still inferior to that of precious catalysts.[17, 20, 60]

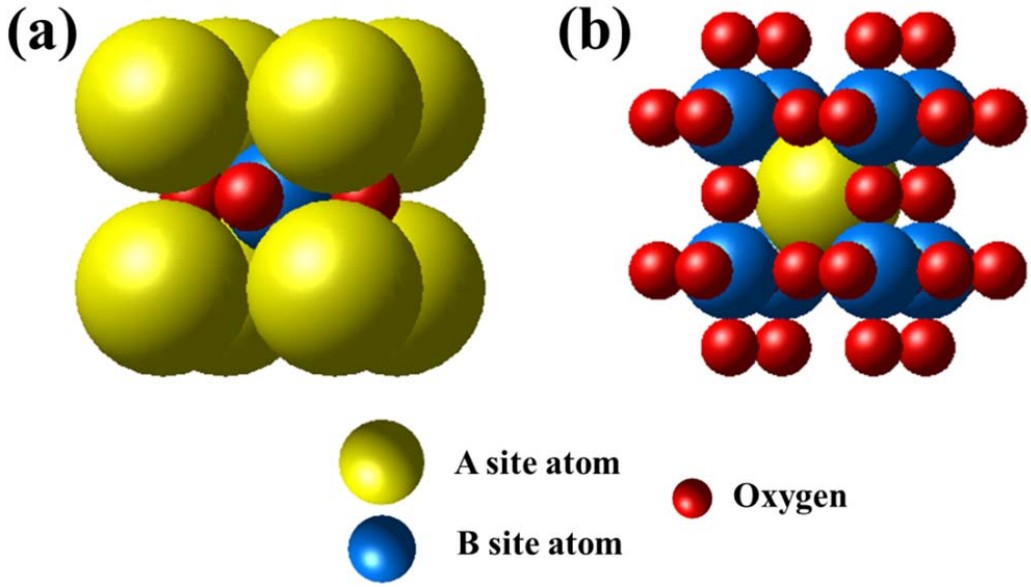


**Figure 2.5** The structure of an $ABO_3$ perovskite oxide with the origin centered at (a) the B-site atom and (b) the A-site atom.

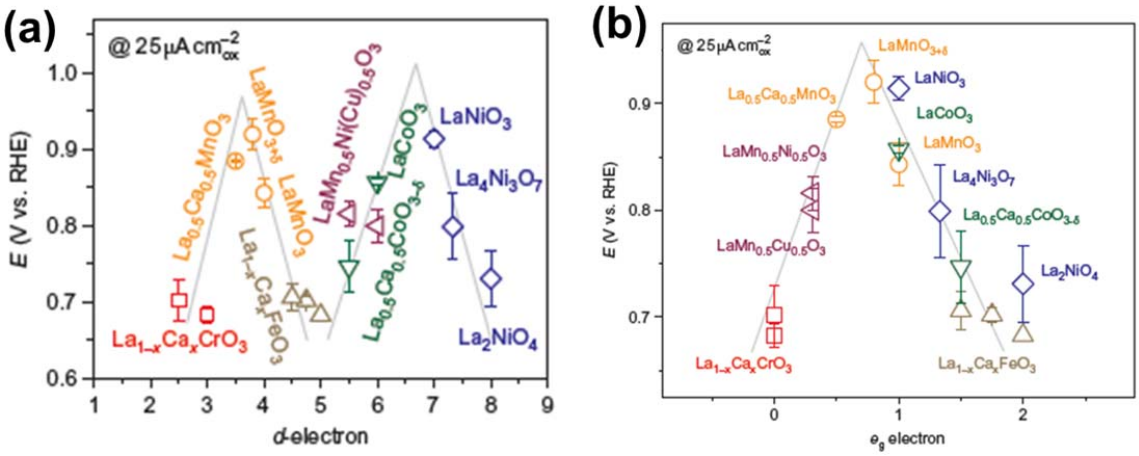


**Figure 2.6** ORR potentials at 25 mA $cm_{ox}^{-2}$ of (a) a function of d-electron number and (b) a function of the number of $e_g$ orbital electron in perovskite-based oxides. Reprinted from reference [15].

Another report from the same group also demonstrated that the OER activity of perovskite oxides, follows a similar volcano-shaped dependence on the $e_g$ occupancy of surface transition-metal cations in an oxide **(Figure 2.7)**. They suggested that an $e_g$ occupancy close to unity with high covalency of B-site metal-oxygen bond leads to the best OER performance. Lastly, based on this principle approach and experimental results, $Ba_{0.5}Sr_{0.5}Co_{0.8}Fe_{0.2}O_3$ was proposed to be the best OER electrocatalyst among the perovskite oxides tested in the study emphasizing enlargement of catalyst surface area is an important factor to enhance its activity. These design principles suggest that the perovskite family can be a highly efficient bi-functional catalyst for the ORR and OER in alkaline media.

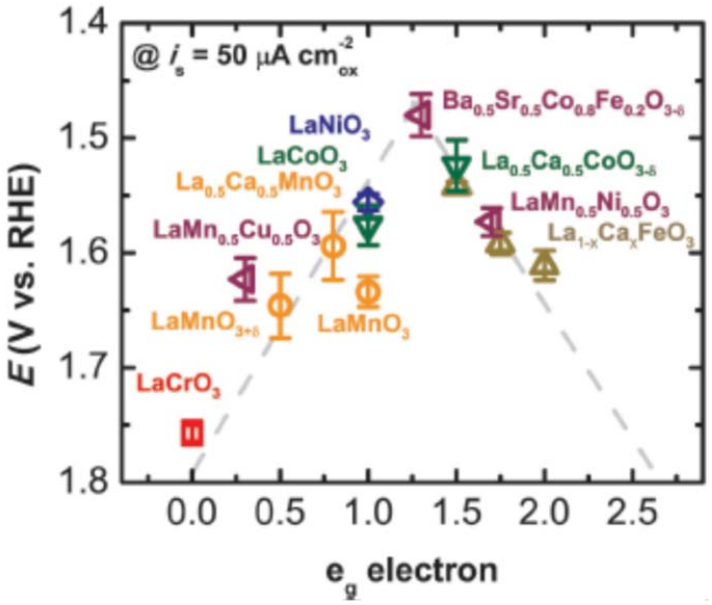


**Figure 2.7** The relation between OER catalytic activity as defined by the overpotential at 50 μA $cm_{ox}^{-2}$ of OER current, and the occupancy of the $e_g$-symmetry electron of the transition metal (B in $ABO_3$). Data symbols vary with type of B ions (Cr, red; Mn, orange; Fe, beige; Co, green; Ni, blue; mixed compounds, purple), where x = 0, 0.25, and 0.5 for Fe. Reprinted from [21].

In addition to the research on the effect of the composition of perovskite oxides on their activity, the effect of morphology has been investigated to prepare high surface area perovskite oxides. Xu et al.[18] prepared porous $La_{0.75}Sr_{0.25}MnO_3$ nanotubes of perovskite oxide by electrospinning and studied their catalytic activities in non-aqueous for Li-oxygen batteries. They used the electrospinning method to prepare novel perovskite oxide with large surface area, as shown in **Figure 2.8**. They obtained the synergistic results of high catalytic activity and the unique hollow channel structure that improved specific capacity, superior rate capability and good cycle stability during ORR and OER in organic for Li-oxygen batteries. In addition, the same research group recently introduced a 3-D ordered macroporous $LaFeO_3$ (3DOM-LFO) catalyst which enhanced rate capability and cycle stability in non-aqueous electrolytes for Li-

oxygen batteries **(Figure 2.9)**.[61] They first prepared close-packed template of the polystyrene (PS) beads, and then incorporated the precursor for LFO into the template. After calcination, the PS template was burned away to leave behind interconnected LFO walls with a porous and ordered 3-D structure. This work also highlighted the synergy between high surface area and catalytic activity. However, the catalytic activity was investigated only in non-aqueous media in which the mechanism for oxygen catalysis is different from that in aqueous media. These catalysts should be examined in aqueous media as well in the future.

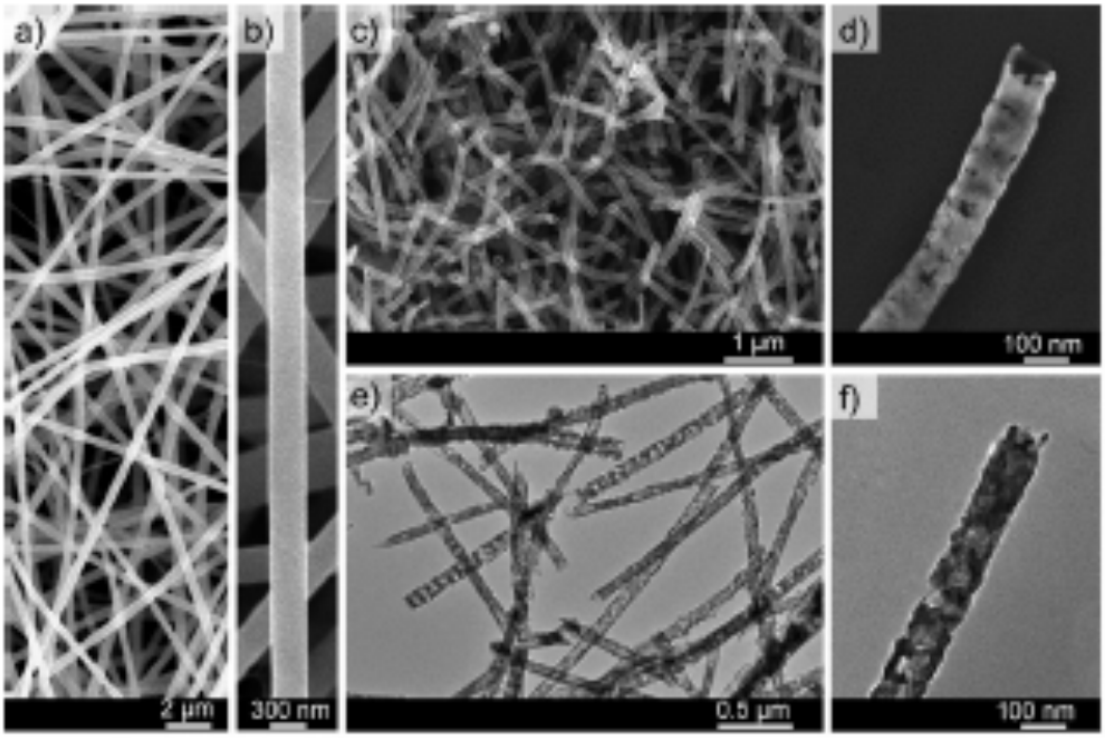


**Figure 2.8** FESEM images at different magnifications. a,b) As-electrospun composite fibers and c,d) PNT-LSM after calcination at 650 $^{o}$C for 3 h. e) Low- and f) high-magnification TEM images of PNT-LSM. Reprinted from reference [18].

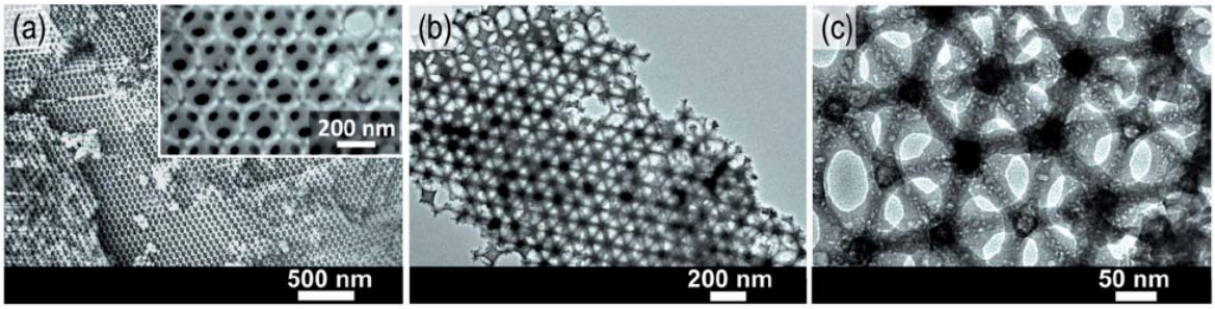


**Figure 2.9** (a) FE-SEM images of 3DOM-LFO. Inset in (a): magnified FE-SEM image. (b) Low-resolution and (c) higher-resolution TEM images of 3DOM-LFO catalyst. Reprinted from reference [61].

Zhao et al.[17] introduced mesoporous perovskite $La_{0.5}Sr_{0.5}CoO_{2.91}$ (LSCO) nanowires by a multistep microemulsion method, demonstrating ORR and OER catalytic activities in both alkaline and organic electrolytes. **Figure 2.10** presents a transmission electron microscope (TEM) image showing the porous morphology and the ORR and OER activities of the mesoporous LSCO nanowires in 0.1 M KOH electrolyte. This confirms the enhanced bi-functional activity by morphology dependence although its intrinsic ORR activity in the alkaline electrolyte as demonstrated in the paper was not impressive compared to other types of catalysts.[62, 63]

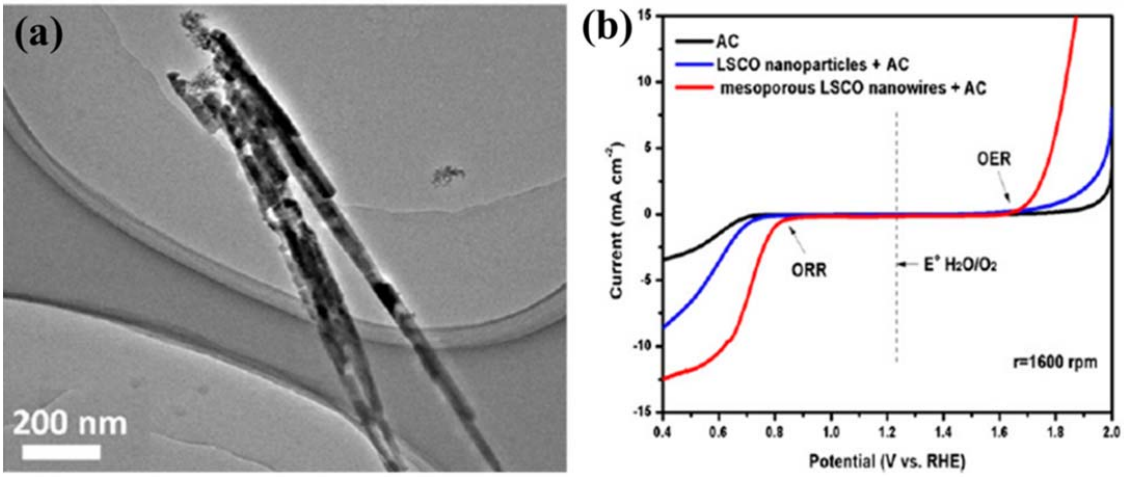


**Figure 2.10** (a) TEM image of the mesoporous LSCO nanowires and (b) ORR and OER polarization curves of acetylene carbon (AC), LSCO nanoparticles + AC, and hierarchical mesoporous LSCO nanowires + acetylene carbon (AC) on glassy carbon electrodes at 1,600-rpm rotation rates. Reprinted from reference [17].

Due to the poor electrical conductivity of metal oxides, the mechanical or chemical blending with carbonaceous materials causes a dramatic improvement in the electro-catalytic activities. One of the well-developed approaches is the preparation of hybrid materials in which metal oxides are well mixed with high surface area and conductive carbon materials (This will be discuss more in subsequent chapters). Metal oxides such as $Co_3O_4$, $MnO_2$, $CoMn_2O_4$ and $MnCo_2O_4$ supported on graphene-based materials have recently been introduced and shown to have superior and synergetic effects on oxygen catalysis in alkaline medium.[39, 40, 64, 65] According to the published reports, further research in combining metal oxide catalysts including perovskites with carbon nanomaterials such as graphene and carbon nanotube is worthwhile to develop highly active and stable bi-functional catalysts.

### 2.2.2 Graphene

Graphene is a single atomic layer of $sp^2$-bonded aromatic carbon material. It is the most recently discovered single-layered carbon material amongst the allotropes such as fullerene and carbon nanotubes.[66, 67] Graphene has drawn significant attention in recent years because of its extraordinary electrical conductivity (~ 2000 S $cm^{-1}$, depending on synthesis methods), high surface areas of ~ 2600 $m^2$ $g^{-1}$, chemical stability and a unique 2-D nanostructure.[68] In addition, graphene is not only considered as the 'mother material' for all graphitic carbon materials and graphite itself **(Figure 2.11)**, but it also possesses superior properties to the allotropes as summarized in **Table 2.3**.[68, 69] Graphene and modified graphene have been exploited in a variety of research areas for diverse applications with the emphasis on the utilization of its unique properties. While its electrocatalytic effects and implementation in batteries are the focus of this project, the versatility of graphene is reflected in the studies in other fields such as optoelectronic devices, electrode materials, supercapacitors, sensors, biomedical devices, and so on.[67]

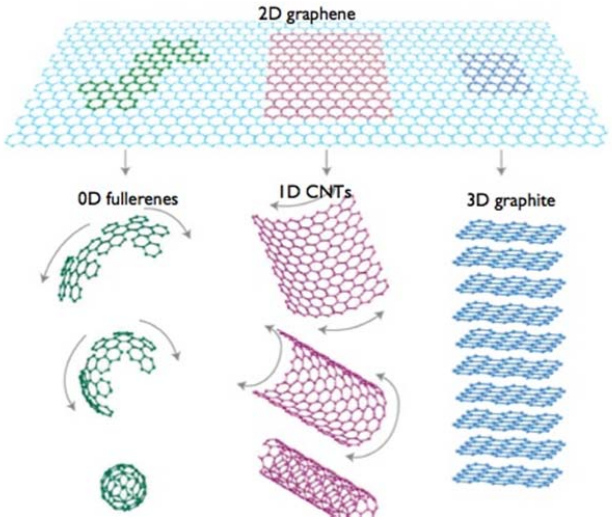


**Figure 2.11** Allotropes of carbon from the conversion of graphene. Reprinted from reference [70].

**Table 2.3** The properties of carbon allotropes.[68, 69]

| Carbon allotropes | Graphene | Graphite | Fullerene | Carbon nanotubes | Diamond |
|---|---|---|---|---|---|
| Carbon hybridization | $sp^2$ | $sp^2$ | $sp^2$ | $sp^2$ | $sp^3$ |
| Dimension | Two | Three | Zero | One | Three |
| Specific surface area ($m^2\ g^{-1}$) | ~ 2600 | ~ 10-20 | 80-90 | ~ 1300 | 20-160 |
| Thermal conductivity ($W\ m^{-1}\ K^{-1}$) | 4840-5300 | 1500-2000 | 0.4 | 3500 | 900-2320 |
| Electronic properties | Semimetal, Zero-gap semiconductor | Conductor | Insulator | Metallic and semiconducting | Insulator, semiconductor |
| Electrical conductivity (S cm-1) | ~ 2000 | $3 \times 10^4$ | $10^{-10}$ | Structure-dependent | |

Graphene can be prepared by various methods such as chemical vapor deposition (CVD), mechanical exfoliation, oxidation and reduction of graphite, and liquid-phase exfoliation of graphite. It should be noted that in real situations, a few layers of aromatic carbons are normally form instead of a single layer of aromatic carbon. This is because obtaining only a single layer of carbon during the synthesis is difficult due to a re-stacking property. For this reason, aromatic carbons with a few layers are generally called 'graphene' in many areas. Amongst different methods, the synthetic route of oxidation of graphite and its subsequent reduction is widely used because a relatively large amount of graphene can be obtained. This type of graphene is called reduced graphene oxide (RGO) based on the reaction mechanism for its synthesis. A schematic diagram of a common synthetic route for large-scale exfoliated reduced graphene sheets is presented in **Figure 2.12**: (i) chemical oxidation of graphite to graphite oxide (GO), and (ii) exfoliation and reduction of GO for conversion into graphene sheets. Graphite oxide (GO) can be reduced to graphene by either chemically exposing GO to reducing agents such as hydrazine and $NaBH_4$, rapid heating at a high temperature (thermal annealing method) or the combination of these two processes.[71, 72] The thermal annealing process for the conversion of GO into graphene will be discussed in detail here as this method is primarily used for this project. Thermal annealing is a facile method to reduce and exfoliate GO into graphene simply by exposing it to heat.[66] The mechanism involves CO and/or $CO_2$ evolution from the oxygen groups on GO and results in simultaneous exfoliation and reduction. The rapid increase in temperature causes the evolution of the gases which produce high pressure and expand the sheets of graphene. This methodology is a simple and effective strategy to produce large amounts of graphene; however, it can also produce RGO with broken sheets during the removal of the

oxygen groups and lead to the formation of defects and edge sites in the aromatic carbon network that slightly lower its electrical conductivity.

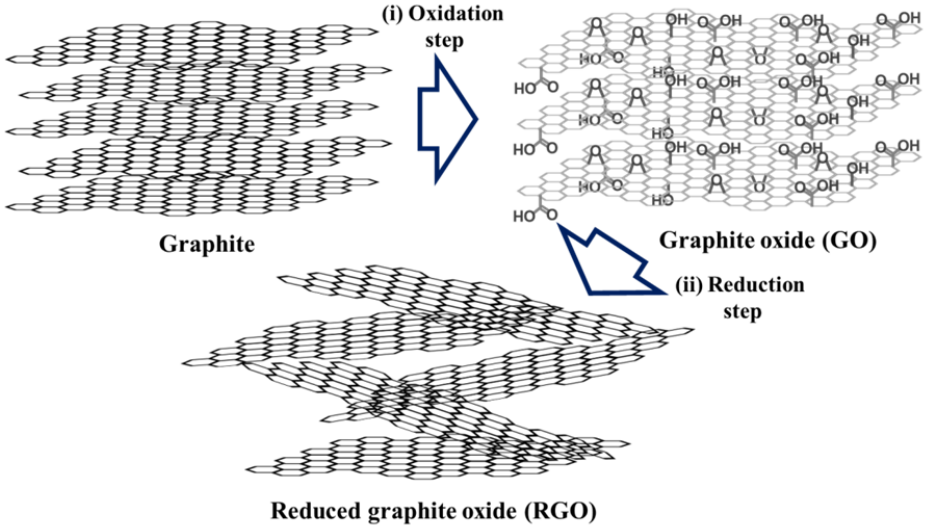


**Figure 2.12** Schematic diagram of graphene synthesis through chemical oxidation and reduction method.[73]

For electrochemical catalyst applications, graphene is employed as a support material for precious metal catalysts or metal oxide catalysts to compensate for their inferior electrical conductivity since graphene is not only chemically and mechanically stable, but also possesses large surface areas with high electrical conductivity. In addition, it can help to control the growth of metal and metal oxide nanoparticles. Graphene was first exploited as a precious metal catalyst support such as Pt/RGO, Pd/RGO, Pt-Co/RGO, etc due to its beneficial properties including chemical resistance, electrical conductivity and large surface area.[10, 74] For example, Choi et al produced Pt nanoparticle-deposited graphene nanosheets (GNS) for a fuel cell catalyst **(Figure 2.13)**, that was compared with conventional Pt/C catalyst.[75] TEM images demonstrated Pt particles with 1.8 nm mean size homogeneously dispersed on GNS is similar to that of the

commercial Pt/C catalyst. The report also suggested that even higher Pt loading could keep uniform particle size on GNS while the Pt particle size with the same content on a carbon black support becomes larger with non-uniform particle size distribution, indicating that the GNS could benefit the formation of homogeneously dispersed Pt nanoparticles at high loadings. In addition, cyclic voltammetry (CV) was conducted to calculate the electrochemical by active surface (EAS) area of the catalyst in acidic medium. As shown in **Figure 2.14**, the hydrogen peak currents normalized by Pt unit mass indicates the electrochemical activity of Pt/GNS catalysts are much better than that of Pt/C. It confirms that the GNS support can enhance the catalytic activity of precious metal catalysts.

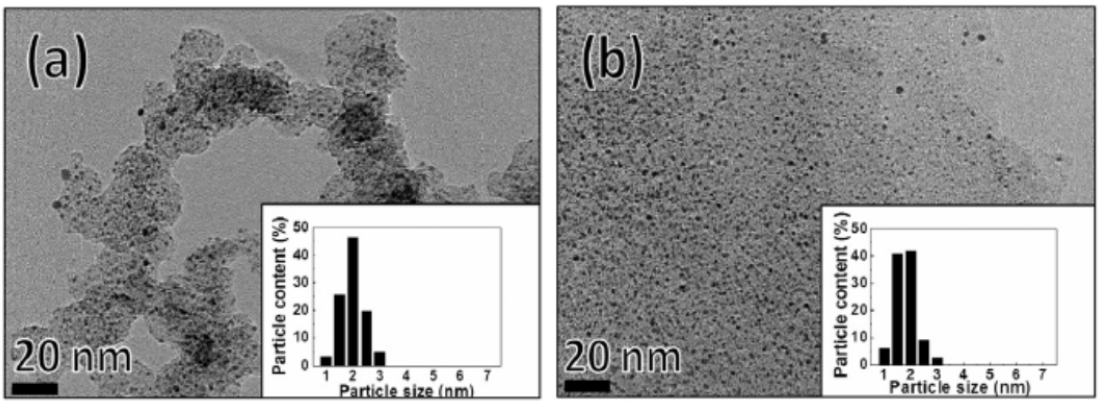


**Figure 2.13** Representative TEM images of the (a) 40 wt.% Pt/C and (b) 40 wt.% Pt/GNS catalysts and their the particle size distributions of the metal nanoparticles. Reprinted from reference [75].

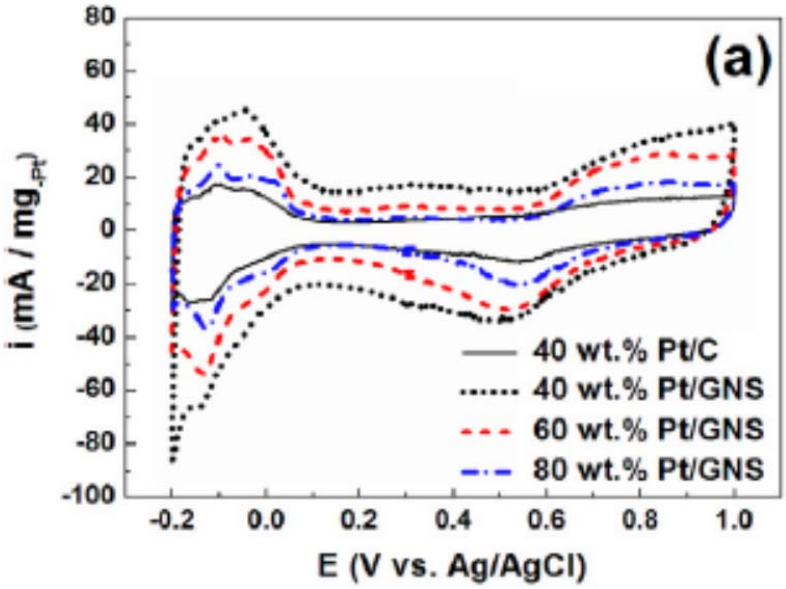


**Figure 2.14** CVs of the Pt/GNS catalysts with differing amounts of Pt metal , from 40 to 80 wt.%, in a $N_2$ saturated 0.5 M $H_2SO_4$ electrolyte solutions at a scan rate of 50 mV $s^{-1}$ from 0.2 to 1.0 V at room temperature. Reprinted from reference [75].

Graphene has also been employed as an electrocatalyst since not only the defect and edge sites present active sites for electrocatalysis, but its unique porous structure helps to accommodate the electrolyte and oxygen to lead to effective catalytic reactions. Moreover, doping heteroatoms such as boron (B), nitrogen (N) or sulphur (S) into graphene provides electrocatalytic active sites to improve the catalytic performance in an alkaline electrolyte.[76-79] Particularly, N-doped graphene has been investigated by many research groups due to its superior activity. Qu et al. synthesized N-doped graphene by a high temperature chemical vapor deposition (CVD) method using ammonia ($NH_3$) and methane ($CH_4$) gases and characterized its the morphology by TEM and confirmed the presence of nitrogen by XPS **(Figure 2.15(a) and (b))**.[80] This N-doped graphene demonstrated superior or comparable ORR activity to that of pristine graphene and Pt/C catalyst in alkaline electrolyte **(Figure 2.15(c))**. Additionally, they

demonstrated long-term stability, tolerance with other energy sources such as methanol and a greater resistance to poison gas than Pt/C in alkaline electrolyte.

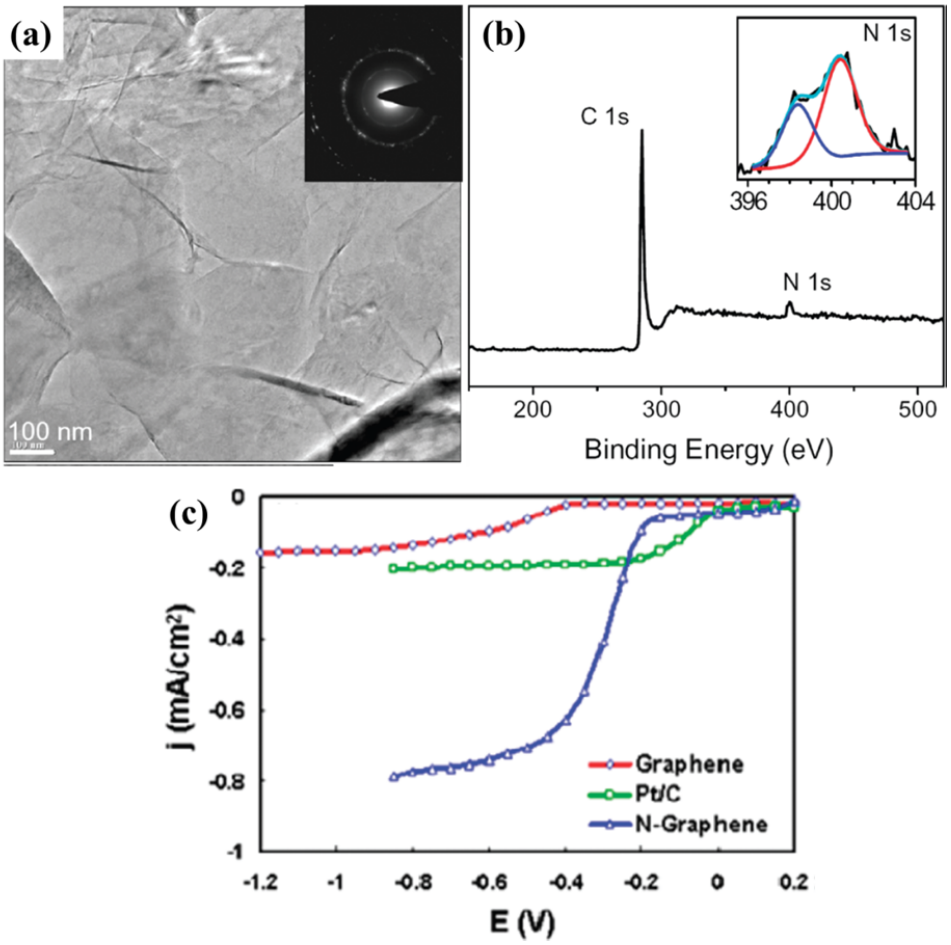


**Figure 2.15** (a) TEM image showing the CVD grown N-doped graphene film. Inset shows the corresponding electron diffraction pattern. (b) XPS spectrum for the as-synthesized N-graphene film. Inset shows the high-resolution N 1s spectrum. (c) RRDE voltammograms for the ORR in air-saturated 0.1 M KOH at the pristine graphene electrode, Pt/C electrode, and N-doped graphene electrode. Reprinted from reference [80].

In addition to the investigation of the hetero-atom doped graphene for oxygen catalysis, Zhou et al. demonstrated electrocatalytic effects of pristine graphene in an alkaline electrolyte for

Li-air batteries.[81] They suggested that the defect and edge sites are active for the electrochemical reactions and two-dimensional morphology of graphene also facilitates oxygen accessibility to the electrode resulting in performance improvement, as described in **Figure 2.16(a)**. In addition, heat-treated graphene provides superior cycle stability due to fewer defect sites and functional groups on graphene, while its catalytic activity is poorer than that of pristine graphene **(Figure 2. 16(b) and (c))**.

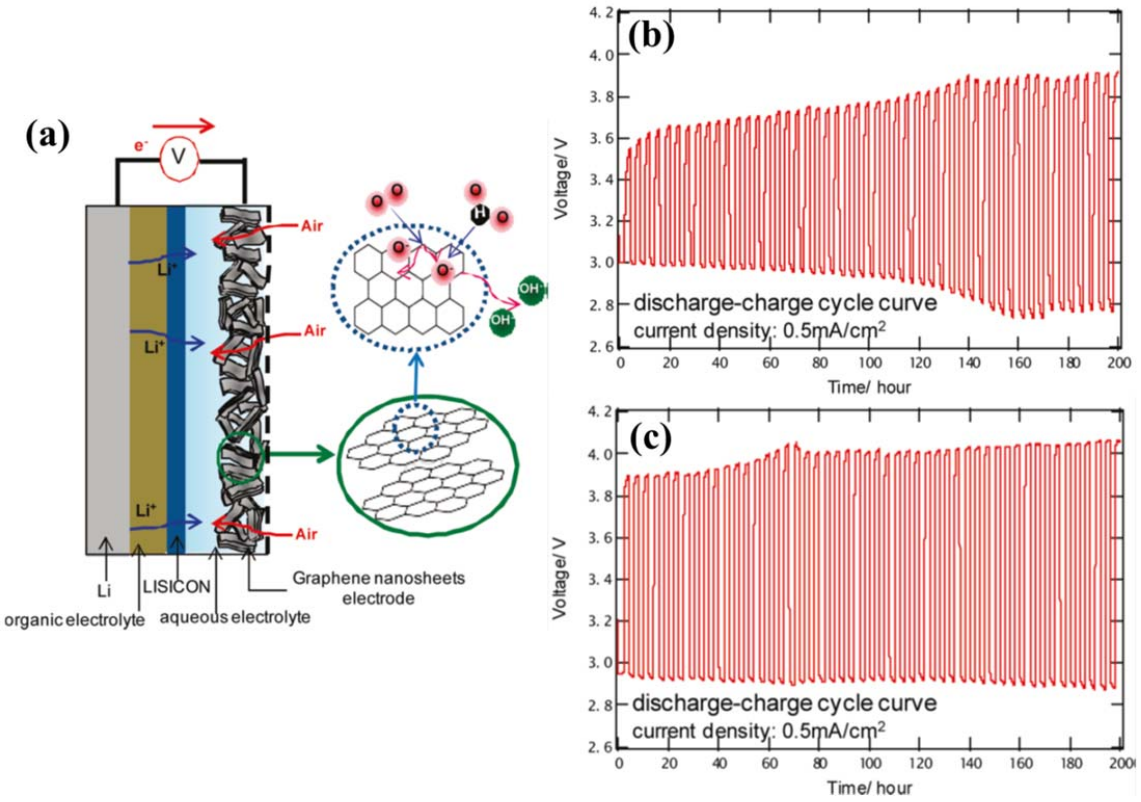


**Figure 2.16** (a) Structure of the rechargeable Li-air battery using graphene nano-sheets as a catalyst. Charge-discharge curves of (b) GNS and (c) heat-treated GNS obtained at a current density of 0.5 mA $cm^{-2}$ cycles. Reprinted from reference [81].

Furthermore, Sun et al. examined the catalytic activity of graphene materials for use in a non-aqueous electrolyte.[37, 38] They proposed that the unique porous morphology of graphene enhanced oxygen diffusion and electrolyte wetting, resulting in an improvement of the catalytic performance. Through further study, they also suggested that the defects and functional groups created by nitrogen doping in graphene allowed it to out-perform pristine graphene in a non-aqueous electrolyte, similar to its behavior in an aqueous electrolyte. Lastly, graphene has been utilized as a support for metal oxides to develop a promising catalyst composite for metal-air battery applications.[39, 40, 65, 82] According to the reports, graphene plays a significant role in the composite as it possesses catalytic activity as well as excellent electrical conductivity, and is able to control the morphology, size and distribution of the oxide nanoparticles. The metal oxide and graphene composites are potentially outstanding bi-functional catalysts for the ORR and OER in metal-air batteries.

### 2.2.3 Carbon nanotubes (CNT)

As introduced in the previous part, carbon nanotubes (CNT) consist of rolled-up graphene sheet(s) into one-dimension (1-D). The novel morphology and structure of CNTs have attracted material scientists due to their nanometer size and unique properties. Simply, CNTs can be divided in two types: single-walled CNTs (SWCNT) and multi-walled CNTs (MWCNT) based on the number of graphene layers making up the tube. In terms of electronic properties, MWCNTs are considered metallic conductors while SWCNTs are a blend of metallic and semiconducting materials, depending on their geometrical atomic structure.[83] Moreover, the

nature of 1-D CNT enables electrons to be conducted without scattering so that no heat is dissipated. Other interesting characteristics are its high accessible surface area chemical stability and thermal stability. Since many reports have proposed that CNTs are suitable supports to enhance the catalytic activity and the performance of fuel cells and metal-air batteries, surface-modified CNTs have been utilized to support a wide variety of noble and non-precious metal oxide catalysts.[6, 84] The first study compared by electrocatalytic activity of Pt supported on MWCNT (Pt/MWCNT) with commercial Pt supported on Vulcan carbon (Pt/C) in fuel cells.[85] Accelerated electrochemical tests were conducted to investigate polarization losses and electrochemical behavior. In comparison with Pt/C, Pt/MWCNT catalysts exhibited higher active area, stable interfacial charge transfer resistance and a decelerated degradation of the performance, as shown in **Figure 2.17**. It was confirmed that the higher corrosion resistance of MWCNTs and stronger interaction with the Pt nanoparticles enhanced performance since catalyst site loss was known to be the main contributor to higher overpotentials. Furthermore, the high corrosion resistance of MWCNT in the cathode catalyst layer helped maintain the electrode structure and its hydrophobicity prevented severe water flooding for a long period when subjected to continuous anodic potential.

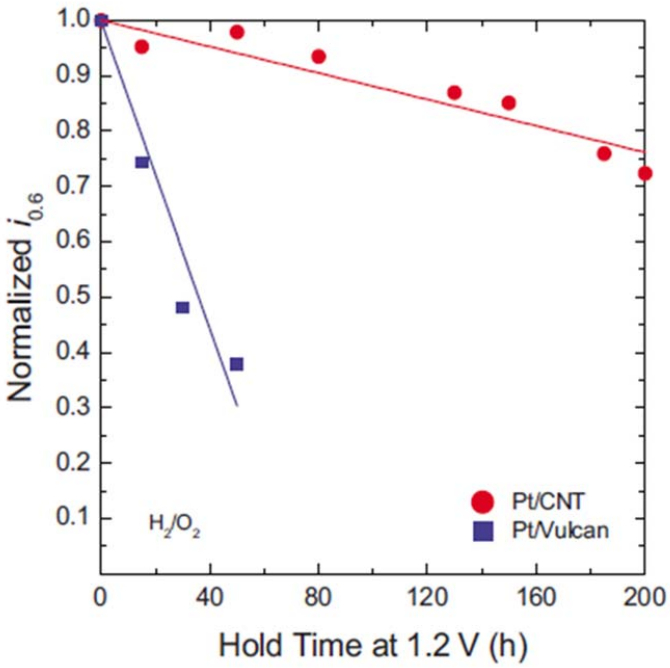


**Figure 2.17** Normalized current densities with $H_2/O_2$ at 0.6 V for Pt/CNT and Pt/Vulcan carbon as a function of hold time at 1.2 V. Reprinted from reference [85].

Similar to graphene, doping with heteroatoms can alter the surface properties and electronic structure of pristine CNTs. Boron (B) and nitrogen (N) are easily incorporated into the graphene layer in CNTs due to their similar atomic size and electron configuration to carbon and the effectively tailor characteristics compared to pristine CNT.[86-88] Notably, N-doped CNTs (NCNTs) have been introduced with remarkable change in electrical properties and chemical reactivity by theoretical calculation and empirically evaluation. NCNTs can be metallic conductors or can have narrow band gaps since lone pair electrons on N atoms in graphene layer of CNTs contribute to delocalize π-electrons.[89] Furthermore, the enhanced electrocatalytic activity NCNT itself for oxygen reduction reaction (ORR) has been proposed. Chen et al. investigated ORR activity of NCNTs in basic electrolyte as precursors to prepare NCNTs via

chemical vapor deposition were altered.[90] Pyridine and ethylene diamine (EDA) were used as precursors with a synthetic catalyst of ferrocene. TEM images of EDA-NCNT and pyridine-NCNT (Py-NCNT) in **Figure 2.18** show a bamboo-like structure which is a well-known feature of nitrogen incorporation in CNT. The formation of positive surface curvature by doped nitrogen atoms in the graphene layer, which is energetically favorable, creates the bamboo-like structure. More bamboo-like structure was observed in EDA-NCNT, indicating that more nitrogen species were incorporated. In addition, EDA-NCNT appeared to have thinner walls than Py-NCNT which could be related to effective surface reactions such as electrochemical oxygen catalysis. Based on the physical properties of the NCNTs, the electrocatalytic activity of NCNT in the ORR was evaluated in $O_2$-saturated 0.1 M KOH and compared with that of state-of-the-art Pt/C catalysts. As shown in **Figure 2.19**, EDA-NCNT demonstrates better ORR activity than Pt/C and pyridine-NCNT in terms of on-set potential, half-wave potential and limiting current density. XPS analysis also showed that EDA-NCNT contained higher nitrogen content which could affect the catalytic activity. Additionally, this NCNT catalyst has been used in Zn-air batteries and effectively improved the performance of practical Zn-air batteries.[91]

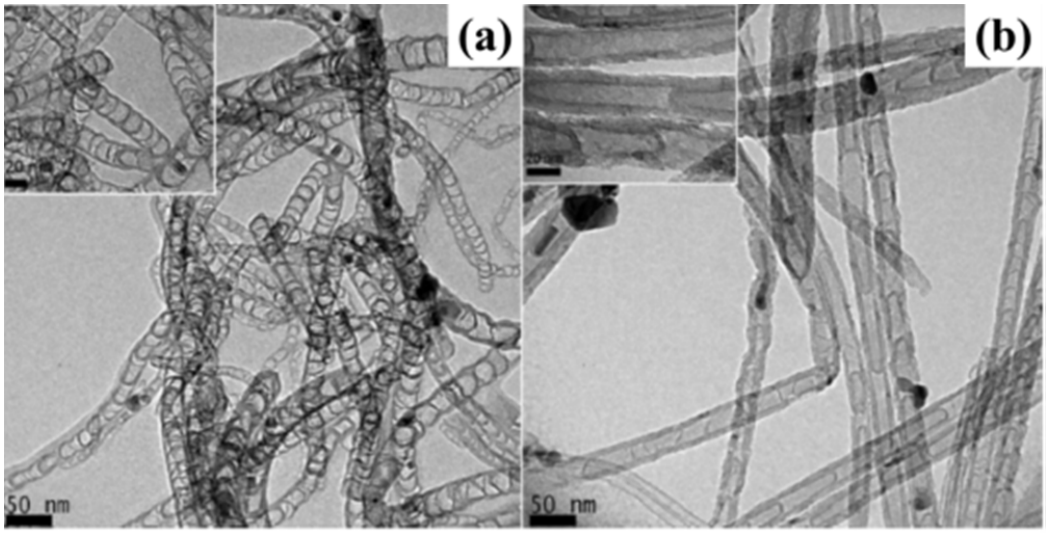


**Figure 2.18** TEM image of (a) EDA-NCNT and (b) Py-NCNT. The bamboo structure is shown in both images. The scale bar in the inset of A and B is 20 nm. Reprinted from reference [90].

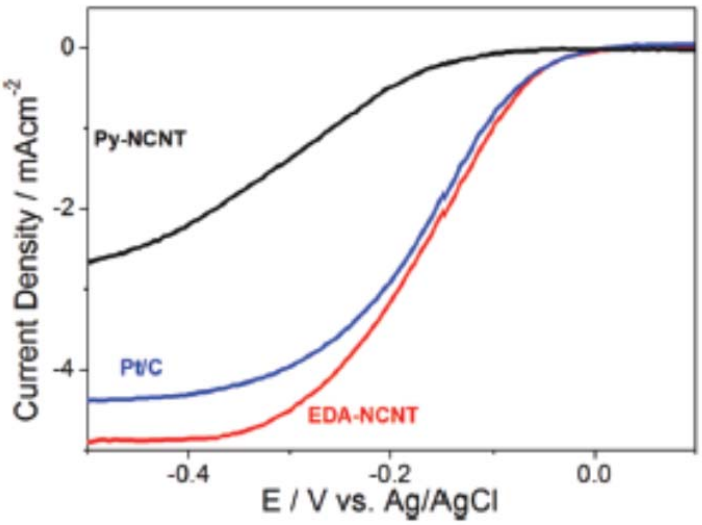


**Figure 2.19** Polarization curve of EDA-NCNT, Py-NCNT and Pt/C at 1600 rpm. EDA-NCNT shows better ORR catalytic performance compared to Py-NCNT and Pt/C. Reprinted from reference [90].

## 2.3 Research scope

As described in previous chapters, Li-air batteries are the promising system for the future energy source as well as the storage systems. Among the proposed concepts for the battery configuration, the aqueous catholyte-based Li-air batteries are believed to be most attractive in terms of the performance and safety. However, a few barriers of Li-air battery such as insufficient cycle stability, low energy efficiency and poor discharge rate capability still prevent their practical use and commercialization. These issues are directly associated with the ORR for discharge performance and the OER for charge performance in the cathode due to its sluggish reaction kinetics which significantly affects the desired power and energy density and cycle stability of Li-air battery. Precious platinum (Pt) metal-based catalysts exhibit the best electrocatalysis for the ORR with a swift kinetics and iridium (Ir) or ruthenium (Ru)-based catalysts have been reported to be excellent OER catalyst in alkaline media. However, high costs, poor durability and single reaction (either ORR or OER) catalysis do not meet the requirements for commercial rechargeable batteries. Therefore, development of affordable and highly active bi-functional catalysts that significantly enhance both ORR and OER kinetics in a cathode is necessary in order to widely commercialize Li-air batteries.

The goal in this study is the development of novel-structured bi-functional catalysts using nitrogen-doped graphene or carbon nanotube and perovskite oxide composite with straightforward synthesis methods. Firstly, a simple synthetic method and its catalytic activity toward ORR of NRGO was investigated, followed by developing $La_{0.5}Sr_{0.5}Co_{0.8}Fe_{0.2}O_3$ porous rod (LSCF-PR)/NRGO composites as a bi-functional catalyst since it was expected that high surface area perovskite oxide could be a promising OER catalyst according to the literature

review as introduced in this chapter. An electrospinning method was applied to prepare the novel nanorod morphology of LSCF-PR. Based on the electrochemical testing results with the LSCF-PR/NRGO composite catalyst, the combination of nitrogen-incorporated graphitic carbon and the perovskite oxide is a promising approach to obtain highly effective bi-functional catalysts that overcome the current challenges with conventional catalysts.

The following chapters focus on the ORR and OER activities of NCNT directly grown on RGO. The methodology to grow NCNT on a substrate as well as the formation of an effective morphology for enhanced catalytic activity are described. Based on the study of the NCNT/RGO composite catalyst, a one-pot method to prepare LSCF-based NCNT composite (op-LN) with combination of a simple calcination method and the injection chemical vapor deposition (CVD) method is proposed. Not only the outstanding activities, but also the proposed synthesis procedure to simplify the preparation of bi-functional catalysts, and can potentially offer a basic strategy for large-scale production. Lastly, the performance of a home-made practical Li-air battery with op-LN catalyst is studied in a full cell.

# 3. Experimental

## 3.1 Catalyst preparation

### 3.1.1 Preparation of graphite oxide (GO)

Most well-known method of graphene oxide synthesis was first established by Hummers in 1957.[92] In his method, harsh acidic condition with sulfuric acid and sodium nitrate adding potassium permanganate ($KMnO_4$) as a strong oxidizing agent effectively oxidized graphite powder.[92] During the reaction, potassium permanganate reacts with strong acid, sulfuric acid, producing dimanganese heptoxide ($Mn_2O_7$) as following reaction equation,

$$\mathbf{KMnO_4 + 3H_2SO_4 \rightarrow K^+ + MnO_3^+ + H_3O^+ + 3HSO_4^-} \quad (3.1)$$

$$\mathbf{MnO_3^+ + MnO_4^- \rightarrow Mn_2O_7} \quad (3.2)$$

Dimanganese heptoxide is known to highly oxidizing agent (stronger than $KMnO_4$) and explode at relatively mild temperature (>55$^oC$) or in contact with organic compounds. This material ended up oxidizing graphite powder, determining the structure and reactions pathways while graphite oxide was being prepared.

In this study, modified Hummers method was applied to enhance the degree of oxidation of graphene oxide (GO) as reported by Marcano et al.[93]. Graphite powder is purchased from Alfa Aesar (A Johnson Matthey Company, U.S.A). Graphitic powder (2 g) was dispersed in 400

mL of concentrated $H_2SO_4$ and $H_3PO_4$ (9:1 (v/v)) mixture in an ice bath. 18 g of $KMnO_4$ was slowly added to the solution with continuously stirring, keeping the temperature of the solution below 25 ℃. Then the temperature of the mixture increased to 55 ℃ and the mixture kept stirring until the color became brownish (~16 hr). Deionized (DI) water (400 ml) was slowly added to the mixture. Subsequently, the suspension was treated with $H_2O_2$ solution (20 mL, 30%) turning bright-yellow in color. The resulting solution was centrifuged (6000 rpm for 5 min) and the supernatant was decanted. The precipitated powder was washed with DI water (250 mL), HCl (250 mL, 30%), ethanol (250mL), and finally DI water (200 mL) twice, and then was placed into freeze-drying set-up. After all water had dried out, GO was used to prepare reduced graphene oxide (RGO).

### 3.1.2 Electrospinning method

Functional nanomaterials with specific morphology and dimensionality are known to have direct impact on the degree of electrochemical performances. One-dimensional (1-D) nanomaterials are highly interesting since they are considered to have effective morphology for improving their chemical, physical and electrochemical properties. 1-D nanomaterials provide a high volume fraction with large surface area compared to bulk materials and fast electron and ion pathway, greatly improving surface reaction kinetics and electrical conductivities. While traditional methods for preparing 1-D nanomaterials generally use a bottom-up approach with complex multi-steps, electrospinning method is a top-down approach known as a fascinating research area in material science. It is highly versatile fabrication technique for producing 1-D organic, inorganic and hybrid nanomaterials with morphologies that can be controlled into core–

shell, hollow or porous fiber, and even multichannelled microtube arrangements.[94-96] As a result, it gives the nanomaterials high surface areas and aspect ratios, low densities and high pore volumes; effectively improving their performance in energy conversion and storage devices. The electrospinning setup consist of a high voltage (kV) power supply, a thin syringe capillary tip which is loaded with polymer containing precursor solution and a grounded counter electrode (typically a metal plate such as aluminum foil) as shown in **Figure 3.1**.[94] The counter electrode is set to the syringe tip in close proximity (normally 5-20 cm), and the power supply in the kilovolt range is connected to the syringe tip. As the high voltage is applied, the droplet of the sample solution at the tip experiences electrostatic forces, and then ejects a liquid jet stream towards the counter electrode. The deposited polymer in the form of nanofibers on the counter electrode is collected for the proper heat treatment depending on the desired materials. While the processing parameters (e.g. distance between a syringe tip, injection speed, applied voltage, and so on), that can be varied in the electrospinning process, influence the quality of the electrospun fibers, the composition and properties of the polymer/precursor solution can also play a significant role in determining the morphology of the materials. In this study, the electrospinning method is employed to produce high surface area perovskite oxide. A mixture of nitrate-based metal precursor and high molecular weight polyvinylpyrrolidone (PVP) in a certain ratio is prepared as the electrospinning solution. After electrospinning, the obtained electrospun fibers are treated under high temperature for calcination to make crystalline metal oxides and burns away the polymer to produce porous architecture. The procedure in detail is presented in Chapter 5.

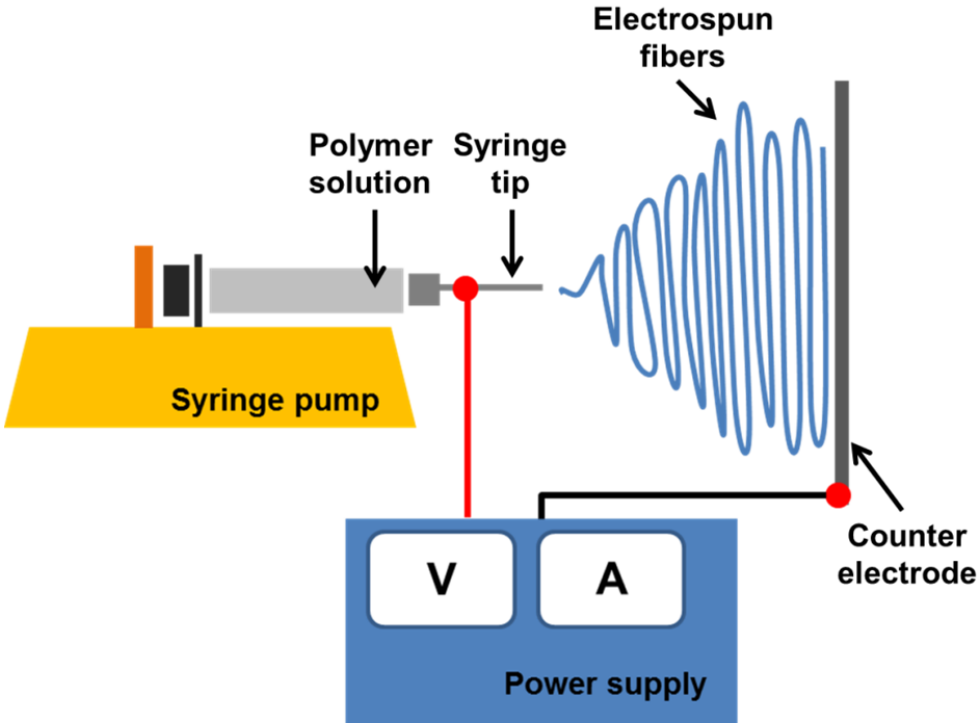


**Figure 3.1** Conventional electrospinning setup.

## 3.2 Catalyst characterization

### 3.2.1 X-Ray Diffraction (XRD)

X-ray diffraction (XRD) is a key characterization technique used to determine the crystal structures of materials. X-rays are employed to generate the diffraction pattern of the crystal because wavelength of X-ray is typically the same order of magnitude (1–100 angstroms) as the spacing between atomic planes in the crystal. The principle of XRD obeys the well-known Bragg's law which is shown in equation (3.3) and **Figure 3.2**;

$$\mathbf{2d\sin\theta = n\lambda} \qquad (3.3)$$

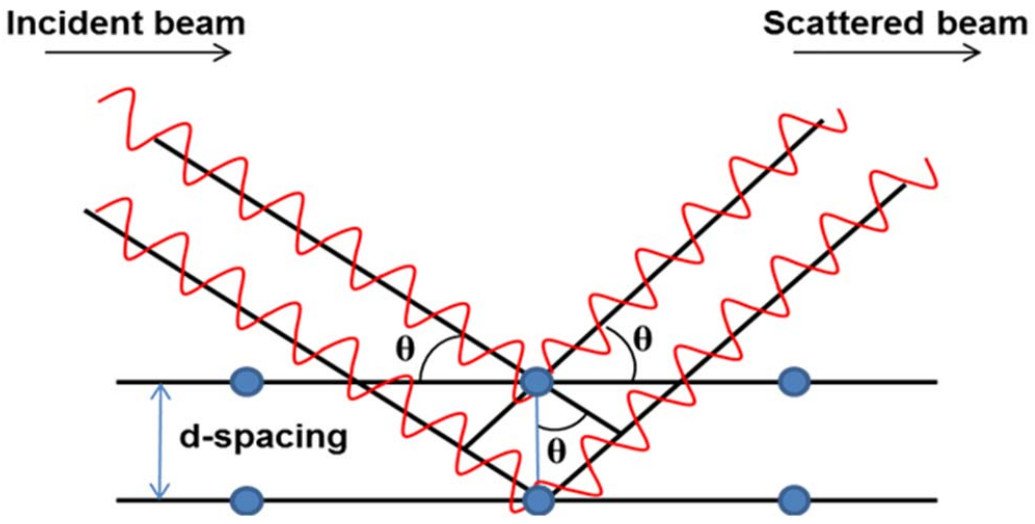


**Figure 3.2** Schematic of X-ray interacting with atoms in the crystal.

where n, λ, d, and θ represent the order of the spectrum (any integer), the wavelength of the X-rays, the spacing between diffracting planes, and the incident angle, respectively. As a result,

XRD pattern, which is the intensity of diffracted X-ray versus the angle at which the diffractions occur, are obtained. The patterns having the intensity maxima and the angles are compared to the theoretical diffraction patterns of crystal structures in the database (e.g. JCPDS card) to identify the sample's crystal phase. It is worth noting that XRD technique cannot provide the patterns of amorphous materials because their structures are in random orientations yielding diffused XRD patterns. In this study, XRD is applied to investigate the crystalline phase of the perovskite oxides catalysts.

### 3.2.2 Scanning Electron Microscopy (SEM) and Transmission Electron Microscopy (TEM)

As compared with light microscopy (LM) which uses visible light as a source of optical lenses to magnify specimens, electron microscopy (EM) uses an electron beam to take images of a specimen. The electron microscope takes advantage of the much shorter wavelength of the electron such as $\lambda = 0.005$ nm at an accelerating voltage of 50 kV, in contrast to the wavelengths of visible light which are between 400 nm and 700 nm. With this short wave length, the electron microscope makes it possible to magnify samples up to 500,000 times their original sizes by especially TEM. Electron microscopes can be divided into the two basic types that are the scanning electron microscope (SEM) and the transmission electron microscope (TEM), based on the types of electron signals and their mechanism for developing images.[97] As shown in **Figure 3.3**, SEM uses the electron signals that are reflected to the direction of incident beam and TEM uses the transmitted signals through the specimen. In brief, the scanning electron microscope produces an image with the help of secondary electrons that gives the viewer a three

dimensional image, while the transmission electron microscope projects electrons through an ultrathin slice of the specimen and generates a two dimensional image. It is worth to note that there is another similar type of electron microscope which is the scanning transmission electron microscope (STEM). This microscope has features of both SEM and TEM, and uses a scanning electron beam to penetrate thin specimens making up for the TEM's shortcomings. Depending on the instrument used, specimens can be magnified roughly between 10 and 100,000 times in SEM and between 500 to 500,000 times in TEM. This makes electron microscopes extremely valuable tools for the ultra-structural examination of any kind of object. In this study, SEM is utilized to observe surface morphologies of developed nano-sized catalysts, while TEM is used to take images of internal structures of the catalysts.

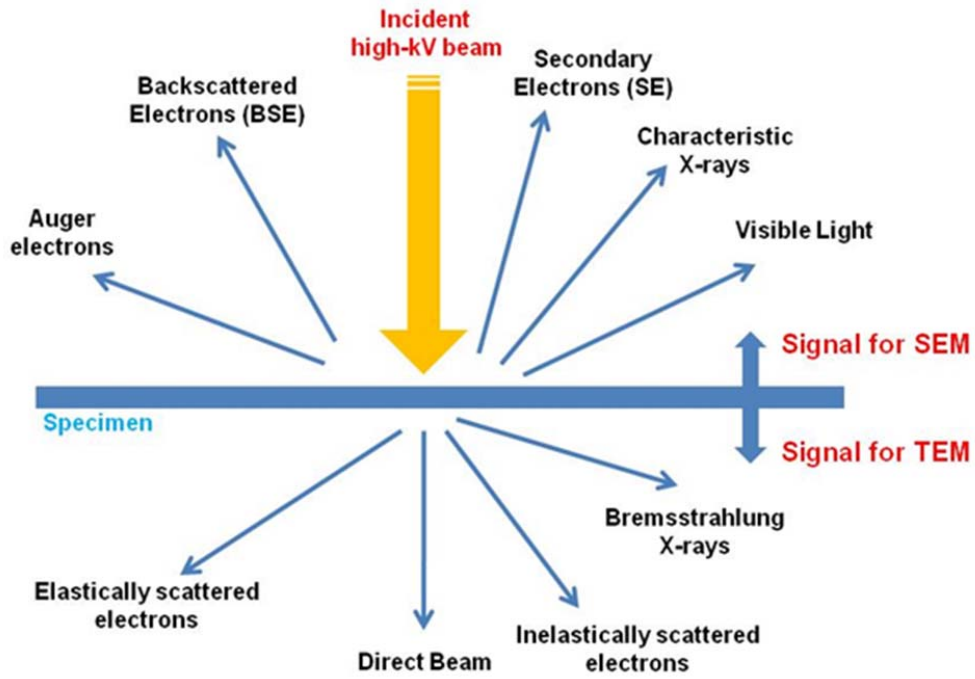


**Figure 3.3** Signals generated when a high-energy beam of electrons interacts with a specimen.

### 3.2.3 Energy dispersive x-ray spectroscopy (EDS)

Energy dispersive x-ray spectroscopy (EDS or EDX) is a common analytical technique used to identify chemical elements in a sample. EDS are commonly coupled with SEM and TEM to be conducted simultaneously with the microscopic study. The EDS technique allows characterization of the elemental composition including quantitative analysis by detecting x-rays emitted from a sample during the bombardment with the electron beam. A typical EDS spectrum is provided as a plot of x-ray counts vs. energy (in keV), which corresponds to the various elements in the sample. It can also create element mapping, which is helpful in analyzing the localized elements on a sample since characteristic x-ray intensity is detected at each characteristic energy value for each element, thereby displaying "maps" of relative contrast depends on the amount of localized elements across the sample. In this study, EDS mapping is utilized to confirm chemical elements in the proposed catalysts, especially perovskite oxide of LSCF.

### 3.2.4 X-Ray Photoelectron Spectroscopy (XPS)

X-ray photoelectron spectroscopy (XPS), also known as electron spectroscopy for chemical analysis (ESCA), is a highly prevalent characterization tool, providing information about the elemental composition of a sample and information about the structure and oxidation states of the compounds. In principle, x-rays with known energy ($h\upsilon$) is irradiated on an analyte, causing emission of electrons by photoelectric effect and the kinetic energy ($E_k$) of the electrons that escape from the material's surface (top 1 to 10 nm) is detected. Based on the irradiated x-ray

energy and the kinetic energy of electrons, binding energy ($E_b$) of the electrons can be calculated by means of the equation.

$$\mathbf{E_b = h\upsilon - E_k - w} \qquad (3.4)$$

In this equation, w is the called work function of the spectrometer. The binding energy spectrum versus the number of electrons can directly identify the elements on the surface of the material and provide the relative amounts of each element. In this study, XPS is utilized to confirm and quantify nitrogen doping on RGO and CNT by detecting nitrogen content and its binding configurations on NRGO and NCNT. In addition, chemical elements of the perovskite oxides in the study are analyzed by XPS.

### 3.2.5 Raman Spectroscopy

Raman spectroscopy is a characterization method to provide information related to the vibrational and rotational modes of molecules. Raman spectra are similar to the infrared spectra which provide useful information for functional group and fingerprint region to identify the molecular structure. This information provides qualitatively characteristics of the degree of defects in the pristine graphene layer or in the heteroatom-doped graphene layer in (N)RGO or (N)CNT. Raman spectra are obtained by irradiating a sample with a powerful laser source of visible or near-infrared of monochromatic laser light. During irradiation, the interaction between the laser beam and the sample leads to spectral excitation and then subsequently emitted radiations in vibration with characteristic frequency are detected with three different frequencies: Rayleigh scattering which is same wavenumber of excitation source, Stokes frequency which is lower wavenumber than that of the excitation source, and Anti-Stokes frequency which is higher

wavenumber than that of the excitation source. Based on the intensity, Stoke lines normally are used to analyze the sample. The emitted light energy detected by spectrophotometer is plotted on the Raman scattering intensity to the wavenumber. In this study, Raman spectroscopy is mainly used to characterize the degree of the defects caused due to doping nitrogen to graphene layer on differently controlled temperatures.

### 3.2.6 Brunauer, Emmett and Teller (BET) method and Barrett, Joyner and Halenda (BJH) method

As an extension of the Langmuir isotherm theory for monolayer adsorption, the BET method was developed with a multi-layer adsorption model in 1938.[98] BET method serves the specific surface area of a solid material using the physical adsorption of gas molecules on a solid surface. The specific surface area is obtained by calculating the amount of adsorbate gas which adsorbs monolayer on the surface. The BET method obeys the assumptions from the Langmuir isotherm theory which are (i) adsorption occurs on specific sites all of which are identical, (ii) the energy of adsorption is independent of the number of occupied sites, and (iii) the adsorbate is typically adsorbed in a monolayer. Additionally, the BET method applies other hypotheses as follows; (i) Each layer is treated as a Langmuir monolayer, (ii) each adsorption layer has no interaction with another layer. Based on the assumptions listed above, the resulting BET equations are derived by Equation (3.5)[98]:

$$\frac{\mathbf{1}}{\boldsymbol{V}[(\boldsymbol{P_0}/\boldsymbol{P})-\mathbf{1}]} = \frac{\mathbf{1}}{\boldsymbol{V_m C}} + \frac{\boldsymbol{C}-\mathbf{1}}{\boldsymbol{V_m C}}\left(\frac{\boldsymbol{P}}{\boldsymbol{P_0}}\right) \tag{3.5}$$

Where **V = volume of gas adsorbed ($cm^3$)**

**P = gas pressure**

**$P_0$ = equilibrium vapor pressure at the test temperature**

**$V_m$ = volume of adsorbate as monolayer ($cm^3$)**

**C = BET constant**

From a typical BET experiment, the volume of gas adsorbed and $P/P_0$ are measured with the adsorbate of $N_2$ at 77K. Based on the equation (3.5), when the vapor pressure (P) is low, compared to $P_0$ ($0.05 < P/P_0 < 0.3$), the plot of $1/[V*((P_0/P)-1)]$ vs. $(P/P_0)$ can be linear providing intercept $((C-1)/V_mC)$ and slope $(1/V_mC)$. It is worth noting the data should be selected between $0.05 < P/P_0 < 0.3$ which is the pressure range associated with the presence of a monolayer. The intercept and slope in the plot yields volume of adsorbate as monolayer (Vm), then finally the Vm is applied to following equation (3.6) to calculate the specific surface area.

$$S = \frac{V_m N_{AV} A_{ab}}{V_i M} \tag{3.6}$$

Where **S = specific surface area ($m^2$ $g^{-1}$),**

**$N_{AV}$ = Avogadro's number ($6.022\times10^{23}$ $mol^{-1}$)**

**$A_{ab}$ = area of single adsorbate molecule using the cross-sectional area ($m^2$)**

**$V_i$ = volume of one mole of ideal gas (L)**

**M = mass of sample (g)**

Barrett-Joyner-Halenda (BJH) is a useful method for determining pore size distributions of mesoporous materials which have pores with diameters between 2 and 50 nm. Before the description of BJH method, adsorption/desorption isotherm from BET method must be understood. First, a capillary condensation of the adsorbate occurs in the pores under saturated vapour pressures. Capillary condensation can be described by an adsorption isotherm as shown in **Figure 3.4**. In stage 1, the adsorption mechanism at low relative pressure is similar with the adsorption on planar surfaces followed by multilayer adsorption (stage 2). After the adsorbed layer reaches a critical thickness (stage 3), capillary condensation of the adsorbate occurs within the pores (stage 4). During desorption, the adsorbate from the pore is evaporated by a thinning of the meniscus (stage 5). In stage 6, equilibrium reaches between a multilayer of adsorbate on the pore and the gaseous adsorbate in the center of the pore following adsorption branch of adsorption isotherm. In this case the pore size and shape and the interaction between the adsorbate and the pore walls can affect the condensation pressure. From these isotherms, useful information of the properties of the mesoporous space can be characterized.[99]

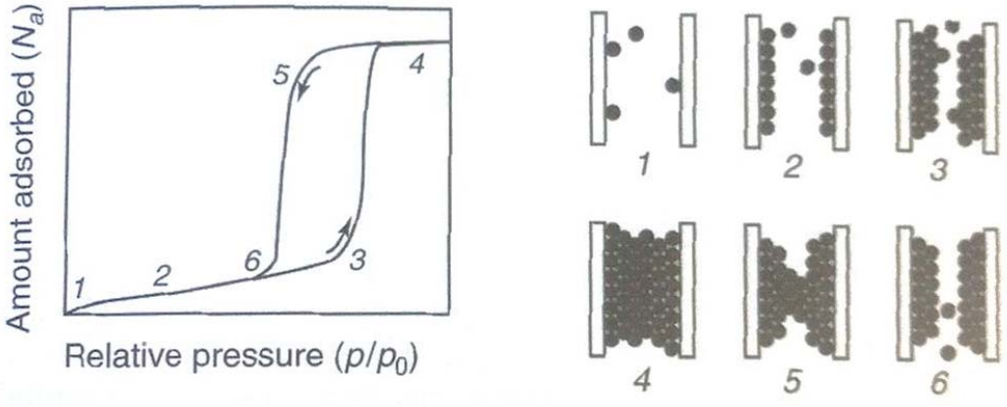


**Figure 3.4** An adsorption isotherm in a cylindrical mesopore and a schematic representation of the involved multilayer adsorption and pore condensation processes.[99]

For the calculation of pore size distribution, Barrett et al.[100] suggested the process involving stepwise condensed adsorbate emptying from the pores with decrease in the relative pressure. The capillary condensation in the pores and thinning of the adsorbed layer by a reference isotherm are employed to establish the BJH theory and one important assumption is at relative pressure close to unity (practically $P/P_o = 0.095$) all pores are fully occupied with the condensed adsorbate (fluid). For calculation of the pore volume distribution with pore size using the isotherm results (relative pressures), Classical Kelvin equation (3.7) is utilized and de Boer et al.[101] proposed an equation (3.8) to calculate the thickness t of the multilayer that remains in the pore. Using these two equations, the pore radius r and distribution of radius, area and volume of the pores can be obtained at the sequence points of steps defined for the isotherm by repeating calculation.

$$\ln\left(\frac{P}{P_o}\right) = -\left(\frac{2\gamma V_L}{RT(r-t)}\right) \tag{3.7}$$

$$t = \left(\frac{13.9}{0.34-\log\left(\frac{P}{P_o}\right)}\right)^{1/2} \tag{3.8}$$

Where r is the pore radius, $P/P_o$ is the relative pressure at which pore emptying start, $\gamma$ is the liquid surface tension, t is the thickness of an adsorbed multilayer film and $V_L$ is the molar volume of condensed adsorbate. The BJH method is widely applied to calculate the pore size distribution of mesoporous materials, however, it is worth noting that this method does not provide accurate information with pore sizes in the range of 2-4 nm because of its lack of microscopic phenomena.[99] In this study, BET and BJH methods are utilized to not only investigate surface area and pore size distribution of the different morphologies of perovskite

oxides, but also analyze physical properties of NCNT/RGO composite catalyst that are relevant to electrocatalytic activities in comparison to NCNT and RGO.

## 3.3 Electrochemical Characterization

### 3.3.1 Linear sweep voltammetry (LSV), cyclic voltammetry (CV) and chronoamerometry (CA)

Linear sweep voltammetry (LSV) and cyclic voltammetry (CV) are the types of potentiodynamic electrochemical measurement technique, which are used to investigate redox characteristics of a material. LSV can be used to investigate the electrochemical reaction which is known to be irreversible while the potential is swept in one direction.[102] However, in most occasions the potential is swept forward and backward to investigate anodic and cathodic reactions within a certain potential window. This method is named CV.[103] In other words, during the measurement, the potential of the working electrode is scanned linearly at a certain potential scan rate (mV $s^{-1}$) within a desired potential range. Then the current is detected along the potential window, resulting in a plot of potential versus current, which is called a cyclic voltammogram **(Figure 3.5)**. The electrochemical properties of analytes are investigated with reaction potentials associated with the current in the cyclic voltammogram. In this work, this technique is used to confirm ORR and OER activities of the developed catalysts in an $O_2$- and Ar-saturated electrolyte, respectively. Furthermore, CV is conducted in an Ar-saturated inert electrolyte to investigate any occurrence of undesired reactions. Next, CA is one of the fundamental electrochemical methods, which instantaneously changes the initial potential to the

step potential and the current response is detected as a function of time, obeying diffusion control behavior, during the experiment as described in **Figure 3.6**. Generally, the Corttrell equation which expresses the relationship between current and time$^{1/2}$ with some parameters (e.g. number of electron involved in the reaction, electrochemical active area, diffusion coefficient, etc.) in CA is the most useful to characterize analytes. However, the equation is not discussed in depth in this work since the use of CA method is limited to monitoring the limiting current behaviors of the RDE measurement in certain reaction potentials for the evaluation of the durability of the catalyst.

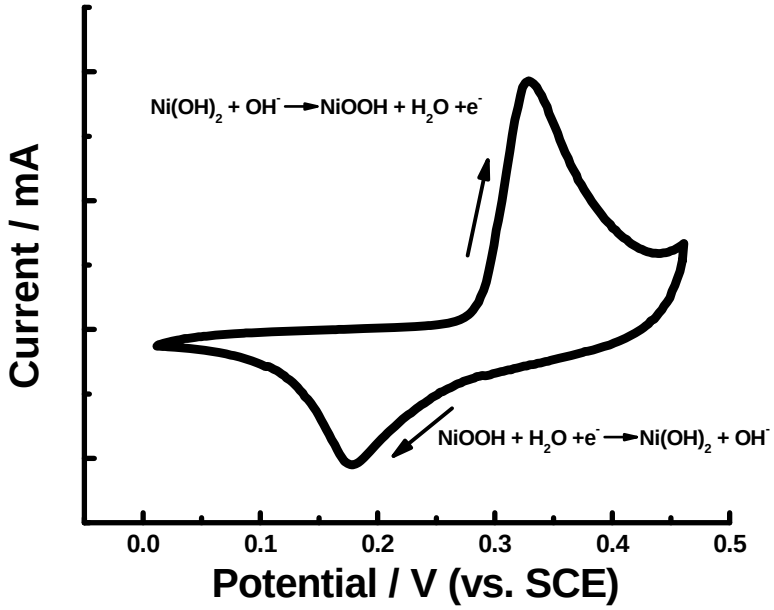


**Figure 3.5** Cyclic voltammogram of $Ni(OH)_2$ oxidation and reduction reaction in 2 M KOH solution.

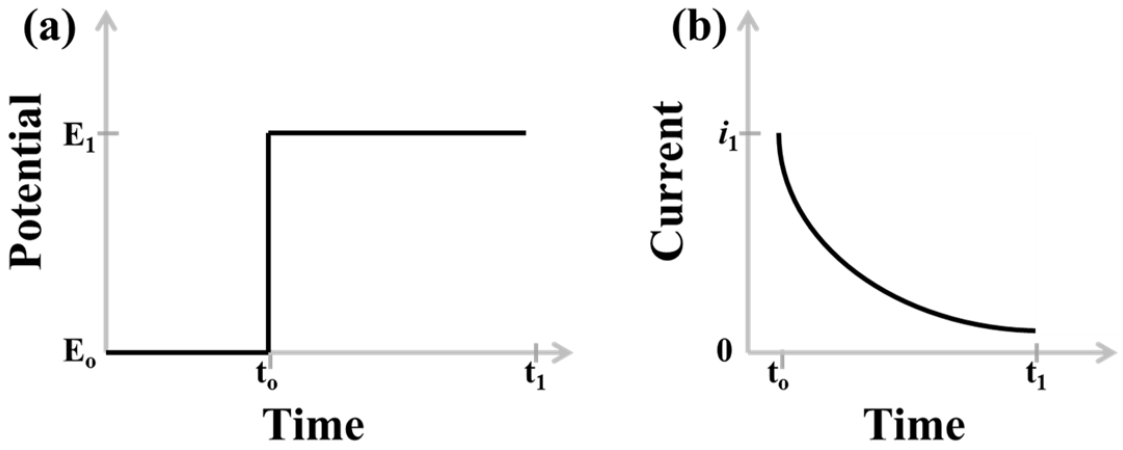


**Figure 3.6** Conventional scheme of the CA method. (a) Potential step from $E_0$ to $E_1$ and (b) current response associated with the potential step as a function of time.

### 3.3.2 Rotating disk electrode (RDE) measurement

A RDE measurement is an electrochemical technique widely used to obtain sufficient mass transport in highly repeatable way to study the mechanism of redox reactions and screen materials based on the electrochemical activities.[103] Strictly, it may not an electrochemical method since it just alters the reaction environment affecting the electrochemical responses. It means that RDE should be combined with other electrochemical methods such as CV or LSV. A RDE is simply defined as a hydrodynamic working electrode in an electrochemical cell. The RDE consists of a disk electrode imbedded in a rotating rod of an insulating material and rotating of the disk electrode creates a totally defined solution flow pattern in which the mass transport of the species is almost complete by convection. The configuration of a RDE is schematically illustrated in **Figure 3.7(a) and (b)**, the motion of electrolyte can be described as shown in **Figure 3.7(c) and (d)**. The disk electrode drags the solution nearest to it and imparts to it momentum in the tangential direction, resulting that electrolyte is pushed out of the surface

sideways and is replaced by solution moving in from the bulk, in a direction perpendicular to the surface. The rotating surface acts, in effect, as a pump, pulling the liquid up toward it. So, it enables intrinsic electrochemical kinetic study, to which mass transport is controlled, to be investigated to study the reaction mechanism.

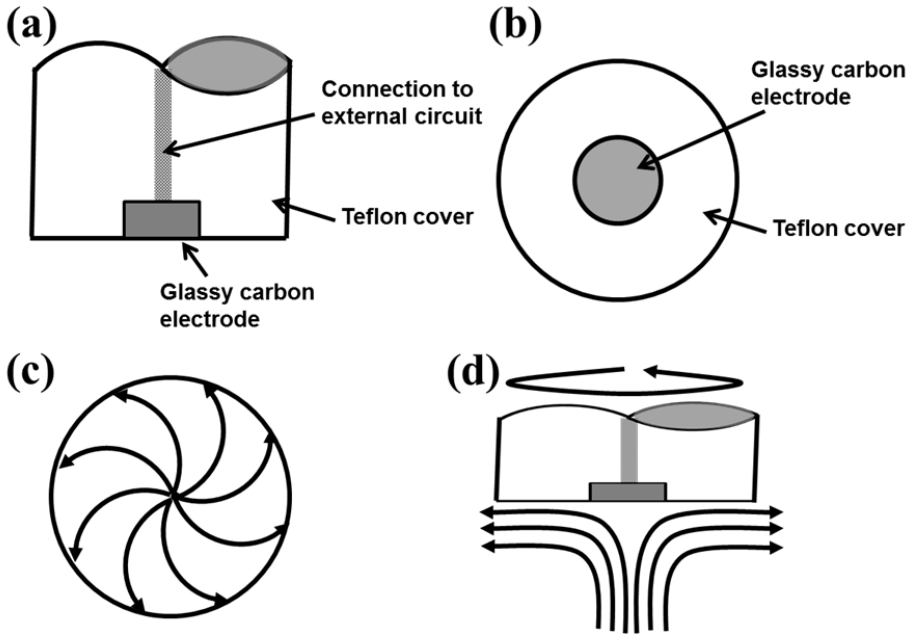


**Figure 3.7** (a) Side view and (b) bottom view of the RDE. (c) Tangential motion of the electrolyte in the plane of the RDE and (d) perpendicular motion of electrolyte towards the RDE.

In the projects, a glassy carbon RDE coated with the developed catalyst is used as a working electrode, while saturated calomel electrode (SCE) is used as a reference electrode and Pt wire is used as a counter electrode. In order to coat the catalyst on the RDE, catalyst ink is prepared by dispersing the catalyst into ethanol-diluted Nafion solution. Mostly RDE measurements are utilized in combination with cyclic voltammetry (CV) and linear sweep voltammetry (LSV) technique in which potential range for redox reactions is swept and the

current produced is detected while the electrode is being rotated at various speeds. Generally, the RDE measurement can be divided into three regions which associate with three parameters of onset and half-wave potentials and diffusion (mass transport) limiting current value to determine catalytic activities as shown in **Figure 3.8**. First region is kinetic control region including on-set potential which is trigger potential for a desired reaction, second region is kinetic and diffusion mixed control region including the half wave potential and third region is diffusion control region including diffusion controlled current.

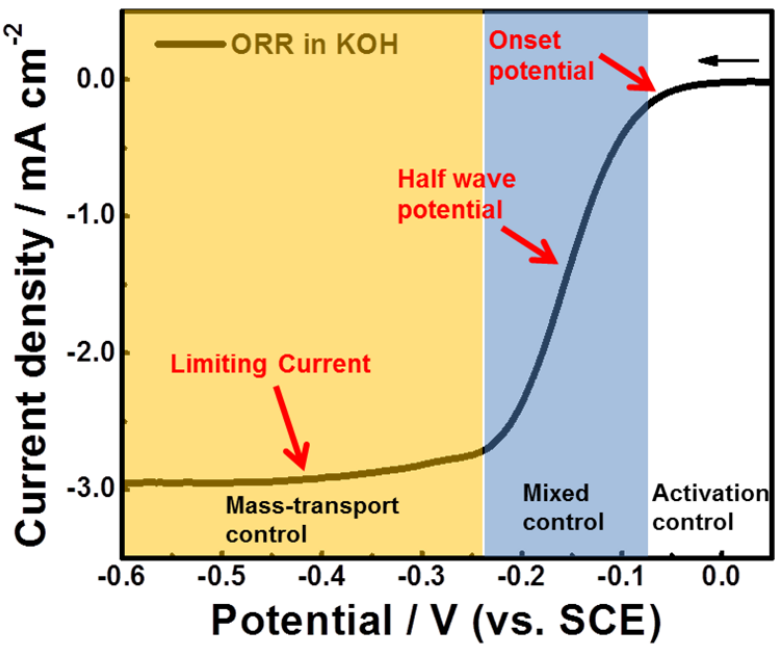


**Figure 3.8** Schematic i/V profile for oxygen reduction reaction in KOH

Lastly, the results from the RDE measurements at different rotating rates is used to study the reaction kinetics and mechanisms of ORR in 0.1 M KOH, which is employ in the project, via the Koutecky-Levich (K-L) equation as the following[104]:

$$\frac{1}{i} = \frac{1}{i_k} + \frac{1}{i_d} \quad (3.9)$$

$$i_k = nFkC_o \quad (3.10)$$

$$i_d = 0.2nFD_o^{2/3}\upsilon^{-1/6}C_o\omega^{1/2} \quad (3.11)$$

In the above equation, $i_k$ and $i_d$ is the kinetic current and diffusion limiting current density, respectively, F is the Faraday constant (96 485 C $mol^{-1}$), k is the rate constant for ORR (m $s^{-1}$), $D_o$ is the diffusion coefficient of $O_2$ (1.9 x 10-5 $cm^2$ $s^{-1}$)[105, 106] in 0.1 M KOH, υ is the kinematic viscosity of 0.1 M KOH (0.01 $cm^2$ $s^{-1}$), $C_o$ is the concentration of $O_2$ in the electrolyte (1.1 x $10^{-6}$ mol $cm^{-3}$) and ω is the angular frequency of the rotation (rad $s^{-1}$), which can be converted into the rotation speed (rpm).[63] By linear fitting the Koutecky-Levich plots of $i^{-1}$ vs. $\omega^{-0.5}$ one can obtain the electron number (n) involved in ORR and rate constant (k) for ORR. For example, as results from the RDE measurements with various rotating speed, potential versus current density profiles can be obtained as shown in **Figure 3.9(a)**. It illustrates the on-set potentials are almost the same, while the half-wave potentials and diffusion limiting currents are altered by the rotation speeds Based on the RDE measurements, K-L equation can be plotted by current density versus rotation speed and then the slope in the graph allows calculation of the number of electron involved in the reaction which assists to determine catalytic activity of various catalysts as shown in **Figure 3.9(b)**.

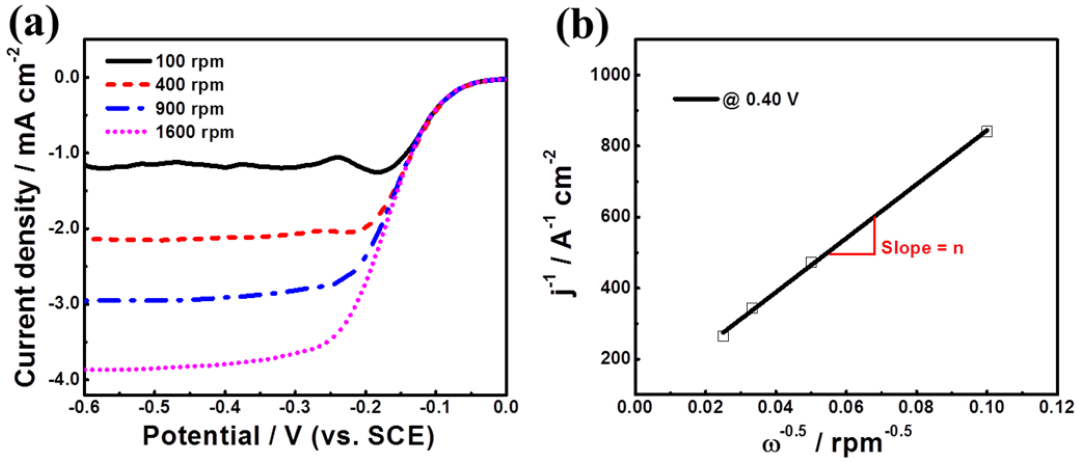


**Figure 3.9** (a) Typical RDE measurements in $O_2$-saturated 0.1 M KOH with a sweep rate of 10mV $s^{-1}$ at the different rotation rates and (b) corresponding Koutecky–Levich plots ($J^{-1}$ versus $\omega^{-0.5}$) at 0.4 V (vs. SCE).

In this study, the electrocatalytic activity and durability of the catalyst samples are examined using RDE voltammetry by a potentiostat (CH Instrument 760D) and a rotation speed controller (Pine Instrument Co., AFMSRCE). The catalyst materials are dispersed in ethanol-diluted Nafion solution to be 4 mg $mL^{-1}$ of the catalyst concentration and coated onto a glassy carbon disk electrode (5 mm OD) with the catalyst ink for the working electrode. A platinum (Pt) wire and saturated calomel electrode (SCE) were utilized as counter and reference electrodes, respectively. Cyclic voltammetry (CV) is used to investigate ORR and OER activities with durability in $O_2$ and $N_2$-saturated 0.1M KOH at a scan rate of 50 mV $s^{-1}$. Linear sweep voltammetry (LSV) is used for further examination of ORR activity in RDE measurements at a scan rate of 10 mV $s^{-1}$ in the same electrolyte.

### 3.3.3 Investigation of the catalyst's performance in a practical hybrid electrolyte Li-air battery

In Chapter 7, practical hybrid electrolyte Li-air battery performances are presented using the developed catalyst in this study. The battery is designed and fabricated **(Figure 3.10(a) and (b))** to investigate the catalyst's activities in a full cell environment. As discussed in Chapter 2, Li metal is used as the anode and a non-aqueous electrolyte of ethylene carbonate (EC) and dimethyl carbonate (DMC) mixture with 1M $LiPF_6$ is filled in to the anode side. 1 M $LiNO_3$ + 0.5 M LiOH is used as the aqueous catholyte. The catalyst layer on the gas diffusion layer (Ion Power Inc., SGL Carbon 10 BB) was prepared for the cathode as follows. First, 9.4 mg of catalyst was dispersed in 1 mL of isopropanol and sonicated for 30 minutes, followed by addition of 67 μL of 5 wt. % Nafion solution to prepare a catalyst ink. The catalyst ink was coated onto the gas diffusion layer with a conventional airbrush. After spraying, the gas diffusion electrode was dried at 80 °C for 12 h. The catalyst loading was determined by the difference in the weight of the gas diffusion layer before and after spraying. The two different electrolytes are separated by 150 μm-thick LISICON solid membrane manufactured by Ohara Corp.

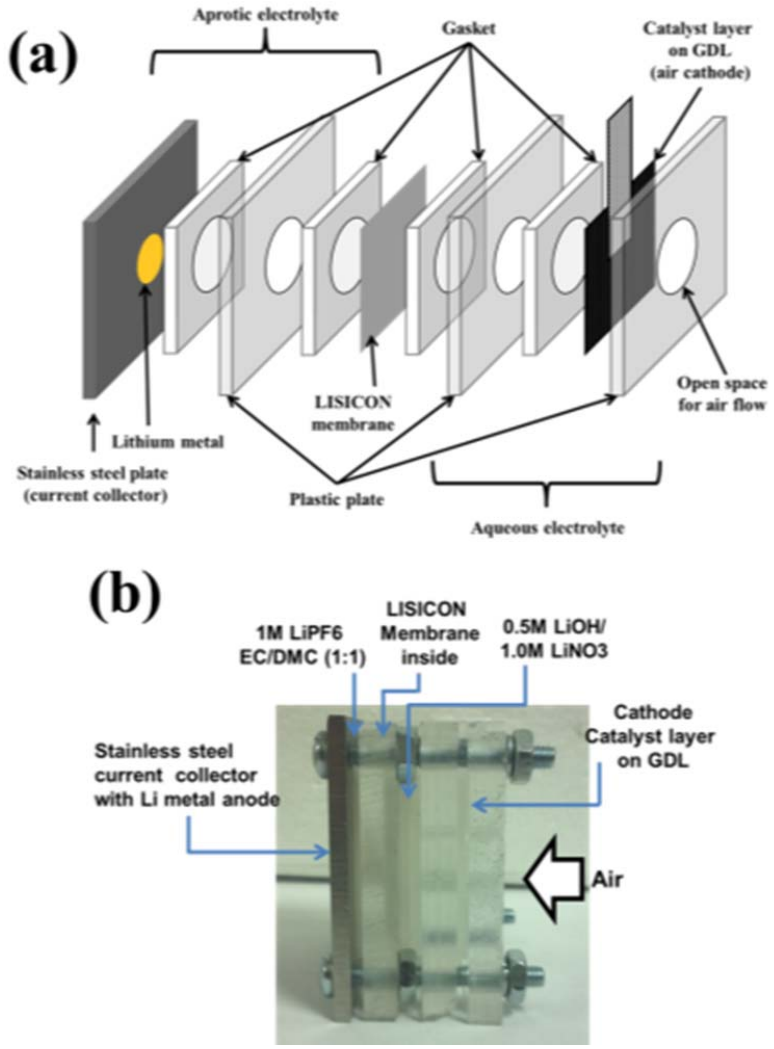


**Figure 3.10** (a) schematic view and (b) optical photograph of the hybrid electrolyte Li-air battery.

# 4. Highly ORR Active Graphene Nanosheets Prepared via Extremely Rapid Heating as Efficient Metal-Air Battery Electrode Material

## 4.1 Introduction

Previously, various synthetic routes to prepare nitrogen-doped graphene were reported;[107, 108] however, the methods are often expensive and complex to set up, and large scale production is difficult for implementation into practical applications. In addition, the most commonly used chemical vapour deposition (CVD) for graphene synthesis requires metal substrates/growth catalyst such as nickel or copper. In early works of thermally reduced graphene oxide (GO), only accordion or worm-like morphologies were obtained with far less degree of expansion of the graphitic layers.[109, 110] Later in the journal of Chemistry of Materials, a report was published on the effect of the heating rate (maximum of 50 $^{o}$C min$^{-1}$) during the graphene synthesis, but the graphene sheets formed rather densely packed morphology with limited expansion.[111]

In this chapter, our motivation is to utilize extremely rapid heating for the synthesis of highly open structured graphene sheets with heterogeneous nitrogen doping (NRGO) by a one-step process, and achieve high electrocatalytic activity for oxygen reduction reaction (ORR). This one-step technique strategically combines two separate processes of thermal reduction and ammonia treatment to produce large batches of graphene nanosheets without the use of a substrate or metallic catalyst layer. The morphological change of the sheets occurs due to the extremely rapid evolution of the gases formed during the decomposition of the oxygen groups of GO, resulting in expansion faster than the GO sheets can knit together *via* van der Waals

bonding.[111] However, to prevent the slow diffusion of the evolved gases that occurs during traditional heating processes - which leads to a more gentle reduction process - an extremely rapid heating technique has been used to heat GO at rate of 150 $^{o}$C sec$^{-1}$ or greater from room temperature to above 800 $^{o}$C within five seconds. Most of the evolved gases escape in a very short period of time, which maximizes the expansion of the graphene sheets. Hence, with the ability to control the morphology via this facile and robust synthesis technique, graphene nanosheets with optimal morphology have been synthesized for efficient ORR activity as well as a catalyst support for the formation of a bi-functional catalyst.

## 4.2 Experimental

As the synthetic set-up is illustrated in **Figure 4.1**, in a typical one-step rapid heating synthesis, the quartz tube is vacuumed and filled with Ar (Praxair) three times, and 100 mg of GO is loaded outside of the heating zone of the horizontal tube furnace. Under 100 sccm of Ar protection, the furnace is heated to a desired temperature after which 50 sccm of $NH_3$ (Praxair) is introduced to the tube and Ar flow is reduced to 50 sccm. Ar/$NH_3$ mixture is allowed to flow for five minutes then the position of the quartz tube is shifted along the horizontal furnace in less than 5 seconds to quickly bring GO to the heating zone in the center of the furnace. This rapid increase in temperature allows the sheets of GO to thermally reduce and expand, while the Ar/$NH_3$ flow allows nitrogen-doping, in a one-step process. At this point, we have exfoliated and nitrogen-doped graphene nanosheets (ex-NG). The sample names are referred as NRGO800, NRGO900, NRGO1000, and NRGO1100 based on the temperature at which the synthesis is carried out (800 $^{o}$C, 900 $^{o}$C, 1000 $^{o}$C, and 1100 $^{o}$C, respectively). After 10 minutes of $NH_3$ treatment, the tube is shifted back to bring the sample to the outside of the heating zone. The

furnace is cooled down under 100 sccm of Ar protection then the sample is collected from the quartz boat for direct use.

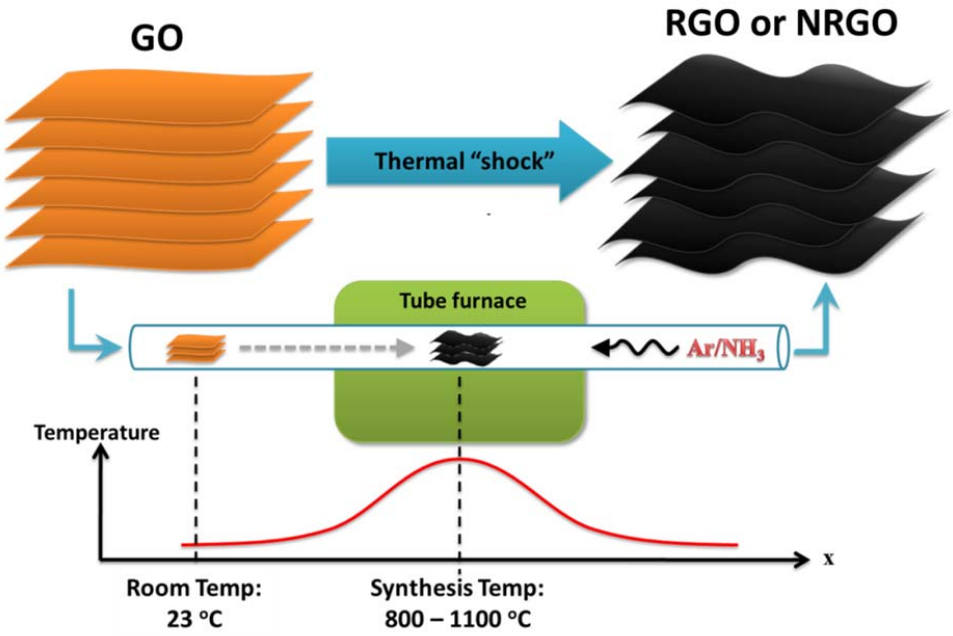


**Figure 4.1** Illustration of facile and one step synthetic method for RGO and NRGO.

## 4.3 Results and discussion

After the one-step thermal reduction and ammonia treatment under an extreme heating rate, the morphological change from GO to NRGO synthesized at 1100 $^{o}$C (NRGO1100) is revealed by SEM analysis. The layered structure observed with GO **(Figure 4.2(a))** has been clearly converted into voile-like sheets of graphene **(Figure 4.2(b))**, indicative of successful thermal reduction of oxygen groups of GO.[107] The large expansions and openings observed between the graphene nanosheets is most likely due to the very rapid heating process, which have allowed

the discharge of evolved gases from GO to occur with much higher kinetic energy, thereby expanding the sheets.

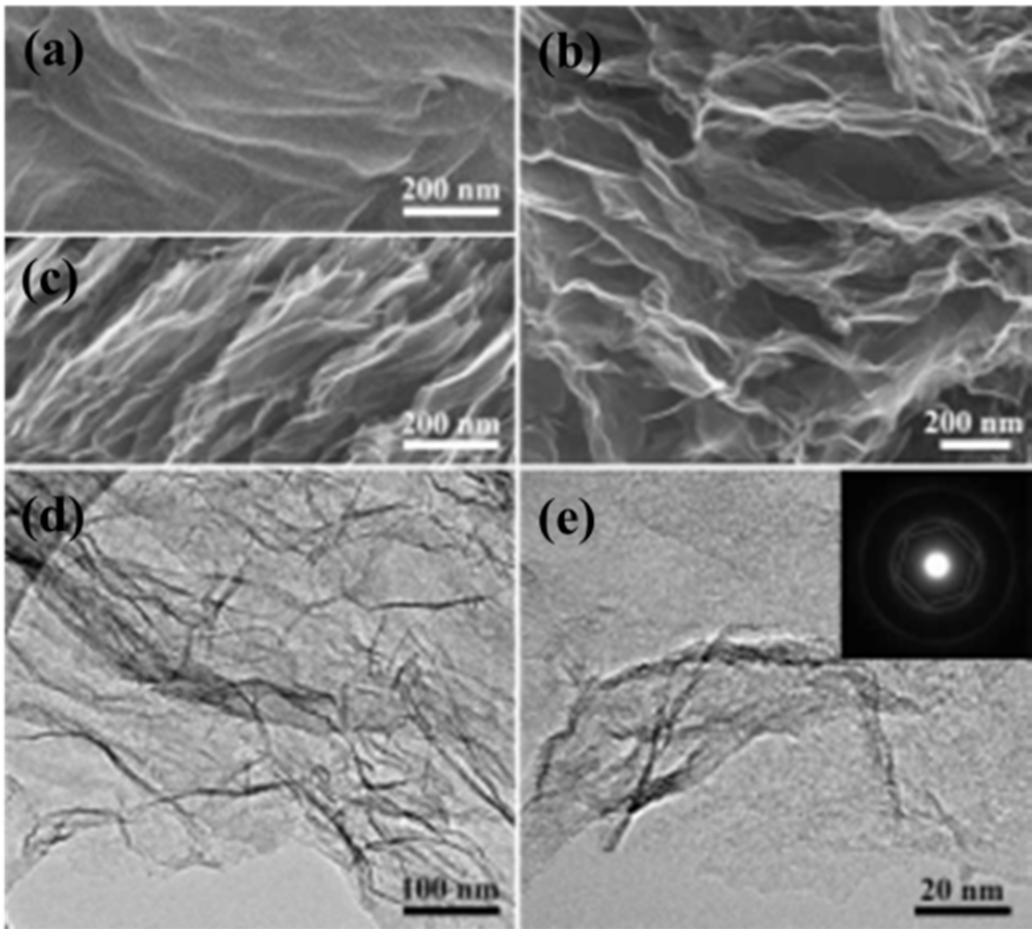


**Figure 4.2** SEM images of (a) GO prior to one-step thermal reduction and ammonia treatment, (b) NRGO1100 synthesized by extremely rapid heating ramp (~150 $^{o}$C sec$^{-1}$), and (c) NRGO1100-S synthesized by slow heating ramp (5 $^{o}$C min$^{-1}$). (d) A typical TEM image of NRGO1100 with randomly oriented wrinkles and folds. (e) HRTEM image of NRGO1100 (Inset: SAED pattern of a few layers of NRGO1100).

Compared to previous reports on thermal reduction of GO, which exhibit accordion or worm-like morphologies,[109-111] the unique open structured morphology with large spacings presented in this study is optimized for the electrocatalysis of oxygen reduction, as we

demonstrate its outstanding performance in later parts by both half-cell and single-cell testing. The wrinkles observed in the graphene nanosheets are most likely due to the incorporation of heterogeneous nitrogen species into the graphitic network, which may prevent re-stacking of the sheets. In order to experimentally verify the effect of heating rate on the degree of expansion of the graphene nanosheets and its electrochemical performance, NRGO1100-S have been synthesized by very slow heating rate of 5 $^{o}$C min$^{-1}$ (compared to ~200 $^{o}$C sec$^{-1}$ for NRGO1100) **(Figure 4.2(c))**. The SEM analysis clearly shows much densely packed morphology compared to that of NRGO1100, most probably due to the discharge gases having insufficient energy to expand the sheets. TEM characterization also confirms wrinkled surfaces of NRGO1100 **(Figure 4.2(d))**, similar to those observed in the SEM characterization.[112] HRTEM, on the other hand, reveals wavy edges of the graphene sheets, which is probably due to the ammonia in the feedstock more readily reacting with the edge planes to incorporate heterogeneous nitrogen species **(Figure 4.2(e))**. The basal planes are observed to have maintained the integrity of the graphitic network as no perforation or defects are observed in the sheets. This is important as these surfaces facilitate the transport of charges and diffusion of reactants during catalysis of ORR. To corroborate, the inset of **Figure 4.2(e)** shows the selected area electron diffraction (SAED) pattern from a few layers of NRGO1100 with a hexagonal symmetry, which is characteristic of the symmetrical three-fold sp$^2$ bonding of carbon atoms.[113] This again confirms that the graphitic network is well-maintained even after ammonia treatment at 1100 $^{o}$C.[114, 115]

The change in the structure from GO to NRGO1100 is further quantified by the X-ray diffraction (XRD) pattern **(Figure 4.3(a))**. The 002 reflection assigned to the layer-to-layer distance in the graphitic structures of GO at 10.3 $^{o}$ in 2θ shifts from a d-spacing of 8.57 Å to a

much lower value of 3.50 Å for NRGO1100 (25.4 $^{o}$ in 2θ), due to the departure of the oxygen groups of GO upon thermal reduction.[111] The degree of structural deformation incurred by thermal reduction and ammonia treatment is verified by comparing the Raman shifts of GO and NRGO1100 **(Figure 4.3(b))**. Two peaks are observed in both spectra, at approximately 1350 $cm^{-1}$ and 1590 $cm^{-1}$, corresponding to the D and G bands, respectively. The D band is characteristic of disorder in the structure caused by defects within the graphitic plane, while the G band is characteristic of the $sp^2$ bonds within any graphitic material which has $E_{2g}$ vibrational modes. The ratio of the max intensities of the two bands, $I_D/I_G$, thus reflects the fraction of structural defects and degree of exposure of the edge planes. A higher $I_D/I_G$ ratio of 1.14 is observed with ex-NG1100 compared to that of 0.97 with GO, consistent with previously reported work.[116] This suggests successful one-step thermal reduction and nitrogen-doping of NRGO because the expansion of the graphene sheets and the incorporation of the heterogeneous nitrogen species into the graphitic structure have resulted in increased edge plane exposure and creation of defects.[117] From the analysis of X-ray photoelectron spectroscopy (XPS), a characteristic peak corresponding to the presence of nitrogen species is observed in the spectrum of NRGO1100, which is absent in that of GO, confirming successful doping of nitrogen species **(Figure 4.3(c))**. The large oxygen peak is observed in the spectrum of GO due to the oxygen groups formed during the Hummers' method, while a much smaller oxygen peak in the spectrum of NRGO1100 is indicative of reduced oxygen content due to the thermal reduction during the synthesis. The high-resolution N1s spectrum of NRGO1100 reveals the atomic percent of nitrogen to be ca. 3.5 %, with a distribution of nitrogen into three species: pyridinic N, pyrrolic N, and quaternary N, based on spectral de-convolution **(Figure 4.3(d))**.[118, 119] As the synthesis temperature of

NRGO is increased, the nitrogen content decreases due to the decomposition of the nitrogen species at higher temperatures, consistent with previous reports **(Table 4.1)**.[112, 120]

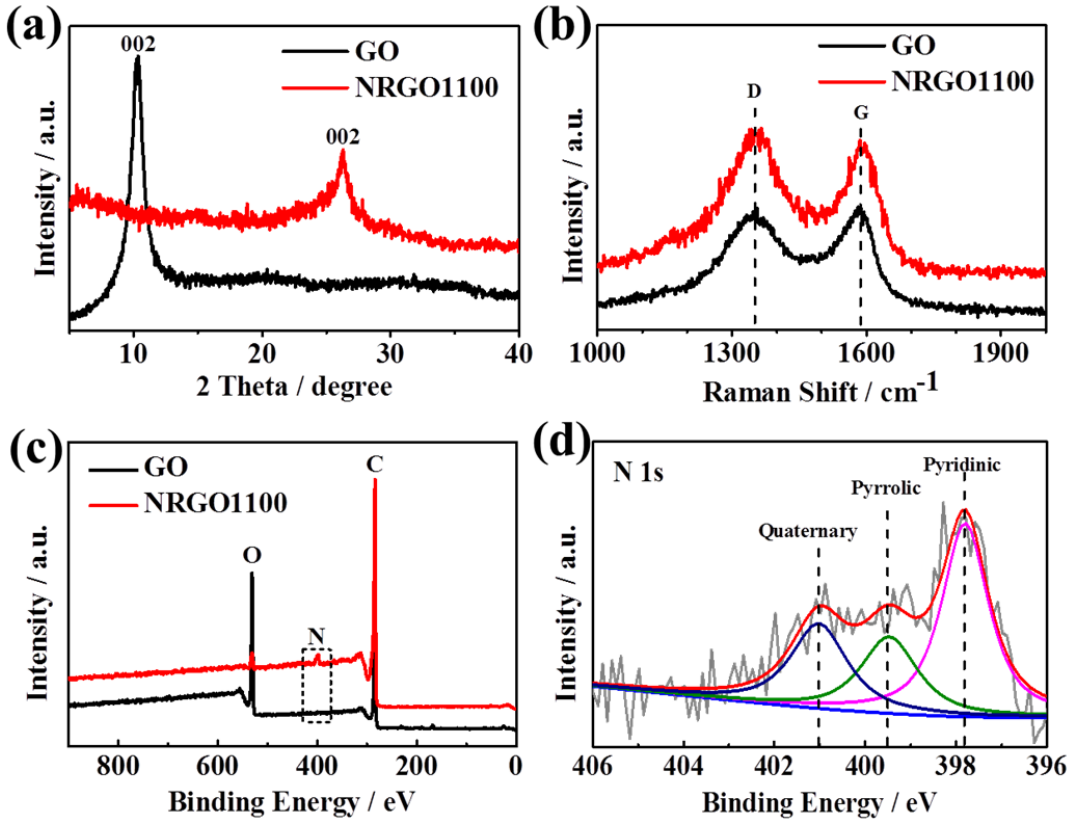


**Figure 4.3** (a) XRD patterns of GO and NRGO1100. (b) Raman spectra of GO and NRGO1100. (c) Full XPS spectra of GO and NRGO1100. (d) High-resolution N 1s XPS spectrum of NRGO1100. (The gray line is the original signal, and the red curve is the result of the curve fit. Blue, green, and pink peaks correspond to quaternary, pyrrolic, and pyridinic nitrogen species, respectively, after de-convolution.).

**Table 4.1** Atomic percent nitrogen content and its distribution into different nitrogen species obtained from de-convolution of the N1s XPS peaks. The numbers in brackets indicate the percentage of the nitrogen species in the three species.

| Sample | N content, at% | pyridinic N, at% | pyrrolic N, at% | quaternary N, at% |
|---|---|---|---|---|
| NRGO800 | 5.80 | 3.10 (53.5 %) | 1.32 (22.8 %) | 1.37 (23.7 %) |
| NRGO900 | 5.44 | 2.98 (54.8 %) | 1.14 (20.9 %) | 1.32 (24.2 %) |
| NRGO1000 | 5.18 | 2.58 (49.9 %) | 1.23 (23.8 %) | 1.36 (26.3 %) |
| NRGO1100 | 3.50 | 1.59 (45.4 %) | 0.69 (19.6 %) | 1.22 (35.0 %) |

To investigate the effect of synthesis temperature on the morphology of the graphene nanosheets, they have been prepared at temperatures 800, 900, 1000, and 1100 $^{o}$C. A trend is clearly observed from the SEM analysis where the increase in the synthesis temperature increases the degree of wrinkling and the degree of expansion of the sheets **(Figure 4.4(a), (b), (c), and (d))**. This is again most probably caused by more energetic release of the gases from the sheets during thermal reduction at elevated temperatures. Such a simple control over the morphology of these graphene sheets by a temperature change highlights the practical feasibility of this synthesis technique in obtaining the correct morphology to achieve high ORR catalytic activity.

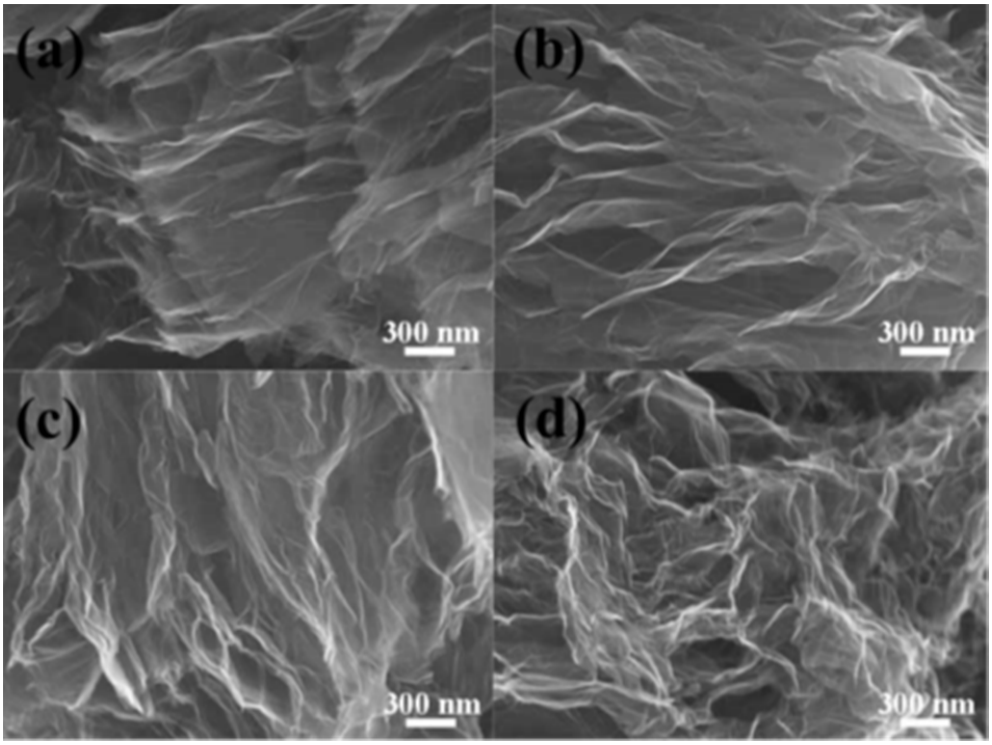


**Figure 4.4** SEM images of NRGO synthesized by one-step thermal reduction and nitrogen-doping at various temperatures of (a) 800 $^{o}$C, (b) 900 $^{o}$C, (c) 1000 $^{o}$C, and (d) 1100 $^{o}$C

To elucidate the effect of heating rate used during the synthesis on the ORR activity of the graphene nanosheets, RDE measurements have been performed with NRGO1100-S and compared to that of NRGO1100 **(Figure 4.5 (a))**. With much negative onset potential, which is indicative of much higher overpotential, NRGO1100-S performed poorly with smaller current densities observed at every potential. The difference in the limiting current densities is most likely due to varying degrees of reaction kinetics for ORR. The number of electron transferred for NRGO1100-S is relatively less than NRGO1100 which is also observed with the polarization curve for NRGO1100-S that looks like two step reaction. In addition, the superior performance of NRGO1100 is likely ascribed to its open structure as confirmed by the SEM analysis, which

allows better diffusion of the electrolyte for highly efficient ORR activity. The RDE measurements of the graphene sheets produced at different temperatures have also been conducted to study the effect of synthesis temperature on the ORR activity **(Figure 4.5 (b))**. As expected, the graphene nanosheets show improvement in both the onset and half-wave potentials, and larger observed current densities as the synthesis temperature is increased. As discussed in **Figure 4.3**, this trend is ascribed to higher degrees of expansion of the graphene sheets at higher temperatures providing the best morphology for highly efficient ORR activity. Furthermore, since the heterogeneous nitrogen atoms incorporate into the graphene sheets as "defects", larger nitrogen contents at lower temperatures disrupt the graphitic network, which likely have been detrimental to the ORR performance. Also, graphitization of the carbon atoms during the synthesis may play an important role in governing the ORR activity as it may be related to electrical properties. At high temperatures, especially for NRGO1100, the graphitization has probably occurred more readily due to higher kinetics. Combined with a moderate amount of heterogeneously doped nitrogen atoms from the ammonia treatment, NRGO1100 likely formed highly efficient active sites for ORR without losing electrical conductivity, resulting in best ORR performance. The kinetics study of ORR of NRGO1100 is investigated by obtaining polarization curves at various rotation rates **(Figure 4.5 (c))**. The Koutechý-Levich (K-L) plot drawn based on polarization curves of NRGO1100 shows parallel lines that correspond to different potentials, which is indicative of first-order kinetics of NRGO1100 **(Figure 4.5 (d))**. At the ORR potentials of -0.50 V, -0.55 V, and -0.60 V (vs. SCE), the determined value of *n* is 4.0, which is an indication of highly efficient electrochemical reduction of $O_2$ occurring via a pseudo four-electron reduction pathway ($O_2 + 2H_2O + 4e^- \rightarrow 4OH^-$). Typically, ORR that occurs on carbon

electrodes involves less than 4 electrons, but there also have been reports that up to 4 electron reduction pathways take place on nitrogen-containing carbon electrodes.[121-123]

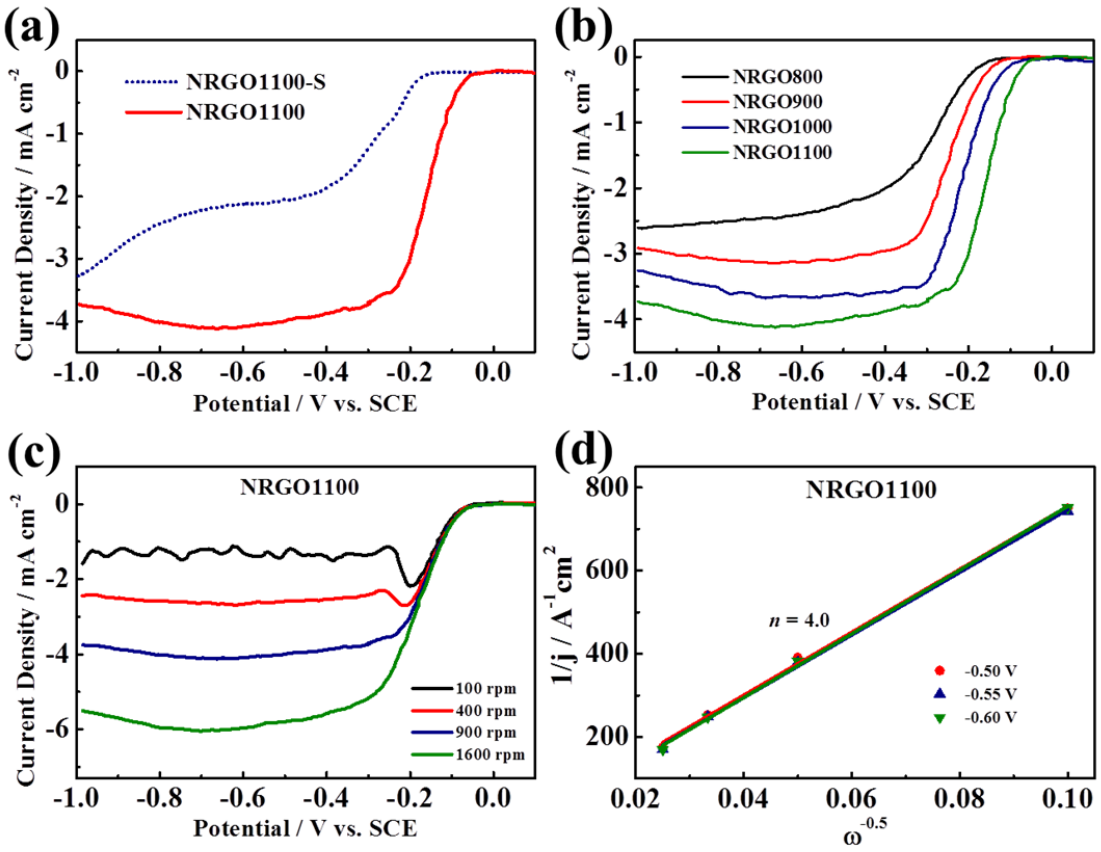


**Figure 4.5** ORR polarization curves of (a) NRGO1100-S and NRGO1100, and (b) NRGO800, NRGO900, NRGO1000 and NRGO1100 obtained at 900 rpm and 10 mV $sec^{-1}$ scan rate in 0.1 M KOH. (c) RDE measurements of NRGO1100 obtained at rotation rates of 100, 400, 900, and 1600 rpm. (d) Koutecký-Levich (K-L) plot of NRGO1100 obtained at potentials -0.50, -0.55, and -0.60 V vs. SCE.

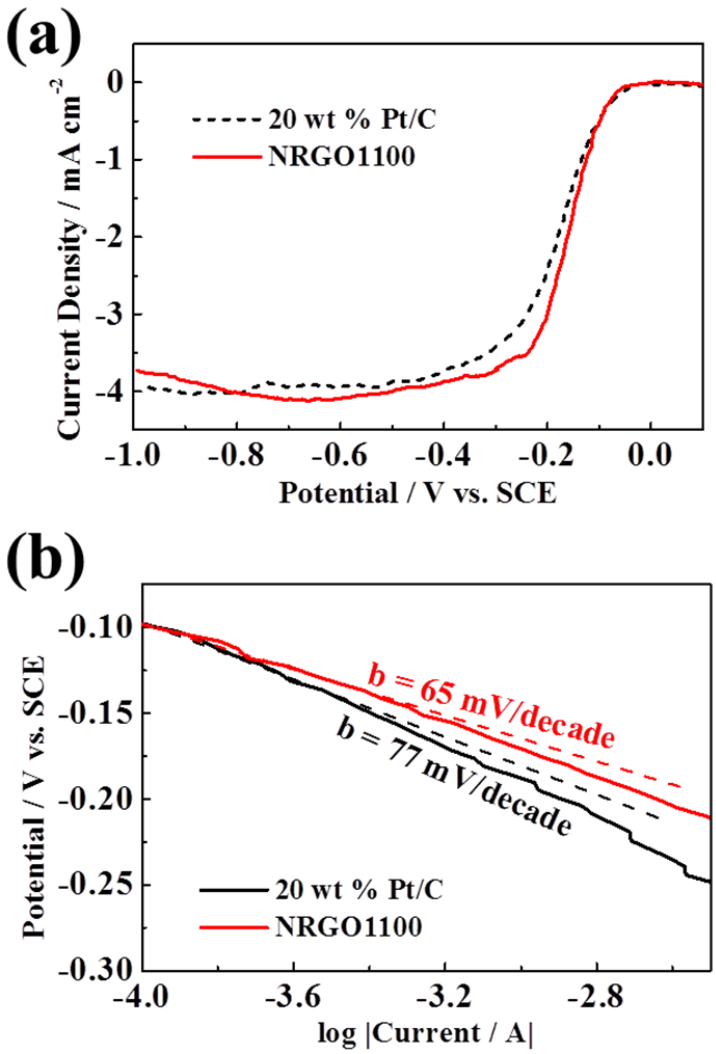


**Figure 4.6** (a) ORR polarization curves of Pt/C and NRGO1100 obtained at 900 rpm. (b) Tafel plot of Pt/C and NRGO1100 at the high potential region.

The practical viability is demonstrated by comparing the excellent ORR activity of NRGO1100 to that of state-of-the-art commercial carbon supported 20 wt. % platinum (Pt/C) catalyst **(Figure 4.6 (a))**. The onset and half-wave potentials of -0.050 V (vs. SCE) and -0.164 V (vs. SCE), respectively, are demonstrated by NRGO1100, which are very comparable to those of

Pt/C (-0.039 V and -0.179 V (vs. SCE), respectively). Furthermore, the analysis of the Tafel plot have resulted in a shallower slope of 65 mV/decade for NRGO1100 compared to that of Pt/C (77 mV/decade), which is indicative of superior ORR kinetics of NRGO1100 in the high overpotential regime **(Figure 4.6 (b))**. This outstanding ORR performance of metal-free carbon-based NRGO1100 electrocatalyst with precisely tailored morphology has been possible with a well-controlled facile synthesis technique. This bolsters our earlier speculation that better graphitization at higher synthesis temperatures contribute in improving the ORR activity due to morphological advantages as well as superior electric properties attained by the graphene nanosheets that facilitate in the charge transfer process during ORR catalysis.

## 4.4 Summary

In this chapter, I present the one-step synthesis technique by a rapid heating to prepare nitrogen-doped reduced graphene oxide (NRGO) sheets. The morphologies of NRGO are well-controlled by the heating temperature. The temperatures of 800, 900, 1000, and 1100 $^{o}$C were applied to GO and electron microscope images revealed that the increase of the synthesis temperature increases the degree of wrinkling and the degree of expansion of the sheets. It was also found that the morphology influenced the catalytic activity towards ORR. In a half-cell testing, NRGO1100 demonstrated comparable ORR activity to that of state-of-the-art 20 wt % Pt/C catalyst. This outstanding catalytic performance and novel morphology of metal-free carbon-based graphene nanosheets are promising for developing new class of bi-functional catalysts for metal-air batteries.

# 5. Electrospun Porous Perovskite Oxide/Nitrogen-Doped Graphene Composite as Bi-functional Catalyst for Metal-Air Batteries

## 5.1 Introduction

In this chapter, a uniquely structured composite bi-functional catalyst consisting of porous nanorods perovskite oxide and nitrogen-doped reduced graphene oxide (NRGO) is introduced, utilizing perovskite oxide of $La_{0.5}Sr_{0.5}Co_{0.8}Fe_{0.2}O_3$ with porous rod shape (LSCF-PR) as an OER catalyst. Perovskite oxides have received much attention as efficient electrode materials due to their relatively high electronic and ionic conductivity as introduced in Chapter 2.[19, 20, 60, 124] Shao–Horn and co-workers have reported the trends in ORR and OER activities of perovskite oxides, introducing underlying design principles for perovskite based electrocatalysts.[15, 16, 21] Additionally, they highlighted the importance of large surface areas on perovskite catalyst activity, particularly towards the OER. Drawing on this, Xu et al.[18] proposed porous $La_{0.75}Sr_{0.25}MnO_3$ nanotubes by electrospinning, focusing on the catalytic activities in organic electrolytes, while Zhao et al.[17] produced mesoporous perovskite $La_{0.5}Sr_{0.5}CoO_{2.91}$ nanowires by a multistep microemulsion method. Nevertheless, further improvements to the oxygen catalysis are still necessary in order to utilize them as practical bi-functional catalysts. In addition, it has been suggested that LSCF would be a good OER catalyst since previous reports which introduced Sr-doping and Fe-doping in $LaCoO_3$ perovskite oxide showed enhancement in the catalytic activity.[19, 125]. Having said this, the nanostructured LSCF-PR/NRGO composite characterized physicochemically and electrochemically presents a new class of bi-functional

catalyst for rechargeable metal-air batteries. Particularly, the facile electrospinning method produces homogeneous nano-structured perovskite materials with unique porous nanorod morphology. NRGO prepared using the thermal annealing method in the presence of $NH_3$ as described in Chapter 4 is then incorporated with LSCF-PR to simultaneously provide ORR activity and act as a conductive support.[126] For the first time, these nanomaterials are coupled into a novel hybrid design to produce a bi-functional catalyst with excellent activities towards both the ORR and OER, and superior durability, rendering LSCF-PR/NRGO as a highly promising electrode material for the next generation rechargeable metal-air battery systems.

## 5.2 Experimental

Perovskite oxide of LSCF-PR was prepared by electrospinning method with metal precursors and polymer solution. The solution was prepared by completely dissolving $La(NO_3)_3 \bullet 6H_2O$, $Sr(NO_3)_2$, $Co(NO_3)_2 \bullet 6H_2O$ and $Fe(NO_3)_3 \bullet 9H_2O$ in $H_2O$, $C_2H_5OH$ and DMF with 2:5:4 mass ratio along with 15.4 wt.% polyvinylpyrrolidone (PVP). The solution was electrospun at a distance of 15 cm between the needle tip of syringe and a ground Al foil collector with an applied voltage of 23 kV using home-made D.C. power supply. The injection rate was controlled to 0.5 mL $min^{-1}$ by a syringe pump (New Era Pump System Inc. Model No. NE-300). The electrospun fibers were dried at 60 $^{o}$C in an oven overnight and collected. To obtain perovskite oxide of LSCF-PR, the collected fibers were calcined at 700 $^{o}$C for 3hr in air. As control materials, LSCF-NP was prepared using the same electrospinning solution, and LCO-NP was prepared by only using $La(NO_3)_3 \bullet 6H_2O$ and $Co(NO_3)_2 \bullet 6H_2O$ dissolved in the same solvent as LSCF-PR. Both of these solutions were directly calcined using the same condition of

700 $^{o}$C for 3 hr with a heating rate of 1 $^{o}$C min$^{-1}$ as LSCF-PR. LSCF-PR/NRGO composite was prepared by dispersion in 0.3 wt.% Nafion/ethanol solution. 30 wt.% LSCF-PR and 70 wt.% NRGO were mixed in the Nafion solution with total concentration of 4 $mg_{catalyst}$ ml$^{-1}$. The solution was sonicated for 3 hr until no precipitation was shown. To examine electro-catalytic activities, the solution was coated onto a glassy carbon rotating disk electrode (RDE) with catalyst loading of 0.41 mg cm$^{-2}$. As control catalysts, NRGO or Pt/C catalyst electrode was prepared in the same way.

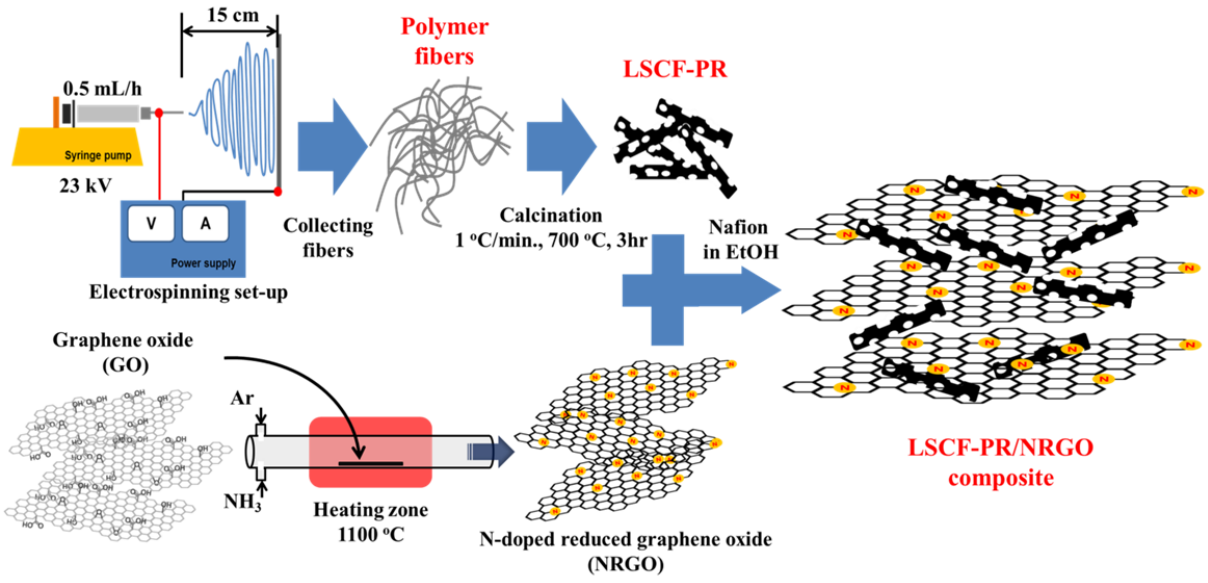


**Figure 5.1** Schematic illustration of the preparation of LSCF-PR/NRGO composite.

## 5.3 Result and discussion

**Figure 5.1** illustrates the preparation of LSCF-PR/NRGO hybrid, whereby PVP-metal based fibers are obtained by electrospinning and then subjected to a calcining heat treatment at 700 $^{o}$C for 3 hrs in air to decompose PVP and obtain crystalline LSCF-PR. NRGO is prepared via rapid annealing of graphite oxide (GO) under Ar/$NH_3$ gas flow. After the preparations of LSCF-PR and NRGO, the two materials are mixed in ethanol-diluted Nafion solution by sonication to finally obtain LSCF-PR/NRGO hybrid bi-functional catalysts.

**Figure 5.2(a)** presents SEM image of the electrospun fibers before calcination of LSCF-PR, which confirms the electrospinning conditions produces bead- and aggregate-free homogeneous fibers. Upon calcination however, the morphology of the fibers changes to a uniform rod shape, as shown in **Figure 5.2(b) and (c)**. During calcination, PVP is decomposed and the metal precursors stabilize into the unique porous nanorod structure. The TEM image in **Figure 5.2(d)** further highlights the nanorods having the porous rod morphology, with clearly observable pores on the surface highlighted by the white arrows.

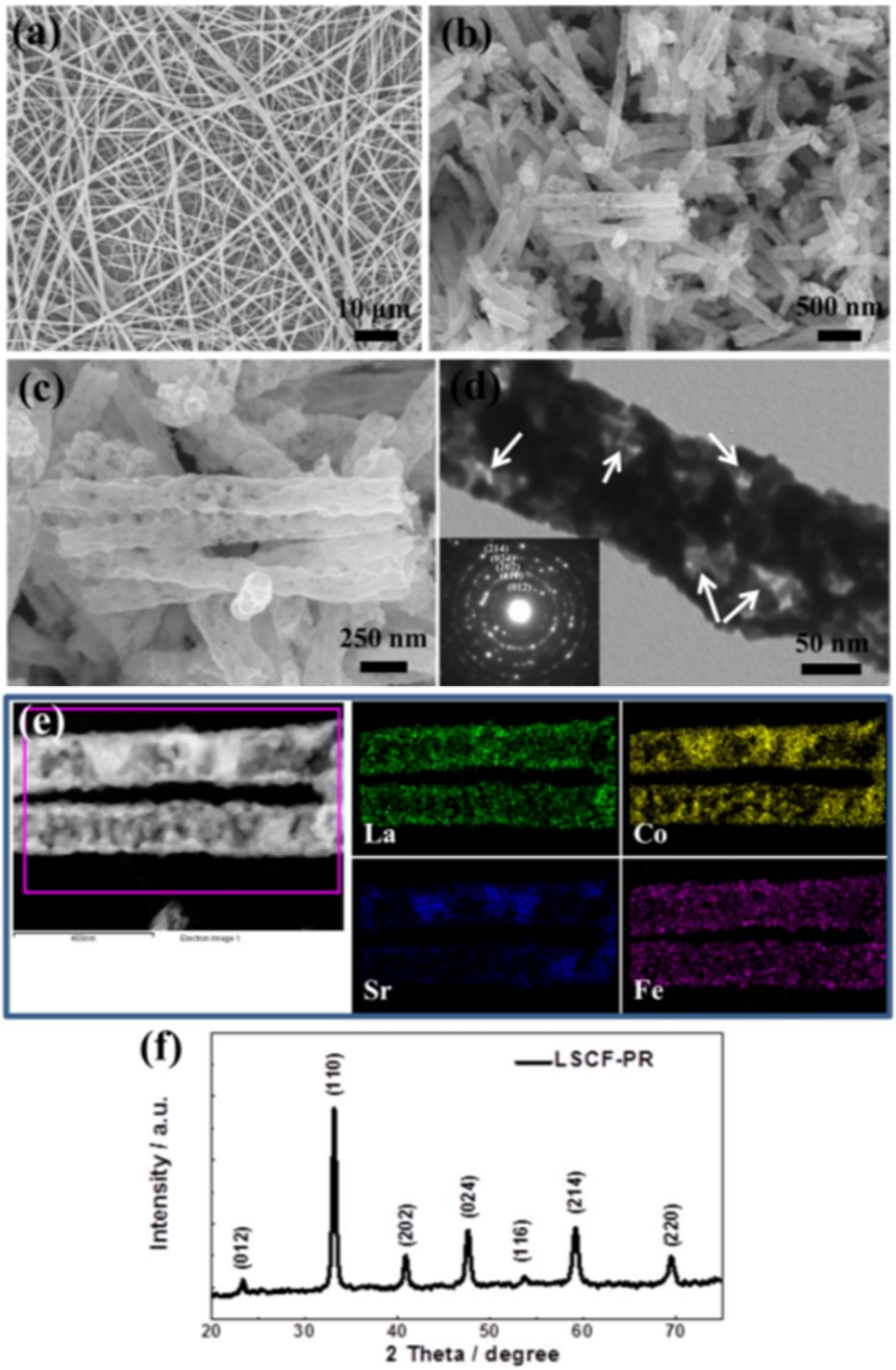


**Figure 5.2** SEM images of (a) electrospun fibers containing metal precursors and PVP, (b,c) LSCF-PR after calcination of the fibers; (d) TEM image of LSCF-PR (inset: SAED pattern); (e) elemental mapping by EDS from TEM; and (f) XRD pattern of LSCF-PR.

Elemental analysis of LSCF-PR by energy-dispersive x-ray spectroscopy (EDS) presents the distribution of the atoms as shown in the color map in **Figure 5.2(e)**. The EDS element images verify that all elements in LSCF are detected and well-dispersed throughout the porous nanorod structure. To determine the crystalline structure of the synthesized LSCF-PR, the X-ray diffraction (XRD) pattern (**Figure 5.2(f)**) was analyzed and found to be characteristic of a single phase crystalline perovskite oxide with a rhombohedrally distorted structure and space group R-3c (JCPDS card no. 48-0124), consistent with previous reports having the similar chemical composition.[17, 19, 127, 128] This is further evidenced by the select area electron diffraction (SAED) pattern **(Figure 5.2(d) inset)** and high resolution TEM (HR-TEM) image **(Figure 5.3)**. The *d*-spacing measured by the observed fringes in the HR-TEM image are 0.270 and 0.229 nm, consistent with the theoretical *d*-spacing of the (110) and (202) planes of LSCF perovskite oxide, respectively. However, refinement of the XRD pattern may need to confirm accurate crystal phase of LSCF for the future work.

As an effective substrate for good distribution of LSCF-PR and excellent ORR catalyst,[65, 129] NRGO is synthesized via a facile heat treatment which makes it highly active towards the ORR.[126] SEM and TEM images present a two-dimensional voile-like architecture of graphene sheets which effectively provides electron conductive pathways in an electrode (**Figure 5.4(a) and (b)**). Un-doped RGO is also prepared by the same method except in absence of $NH_3$ as a comparison. Distinguishing between RGO and NRGO based on electron microscope characterization is difficult,[37] hence X-ray photoelectron spectroscopy (XPS) has been conducted and confirmed nitrogen content and its configurations within the graphitic layer of NRGO sheets, compared with RGO **(Figure 5.5)**.[130]

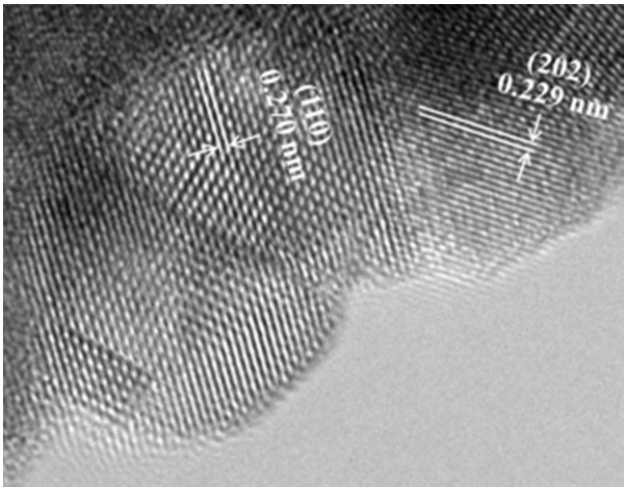


**Figure 5.3** High resolution TEM (HR-TEM) image of LSCF-PR.

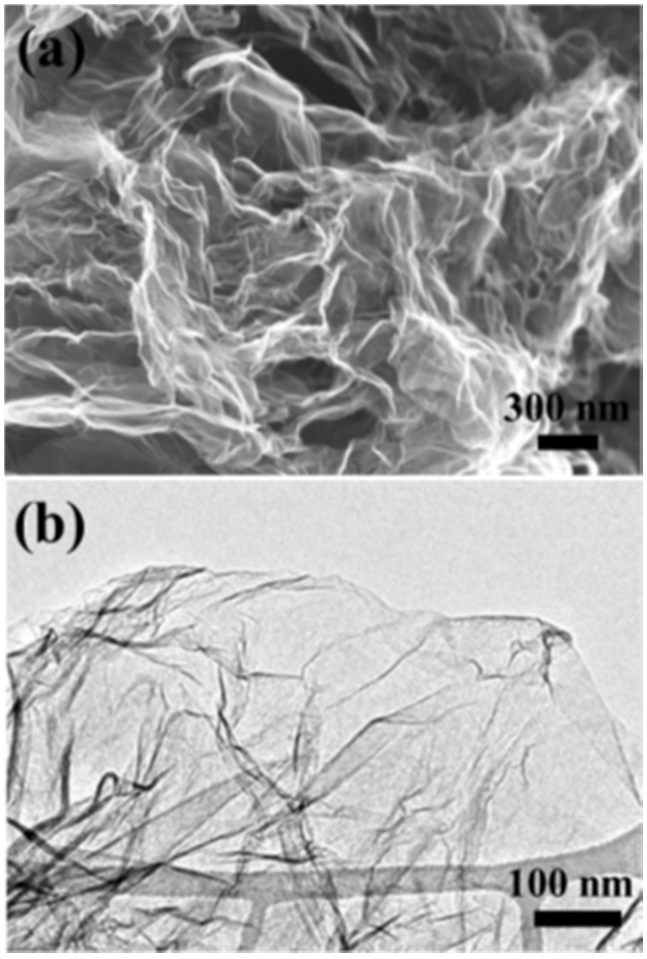


**Figure 5.4** SEM and TEM images of (a,b) NRGO.

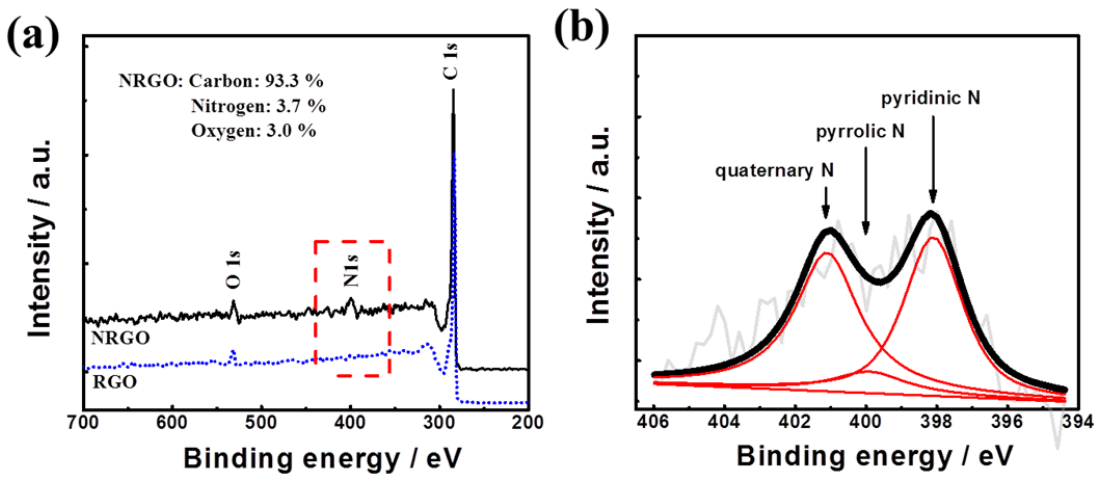


**Figure 5.5** (a) Full XPS spectra of RGO and NRGO, and (b) de-convoluted high resolution N 1s XPS spectrum of NRGO.

The full XPS spectrum of NRGO exhibits peaks at 284.6 eV of C 1s and O 1s peak at 531.6 eV and additionally the spectrum shows that nitrogen is successfully doped in the graphene sheets as observed by N 1s peak at ca.400 eV **(Figure 5.5(a))**.[130] The atomic percentages in NRGO are calculated using the spectrum to be 93.3, 3.0 and 3.7 % of carbon, oxygen and nitrogen, respectively. The doped nitrogen is believed to generate defective structure in the graphitic layer which is the active sites for the oxygen reactions. Moreover, the high resolution spectrum of N 1s is also investigated as shown in **Figure 5.5(b)** since it is proposed that electrochemical catalysis of oxygen depends on nitrogen configuration. After the de-convolution of the high resolution, it reveals that nitrogen possesses pyridinic N (398.1 eV), pyrrolic N (399.9 eV), and quaternary N (401.1 eV) with 1.6, 0.3 and 1.8 % of atomic percentages, respectively. According to literature, the quaternary N mainly plays role of catalyzing oxygen reduction reaction.[131]

To investigate the electrode structure of LSCF-PR/NRGO composite prepared by mixing in the Nafion solution, the composite are coated on an aluminum foil by the same procedure as

the preparation of the working electrode for all electrochemical testing. The SEM image in **Figure 5.6(a)** shows LSCF-PR well-dispersed throughout the sheets of NRGO. Moreover, a magnified image in **Figure 5.6(b)** clearly shows some LSCF-PR buried under the graphene sheets (dotted arrows) and others exposed on the surface (solid arrows). The cross-sectional SEM image of LSCF-PR/NRGO electrode is also provided in **Figure 5.6(c)** showing a three-dimensional structure with well-distributed LSCF-PR throughout the sheets of NRGO. The magnified cross-section image shows consistent morphologies observed with in-plane of the composite with both buried and exposed LSCF-PR incorporated in the graphene sheets **(Figure 5.6(d))**. It is believed that this novel structure of the composite catalyst is attributed to the amphiphilic property of Nafion effectively combines hydrophobic NRGO with relatively hydrophilic LSCF-PR since the Nafion ionomer has been known to be a good surfactant for dispersing carbon-based structures such as CNT and graphene due to its amphiphilic property.[132, 133]. Additionally, LSCF nanoparticles (LSCF-NP) and $LaCoO_3$ nanoparticles (LCO-NP) have also been synthesized as comparisons to compare the morphological and compositional effects. The morphology and crystal phase of LSCF-NP and LCO-NP is also characterized by SEM, TEM and XRD **(Figure 5.7 and 5.8, respectively)**. While LSCF-NP has the same XRD pattern with LSCF-PR, LCO-NP has a single phase of a rhombohedral structure with R-3c space group presenting all lattice planes corresponding to those in JCPDS card no 48-0123. While these materials demonstrate the same crystal structures, LSCP-NP exhibits irregularly shaped nano-sized particles with some aggregation. The specific surface area, pore size distribution and pore volume of LSCF-PR and LSCF-NP are analyzed by nitrogen adsorption and desorption isotherms at 77 K using the Brunauer–Emmett–Teller (BET) and Barrett–Joyner–Halenda (BJH) methods **(Figure 5.9)**. The BET surface area and BJH total pore

volume of LSCF-PR is 36.5 $m^2$ $g^{-1}$ and 0.139 $cm^3$ $g^{-1}$, respectively, which has much larger surface areas compared to the respective values of LSCF-NP (22.6 $m^2$ $g^{-1}$ and 0.113 $cm^3$ $g^{-1}$), owing to the nanorod morphology with high porosity as observed by the electron micrographs. This directly shows that electrospinning and subsequent calcination process are highly beneficial for the preparation of perovskite oxide based materials with significantly increased surface area.

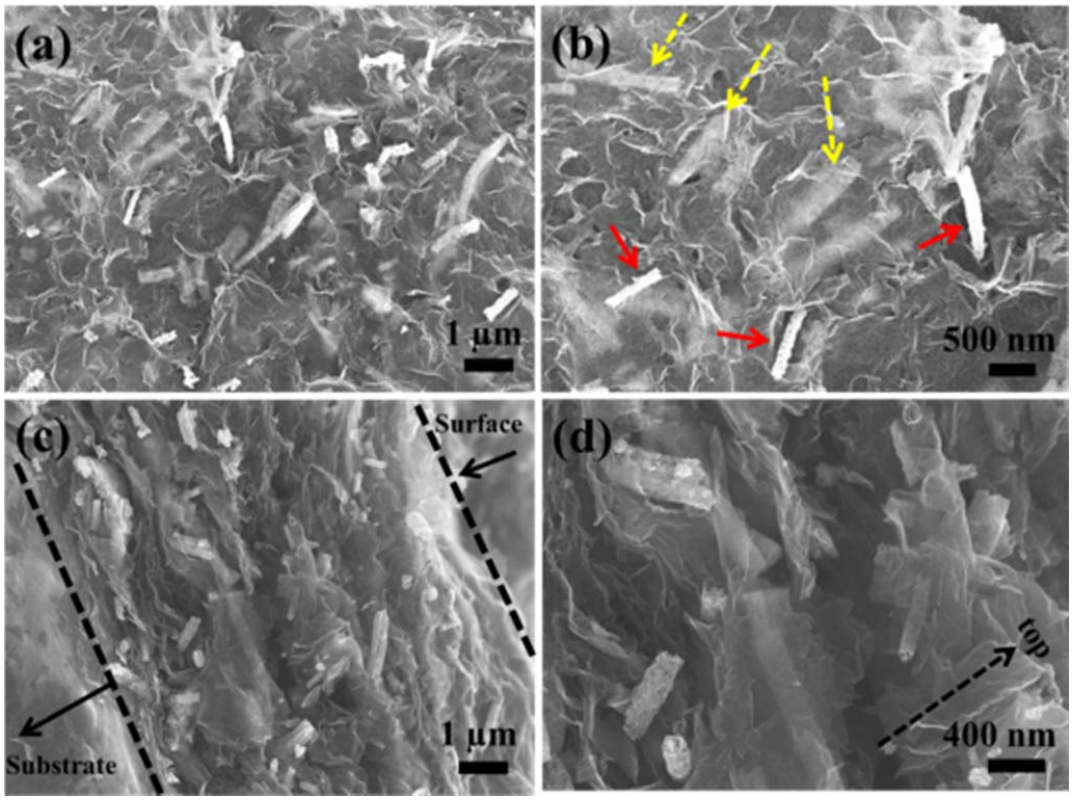


**Figure 5.6** SEM images of (c,d) LSCF-PR/NRGO composite; and cross-sectional SEM images of (e,f) LSCF-PR/NRGO composite.

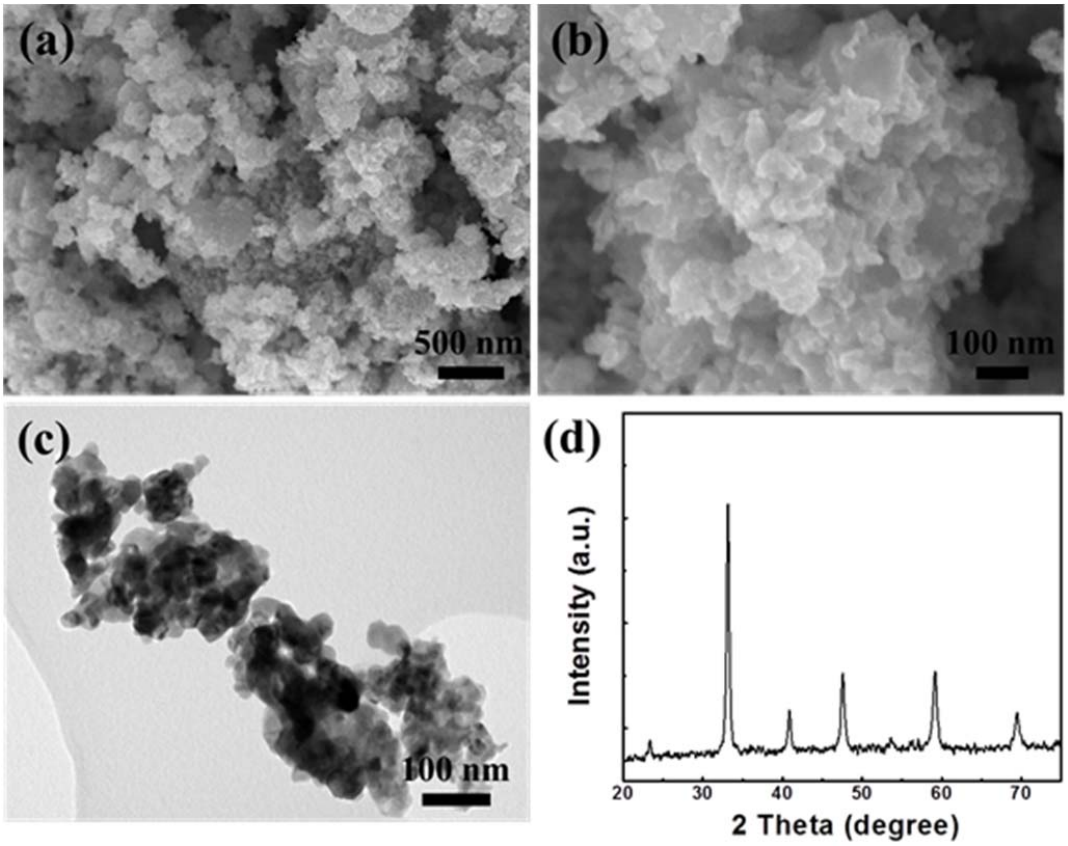


**Figure 5.7** (a) Low magnification and (b) high magnification SEM image, (c) TEM image of LSCF-NP; and (d) XRD pattern of LSCF-NP.

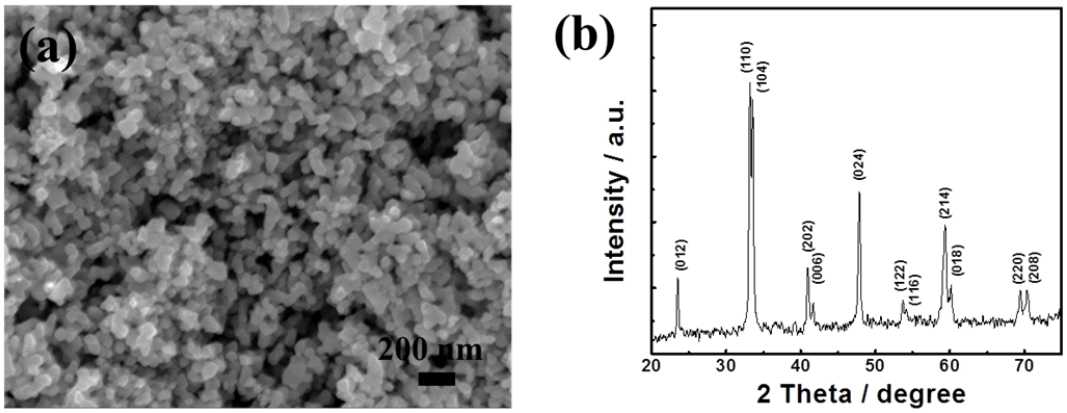


**Figure 5.8** (a) SEM image and (b) XRD pattern of LCO-NP.

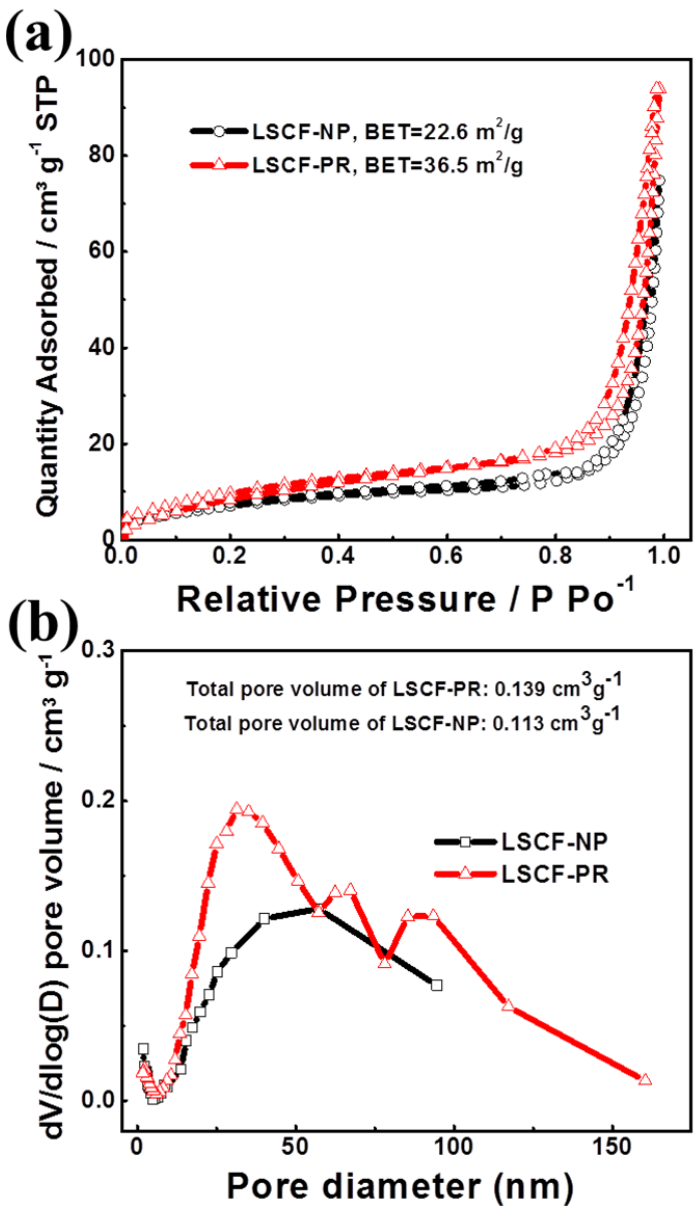


**Figure 5.9** (a) $N_2$ adsorption–desorption isotherms and (b) pore size distribution of LSCF-PR and LSCF-NP.

The electrochemical behaviors of LSCF-PR, LSCF-NP and LCO-NP towards the ORR ($O_2 + 2H_2O + 4e^- \rightarrow 4OH^-$) and OER ($4OH^- \rightarrow O_2 + 2H_2O + 4e^-$) are investigated by half-cell testing in 0.1M KOH. **Figure 5.10(a)** displays full range polarization curves of ORR and OER of LSCF-PR, LSCF-NP and LCO-NP in $O_2$-saturated 0.1M KOH between 0.4 V and 2.0 V (vs. RHE) scanned at 10 mV $s^{-1}$, showing cathodic and anodic currents associated with ORR and OER, respectively. While the metal oxides show relatively low current densities that are comparable to each other, clear differences are observed in OER activities with prominent current densities.[63, 134] The OER potentials are measured at 1 mA $cm^{-2}$, the current density at which distinguishable electrochemical reaction kinetics occurs apart from the double-layer capacitance, where LSCF-PR shows much lower potential than those of LSCF-NP and LCO-NP **(Figure 5.10(a) inset)**. The increased OER activity of LSCF-PR is also evidenced by significantly enhanced current densities observed at all electrode potentials investigated up to 2.0 V. The higher current densities at 1.0 V (vs. SCE) and reduced overpotentials at 1 mA $cm^{-2}$ for OER of LSCF-PR compared to its nanoparticles counterpart are attributed to the porous nanorod morphology which provides larger surface areas significantly enhancing the active site exposure.[21] In addition, the porous structure also facilitates the diffusion of hydroxide ions during the electrocatalytic reaction which accelerates the kinetics of OER. With respect to the compositional advantages of LSCF-PR, the same perovskite phased LCO is significantly outperformed due to the Sr- and Fe-substitution which improve the catalytic activity towards the OER.[19, 125] The effectiveness of combining LSCF-PR and NGRO as a bi-functional catalyst is shown in **Figure 5.10(b),** where the polarization profile of the composite shows far superior ORR behavior compared to RGO and Vulcan carbon (VC) composites.

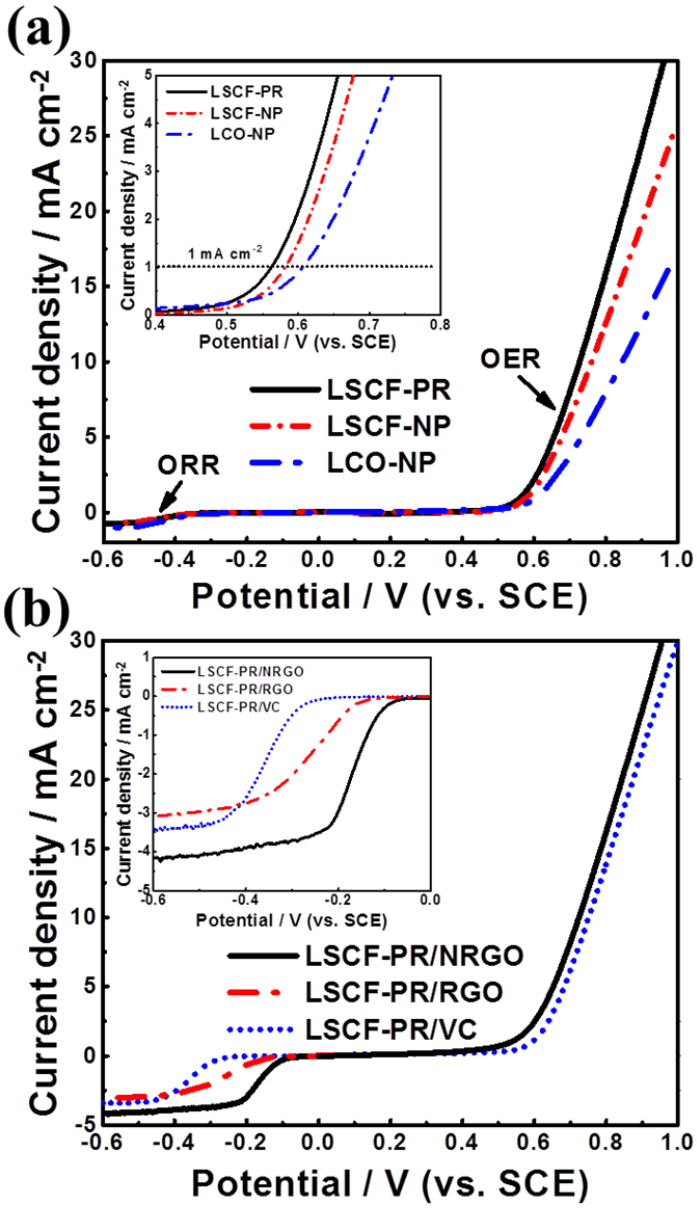


**Figure 5.10** (a) ORR (negative scan) and OER (positive scan) polarization profiles at 900 rpm and 10 mV $s^{-1}$ scan rate of LSCF-PR, LSCF-NP and LCO-NP (inset: magnified OER polarization profiles) and (b) ORR and OER polarization profiles at 900 rpm and 10 mV $s^{-1}$ scan rate of LSCF-PR/NRGO, LSCF-PR/RGO and LSCF-PR/VC composites (inset: magnified ORR polarization profiles).

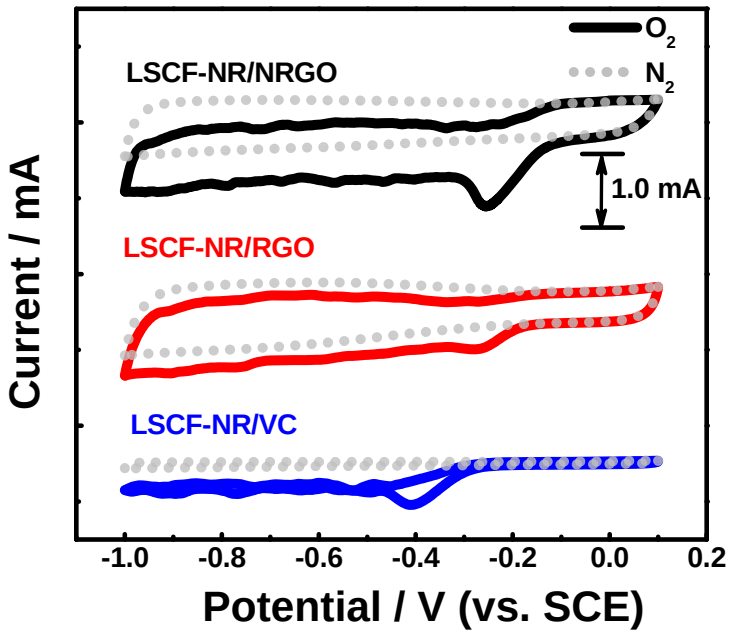


**Figure 5.11** Cyclic voltammograms at scan rate of 50 mV $sec^{-1}$ of LSCF-PR/NRGO, LSCF-PR/RGO and LSCF-PR/VC.

Compared to LSCF-PR tested itself as shown in **Figure 5.10(a)**, combining with a carbon support improves the ORR activity, while the OER activity remains similar to that of free LSCF-PR. In comparing ORR activities, half-wave potential of LSCF-PR/NRGO is 89 and 187 mV higher, and limiting current density at 0.4 V is increased by 1.08 and 0.76 mA $cm^{-2}$ in comparison to LSCF-PR/RGO and LSCF-PR/VC composite, respectively **(Figure 5.10(b) inset)**. The trend of ORR activities are also confirmed by the cyclic voltammograms, as shown in (**Figure 5.11)**.This clearly highlights the benefits of using NRGO support, providing excellent ORR activity in alkaline conditions. Based on these results, the ORR and OER performance of LSCF-PR/NRGO is very similar to NRGO and LSCF-PR, respectively **(Figure 5.12)**.

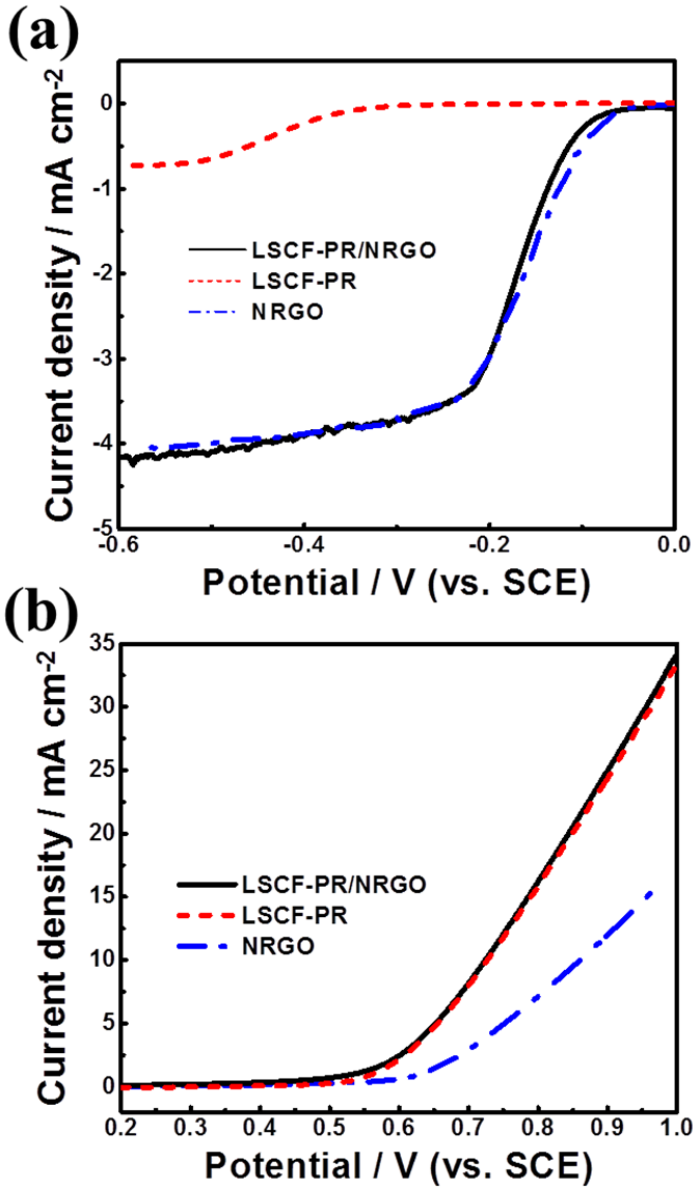


**Figure 5.12** (a) ORR and (b) OER polarization profiles of LSCF-PR/NRGO, LSCF-PR and NRGO at rotation speed of 900 rpm and 10 mV $s^{-1}$ scan rate.

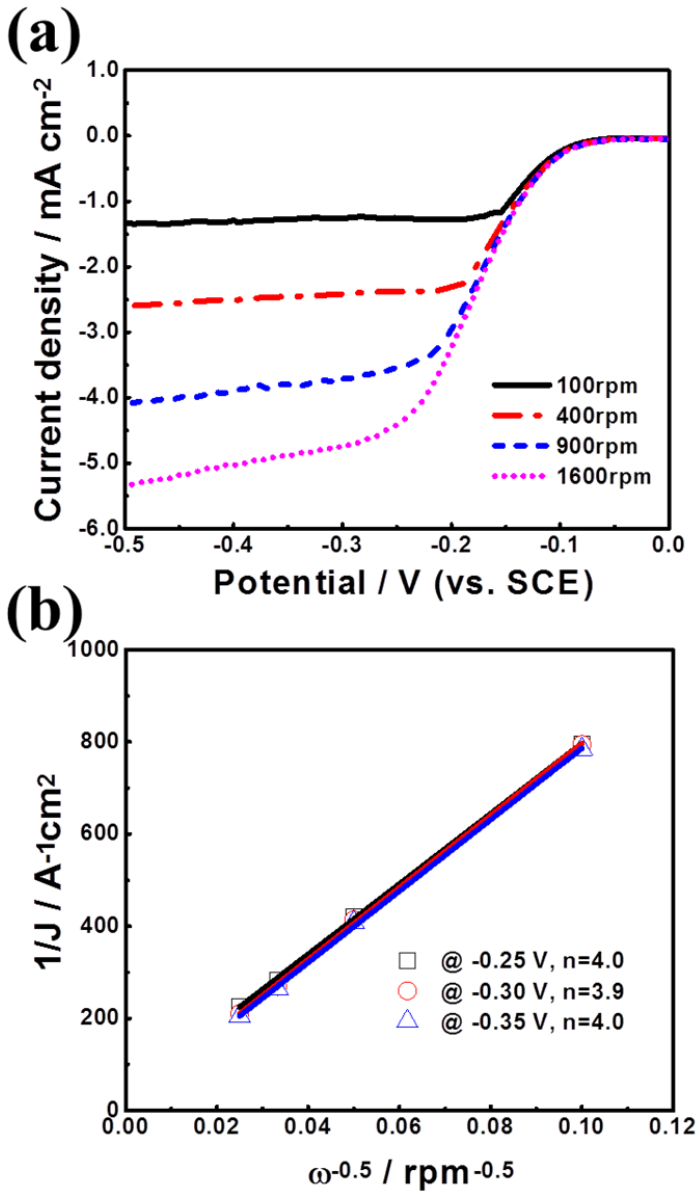


**Figure 5.13** (a) ORR polarization profiles of LSCF-PR/NRGO at various rotation speeds and 10 mV $s^{-1}$ scan rate and (b) its Koutecky-Levich plot at potentials -0.25, -0.30 and -0.35 V)

This clearly confirms that the composite's ORR activity is mainly attributed to NRGO, while the OER activity is responsible for LSCF-PR, indicative of effective bi-functionality of the composite obtained by combining LSCF-PR and NRGO without interfering each other. In addition to the evaluation of the intrinsic ORR activity of LSCF-PR/NRGO catalyst, rotating disk electrode (RDE) measurements at various rotation speeds have been conducted to quantify the number of electrons transferred during the ORR. Based on the RDE measurements, Koutechý-Levich (K-L) plots have been prepared by selecting four different potentials of -0.25, -0.30 and -0.35 V as shown in **Figure 5.13(a) and (b)**, demonstrating calculated *n* values of 3.9 ~ 4.0, and indicating that LSCF-PR/NRGO facilitates ORR by the highly efficient pseudo 4 electron pathway. Lastly, commercial Pt/C catalyst is examined to compare with LSCF-PR/NRGO catalyst as presented in **Figure 5.14(a) and (b)**, which shows ORR performance of LSCF-PR/NRGO comparable to that of Pt/C in terms of limiting current density, and half-wave potential. In addition, the Tafel plot in the ORR potential region results in the slope of 60.0 mV/decade for LSCF-PR/NRGO which is similar to that of Pt/C (58.6 mV/decade) **(Figure. 5.15)**. To study the durability of LSCF-PR/NRGO catalyst, chronoamperometry is carried out at -0.4 V and 0.8 V (vs. SCE) for ORR and OER respectively, at rotation speed of 900 rpm to evaluate the reaction currents. As shown in **Figure 5.16(a) and (b)**, the retention of current density of LSCF-PR/NRGO during ORR and OER is relatively stable compared to that of Pt/C, indicating superior durability of LSCF-PR/NRGO for bi-functional catalytic activity.

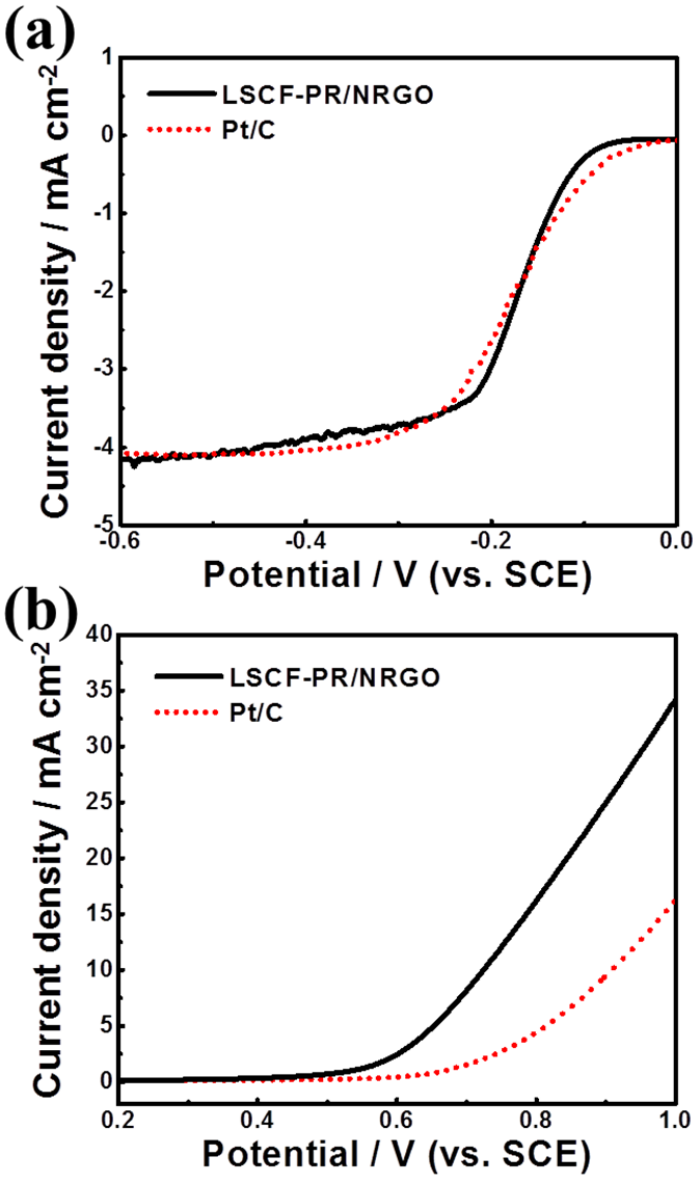


**Figure 5.14** (a) ORR and (b) OER polarization profiles of LSCF-PR/NRGO and Pt/C at rotation speed of 900 rpm and 10 mV $s^{-1}$ scan rate.

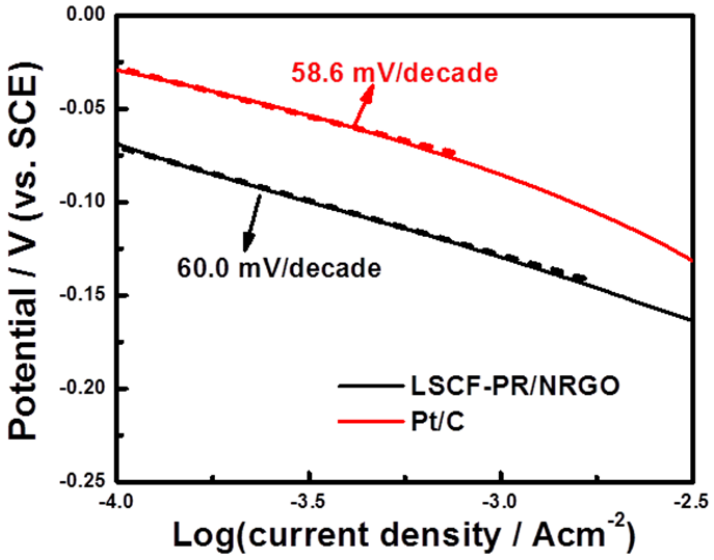


**Figure 5.15** Tafel plots of LSCF-PR/NRGO and Pt/C.

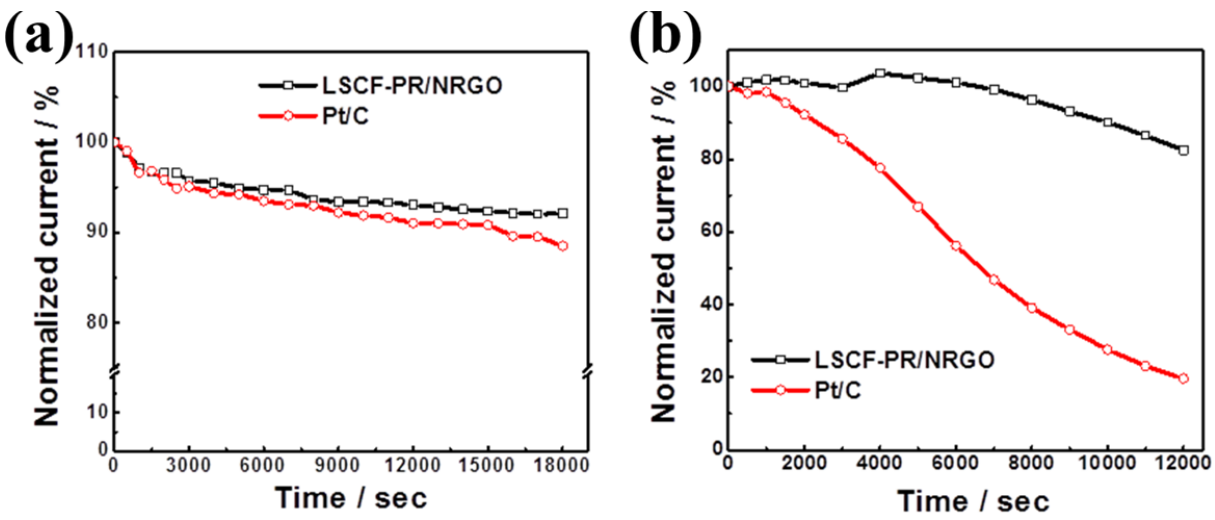


**Figure 5.16** Chronoamperometric responses (percentage of current retained versus operation time) at 900 rpm for (a) ORR (-0.4 V vs. SCE) and (b) OER (0.8 V vs. SCE) of LSCF-PR/NRGO and Pt/C.

## 5.4 Summary

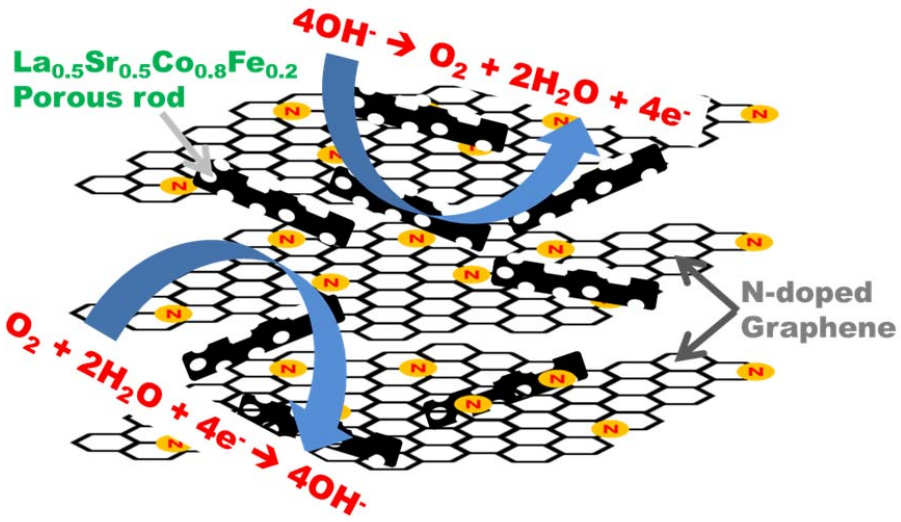


**Figure 5.17** Graphical summary of LSCF-PR/NRGO bi-functional catalyst.

In this study, a new type of bi-functional electrocatalyst has been developed which consists of porous nanorod perovskite oxide and NRGO as a composite graphically summarized in **Figure 5. 17**. The perovskite oxide of LSCF with porous rod morphology (LSCF-PR) was prepared by a novel electrospinning method, followed by calcination and NRGO was prepared as introduced in the Chapter 4. The LSCF-PR uniformly distributed throughout the NRGO sheets creating an efficient LSCF-PR/NRGO composite morphology for oxygen reactions. The crystalline structure and morphology of LSCF-PR, NRGO and the composite were characterized by XRD, electron microscopes, EDS and XPS. By half-cell testing, it was revealed that LSCF-PR with porous morphology enhanced the catalytic activity, compared to that of LSCF nanoparticles, indicating the improved activity is attributed to the higher surface area of the

metal oxide catalyst. Furthermore, the electrochemical performances of the composite revealed excellent catalytic activity and superior durability (compared to Pt/C catalyst) for both the ORR and OER in alkaline electrolyte. It was suggested that LSCF-PR provided the majority of the OER activity, whereas the majority of the ORR active was attributed to NRGO, resulting in a complementary bi-functional catalyst composite arrangement. Therefore, the unique combination of LSCF-PR and NRGO with excellent electrochemical activity is highly promising for rechargeable metal-air batteries.

# 6. Bi-functional N-doped CNT/Graphene Composite as Highly Active and Durable Electrocatalyst for Metal-Air Battery Applications

## 6.1 Introduction

In this chapter, nitrogen-doped carbon nanotubes (NCNT) directly grown on a thermally reduced graphene oxide (RGO) composite as an electrochemical catalyst for rechargeable metal-air batteries is introduced. The main purpose of this study is to investigate the electrochemical performance of directly grown NCNT on RGO as a bi-functional catalyst. To effectively utilize the highly active NCNT, RGO has been chosen as a substrate material since previously reported graphene based catalysts have employed chemically reduced graphene oxide (RGO) as it can be prepared in large quantities and is convenient for combining with metal or metal oxide catalysts as composites.[135-137] However, this study utilizes RGO prepared by the thermal annealing method which is simple and environmental friendly since no additional use of chemical is required for the reduction process.[138] In addition, the thermal annealing technique leads to greater expansion of the graphene sheets and the formation of defects and edge sites in the graphitic network, which have been suggested as highly active catalytic sites for the oxygen reactions.[66, 81] Despite the merits of this simple thermal annealing process, it leads to the loss of long range electrical conductivity since the planar sheets of aromatic carbon network are physically separated by high pressure gas generated during the reaction.[138] To compensate, 1-D NCNTs are utilized to serve the critical role as bridges to electrically connect the discrete graphene sheets and thereby restore the electrical conductivity. Conversely, RGO plays the role

of a substrate to support electrical inter-connections between NCNTs. Moreover, the addition of NCNTs in the graphene sheets as a composite structure can prevent the sheets from restacking during the electrode fabrication. In addition to the structural merits, NCNT can also provide highly catalytic active sites through nitrogen doping. Recently, Ma et al. introduced NCNTs in chemically reduced graphene oxide with a three-dimensional structure as a metal-free electrocatalyst.[136] However, the ORR performance was found to be inferior to that of Pt/C. Also their investigation was limited to the ORR catalytic activity. Presumably, this limited performance was due to their pyridine-derived NCNTs. According to the literature, the ORR performance of pyridine-derived NCNTs cannot surpass that of ethylene diamine (EDA)-derived NCNT due to the higher nitrogen content and the nitrogen configuration of EDA-derived NCNT.[90] Having said this, this study uses EDA as the carbon source to prepare NCNT directly on RGO which leads to outstanding catalytic activity.[90] As a result, the electrochemical catalytic activity of ORR with NCNT/RGO hybrid composite in this study reveals comparable performance to that of state-of-the-art Pt/C catalyst. Furthermore, this hybrid graphitic carbon material demonstrates impressive OER activity with excellent durability, indicating superior ORR activity to Pt/C after a full range cyclic voltammetry (CV). Based on our electrochemical investigation the hybrid NCNT/RGO composite demonstrates feasibility as a bi-functional catalyst for rechargeable metal-air batteries.

## 6.2 Experimental

A brief schematic diagram of the synthesis of NCN/TRGO composite is illustrated in **Figure 6.1** One step thermally reduced graphene oxide (RGO) was synthesized as described in Chapter 4, except $NH_3$ gas.[137] First, graphite oxide (GO) is prepared by a modified Hummer's method from natural graphite, and then GO is placed in a quartz tube outside of the heating area of the horizontal tube furnace. When the temperature of the furnace reaches to 1000 $^oC$ under 100 sccm of Ar gas stream, the quartz tube is quickly shifted for GO to be placed in the heating area in the center of the furnace and kept in that position for 30 ~ 60 seconds. This rapid thermal process have enabled GO to be reduced and exfoliated. The tube is taken back after the thermal treatment outside of the heating area of the furnace and RGO is collected. To prepare NCNT/RGO composite, injection chemical vapor deposition (CVD) method have been conducted to grow NCNT on RGO. The prepared RGO is mixed with 0.25 mL of 0.5 wt% ferrocene (C10H10Fe, Aldrich) dissolved ethanol solution. The mixture of RGO and ferrocene is casted inside of a small quartz tube (18 mm O.D., 100 mm length) and then the small tube is positioned in the heating zone of a horizontal tube furnace. As a precursor of the injection CVD method for NCNT, 1.0 mL of 2.5 wt% ferrocene containing ethylene diamine (C2H8N2, Aldrich) is loaded into a syringe for the injection. The precursor is injected at 0.05 mL $min^{-1}$ to produce NCNT under the nitrogen flow at 100 sccm and 700 $^oC$. After the reaction, the black powder at the position of RGO in the small tube is collected as NCNT/RGO composite. The rest of the black powder is also collected as pure NCNT to compare with the composite. Lastly, NCNT/RGO and NCNT is washed with 0.5 M $H_2SO_4$ solution to leach out the ferrocene derived materials out similar to our previous reports.[90]

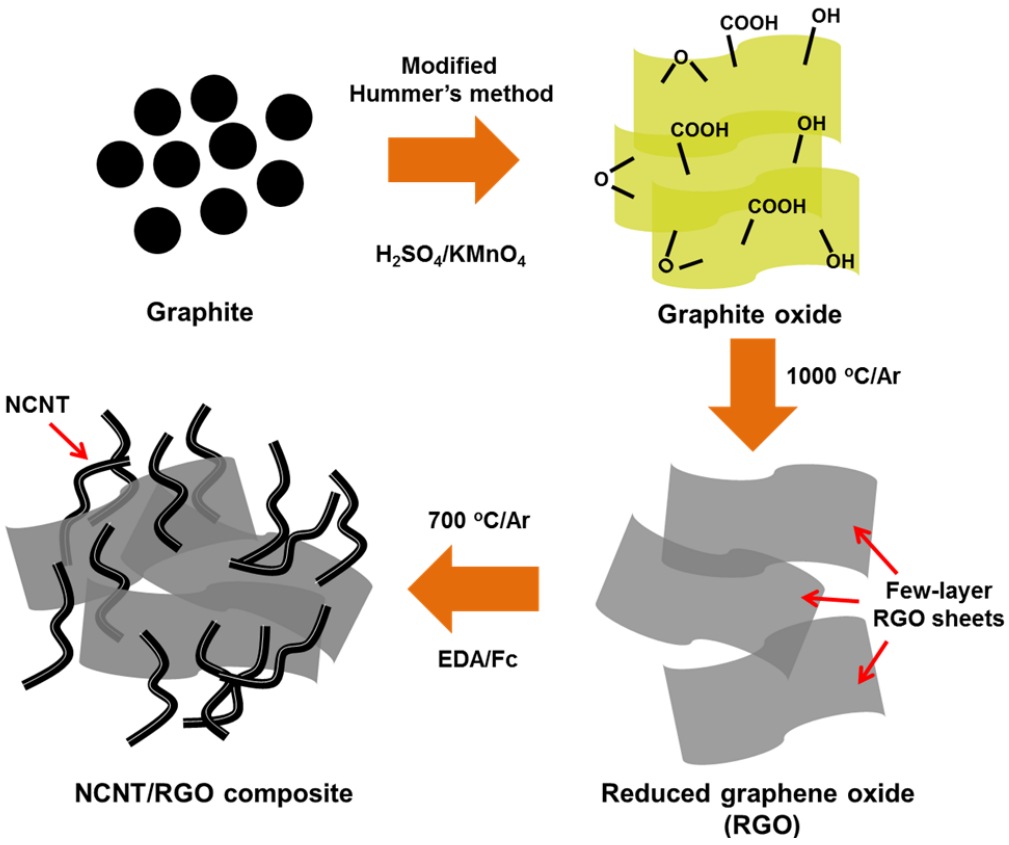


**Figure 6.1** Schematic diagram of the synthesis of NCNT/RGO composite.

## 6.3 Results and discussion

**Figure 6.2(a)** shows the XRD patterns of RGO and NCNT/RGO with a broad diffraction peak for (002) plane in the range 22 ~ 27$^{o}$ which are typical characteristics of few-layer reduced graphene oxide and CNT materials.[137, 139, 140] However, two patterns display different features. The pattern of RGO suggests that even though GO was heat treated less than one minute at 1000 $^{o}$C, it was well reduced and exfoliated to graphene as observed by the broad peak and relatively low intensity of the peak. On the contrary, the hybrid NCNT/RGO composite possesses relatively higher angle and intensity compared to RGO. The pattern is attributed to the multi-walled nature of the NCNT.[139] The number and d-spacing of the graphene layers in NCNT is larger and shorter than those of RGO, respectively, resulting in a sharper peak at a slightly higher angle. The inset of **Figure 6.2(a)** presents the XRD pattern with a relatively sharp peak at ~ 11.5$^{o}$ of GO prepared from natural graphite by the modified Hummer's method to compare with the pattern of graphene-based materials. It supports RGO reduction from GO as the right-shift in the diffraction angle indicates decrease in the d-spacing. The elemental composition of the hybrid NCNT/RGO composite is examined by X-ray photoelectron spectroscopy (XPS) characterization. **Figure 6.2(b)** introduces the full spectrum of the samples in XPS. There are three major peaks which correspond to carbon (C) 1s, nitrogen (N) 1s and oxygen (O) 1s and the diminutive trace of iron (Fe) 2p from the ferrocene catalyst. The peak at the 284.1 eV represents C 1s indicating a majority of carbon is in the conjugated graphitic lattice. The peak corresponding to N 1s at 397.1 eV reveals that nitrogen is successfully doped into the CNT matrix. The peak intensity of O 1s at 532.1 eV have increased during synthesis of NCNT, compared to that of RGO due to the possible formation of pyridinic $N^{+}$-$O^{-}$ during the

synthesis[90] as well as adsorbed oxygen on carbon near the doped nitrogen species in the NCNT due to its affinity to oxygen.[137] In addition, the spectrum of NCNT/RGO exhibits the total content ratio of the carbon, oxygen and nitrogen to be 91.0, 4.6, and 3.9%, respectively. It is expected that the nitrogen species in NCNT render the electrochemical catalytic active sites for ORR since doped nitrogen can produce defects sites related to high activity for oxygen.

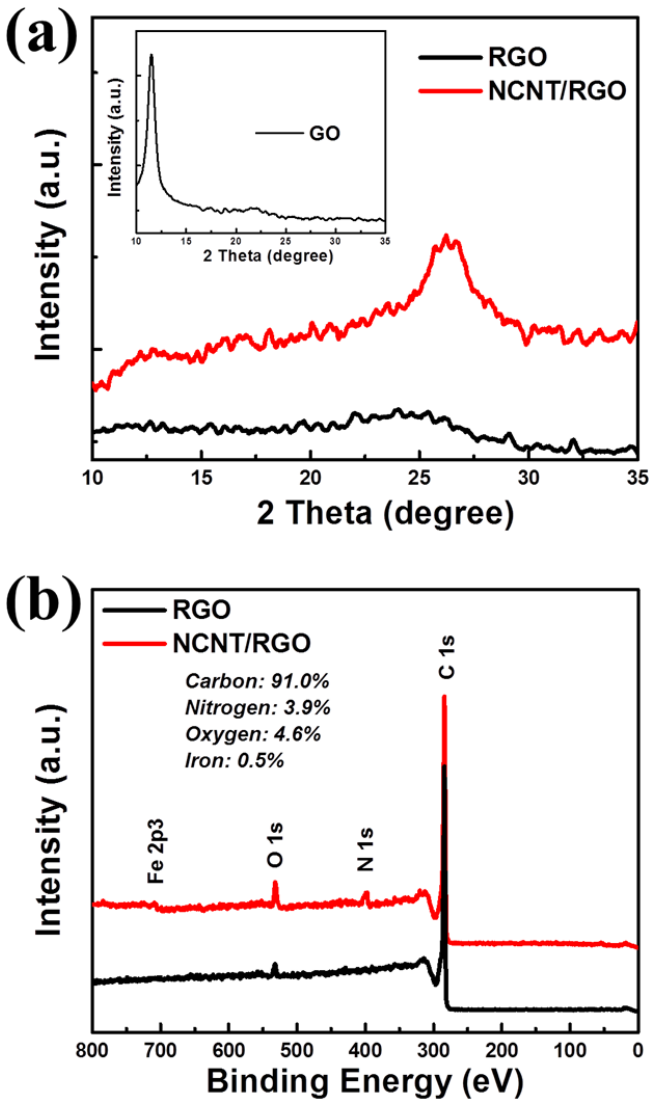


**Figure 6.2** XRD patterns of (a) RGO and NCNT/RGO (inset: graphite oxide (GO)), and (b) full XPS spectra of RGO and NCNT/RGO.

**Figure 6.3(a) and (b)** demonstrate SEM images of the RGO and NCNT/RGO composite, respectively. The SEM image of RGO shows a thin sheet morphology, indicative of the facile synthesis method by thermal treatment successfully reducing graphite oxide to graphene sheets.[38] As shown in Figure 2b, NCNT/RGO composite has resulted in a good dispersion of NCNT on RGO. NCNTs are observed to be present mostly on the graphene surface indicating that they are directly grown on the graphene. Moreover, **Figure 6.3(b)** shows NCNTs contact several graphene sheets so that it is expected to improve conductivity of the electrode. The TEM image of RGO in **Figure 6.3(c)** clearly displays thin and wrinkled morphology of graphene as reported in other literatures.[38, 141] The TEM image shown in **Figure 6.3(d)** supports the SEM analysis of NCNT/RGO composite as NCNTs flourished on the graphene sheet, suggesting the porous structure can be formed between the graphene sheets. NCNTs seem to be stemming out of the graphene sheet **(Figure 6.3(d) inset)**. It is noted that the black dots in the image are the residual iron-based materials from the ferrocene catalyst. Even though the composite have been washed with 0.5 M $H_2SO_4$, based on the procedure of a previous report,[90] the iron particulates still remained in the composite. It is possible that graphitic network have hindered these particles from leaching out, but the amount is negligible as detected by XPS and does not affect the catalytic activities.[136] The inset in the **Figure 6.3(d)** looks as NCNTs take root on the surface of RGO. The TEM and SEM analysis have confirmed the expected morphology of the NCNT/RGO composites in this study.

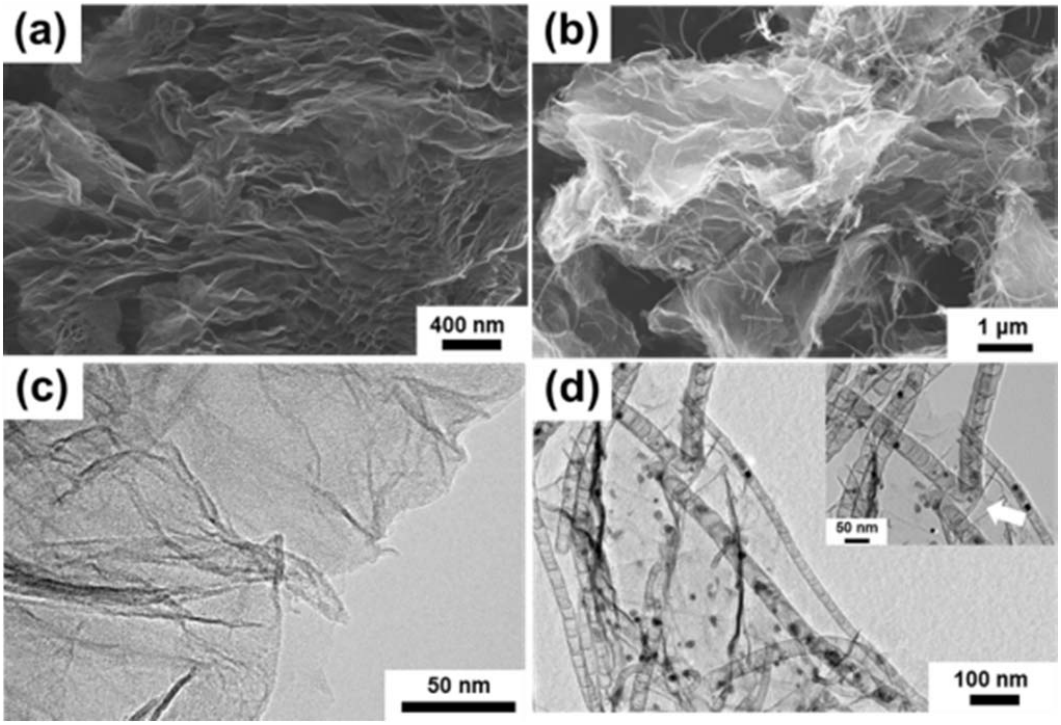


**Figure 6.3** SEM images of (a) RGO and (b) NCNT/RGO, TEM images of (c) RGO and (d) NCNT/RGO (inset: magnified image).

To investigate the surface area and pore size distributions (PSD), Brunauer-Emmett-Teller (BET) and Barrett–Joyner–Halenda (BJH) methods, respectively, have been carried out. **Figure 6.4(a)** exhibits nitrogen adsorption-desorption isotherms of RGO and NCNT/RGO composite at 77K, indicating that the hysteresis loops correspond to previous CNT and graphene works.[38, 142] The surface areas of RGO and NCNT/RGO present 528.4 $m^2 g^{-1}$ and 175.3 $m^2 g^{-1}$, respectively. The large surface area of RGO is another supporting evidence of successful thermal reduction of GO by the thermal annealing process. On the other hand, the composite of NCNT/RGO shows smaller surface area than that of RGO itself, which is likely attributed to NCNT because generally CNT yields smaller surface areas than that of graphene sheets.[38, 142]

However, the PSD of NCNT/RGO is shifted to a larger size, compared to that of RGO, as shown in **Figure 6.4(b)**. This is strong evidence that bolsters our earlier conjecture that the NCNT grown on the surface of graphene sheets help to prevent the sheets from restacking and providing spaces between graphene sheets. It is believed that the suggested structure can enhance utilization of the electrolyte in an electrochemical cell through enlarged spaces between the sheets.

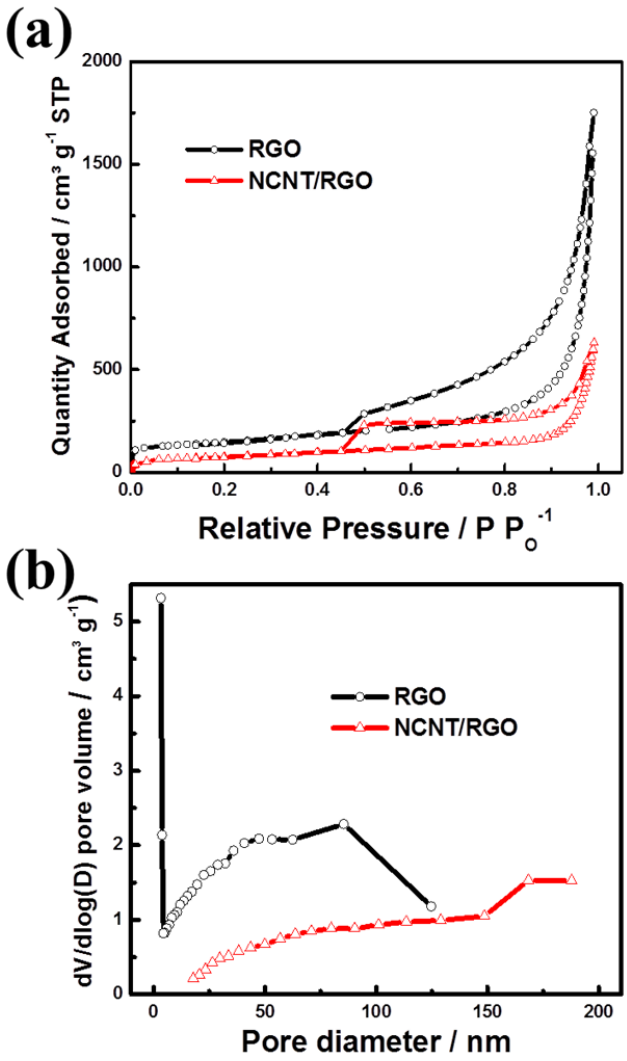


**Figure 6.4** (a) $N_2$ adsorption–desorption isotherms and (b) pore size distribution of RGO and NCNT/RGO.

As shown in **Figure 6.5**, the ORR capabilities of RGO and NCNT/RGO composites are examined by cyclic voltammetry (CV) in nitrogen ($N_2$) and oxygen ($O_2$) atmosphere. For both materials, there are no detectable peak currents observed in $N_2$ atmosphere; however, the significant current peaks have appeared in $O_2$ atmosphere, which indicate that the materials are catalytically ORR active. In addition, higher current density and more positive potential observed for the composite indicates that NCNT/RGO is more catalytically active. For further electrochemical analysis of ORR catalytic activity, rotating disk electrode (RDE) voltammetry with various electrode rotating speeds have been conducted. **Figure 6.6** presents ORR activities of NCNT/RGO, RGO and NCNT, which was prepared in the same reaction batch of NCNT/RGO, via RDE measurements with a rotation speed of 900 rpm at a scan rate of 10 mV $s^{-1}$. All ORR current densities in this study are normalized by surface area of the disk electrode and background-corrected by current densities obtained in $N_2$-saturated 0.1M KOH solution. Although ORR capabilities of RGO itself have been demonstrated, when RGO is combined with NCNT, the activity is significantly enhanced in terms of all electrochemical indicators such as the onset potential, half-wave potential and limiting current density. The performance of the composite presents 123 mV and 152 mV higher onset and half-wave potentials, respectively. In addition, it shows almost twice higher limiting current density at 0.5 V. It is believed that NCNT mainly contributes the improved activity since heteroatom doping in the graphitic layer is known to be the ORR catalytic active sites.[77-79, 143] It also suggests that nitrogen species in the CNT can mainly engender the catalytic activity of the composite. Moreover, the NCNT/RGO composite illustrates 48 mV and 60 mV improvements in terms of onset and half-wave potential, respectively, in comparison to those of NCNT. This is most probably due to the graphene sheets

contributing in improving the activity facilitated by the nanotubes bridging the sheets to create electron pathways, generating useful pores, and preventing restacking of graphene sheets.

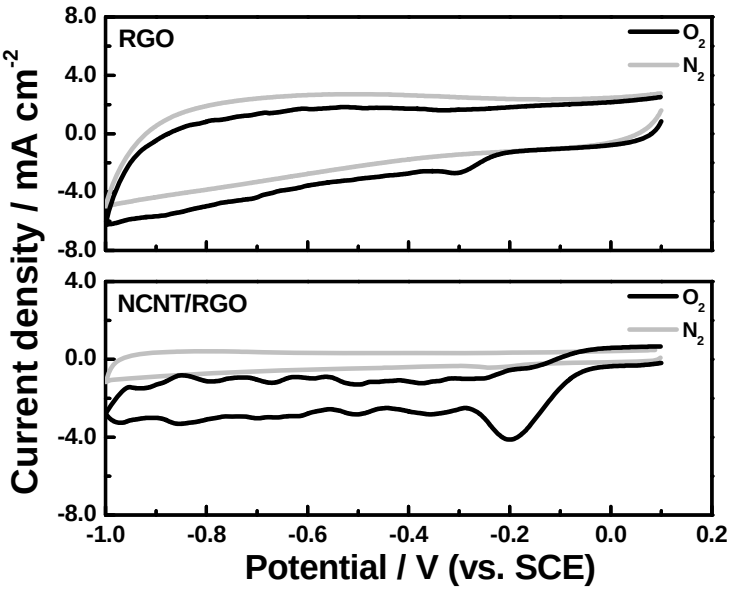


**Figure 6.5** Cyclic voltammograms at scan rate of 50 mV $sec^{-1}$ of RGO and NCNT/RGO in $N_2$ and $O_2$ saturated 0.1 M KOH.

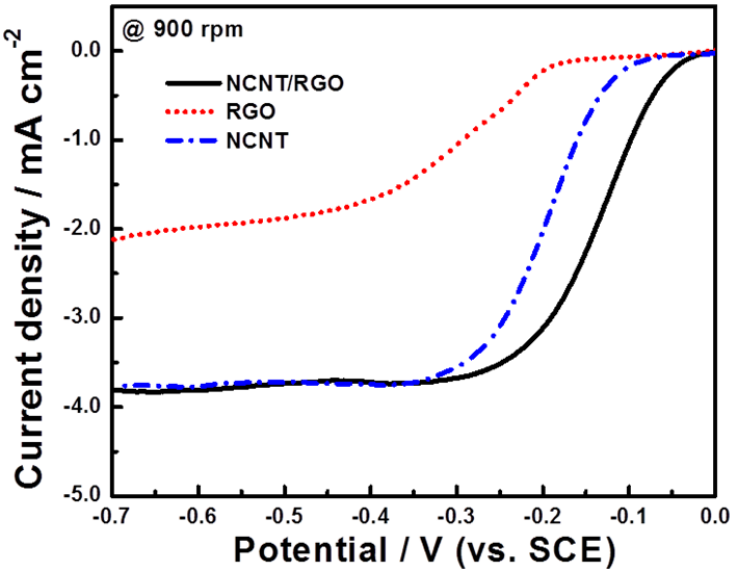


**Figure 6.6** ORR polarization curves of RGO, NCNT and NCNT/RGO at rotation speed of 900 rpm and 10 mV $s^{-1}$ scan rate.

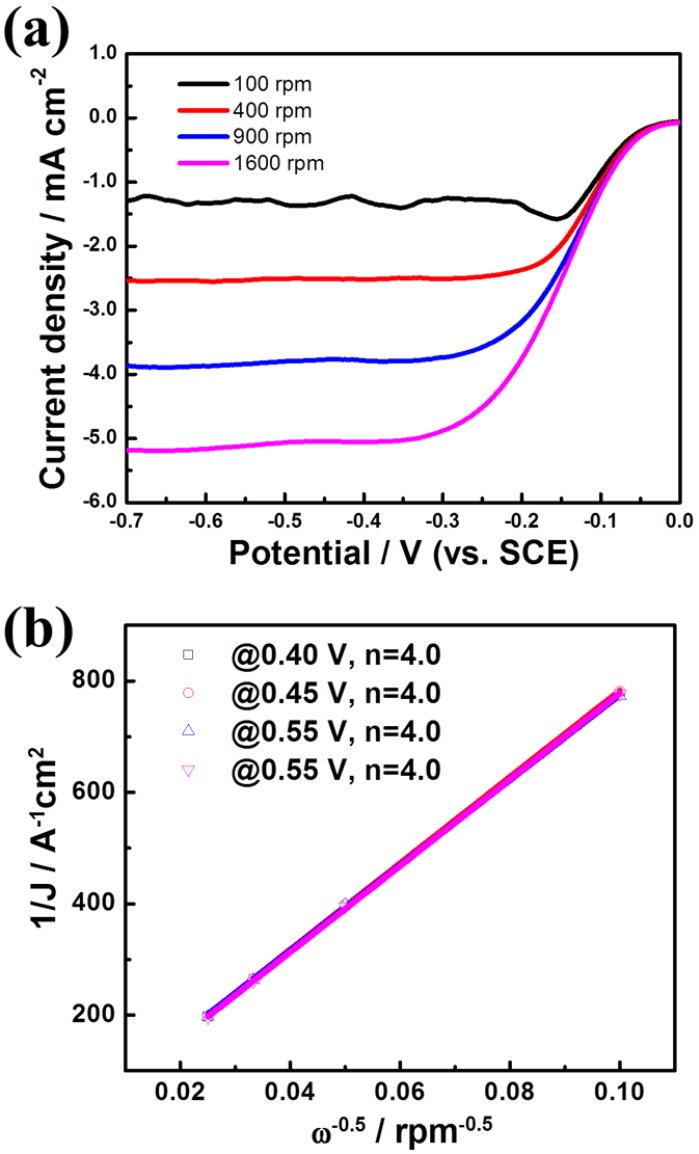


**Figure 6.7** (a) ORR polarization curves of NCNT/RGO at various rotation speeds and 10 mV $s^{-1}$ scan rate and (b) Koutecký-Levich plot at potentials -0.40, -0.45, -0.50 and -0.55 V (vs. SCE).

Based on the RDE measurements of NCNT/RGO at various rotation speeds in **Figure 6.7(a)**, the degree of the ORR activity can be verified via the Koutechý-Levich (K-L) equation. By linear fitting the Koutecky-Levich plots of $i^{-1}$ vs. $\omega^{-0.5}$, the electron number (n) involved in the ORR can be determined, as shown in **Figure 6.7(b)**. The number of electrons is calculated at four different potentials of -0.40, -0.45, -0.50 and -0.55 V to be n=4.0. This is ascribed to the ORR occurring via a four-electron reduction pathway which is known to $O_2 + 2H_2O + 4e^- \rightarrow 4OH^-$, indicating a rapid ORR reaction kinetics. To further examine the ORR activity, the RDE measurement of NCNT/RGO is compared to those of state-of-the-art commercial 20% Pt/C. As shown in **Figure 6.8**, the TRGO/NCNT composite exhibits comparable ORR performance to that of a commercial 20% Pt/C catalyst suggesting the composites developed in this study possesses an excellent ORR catalytic activity. This result could also be highlighted in comparison with the performances from previous reports related to the Pt-based alloy catalysts in alkaline media.[144, 145]

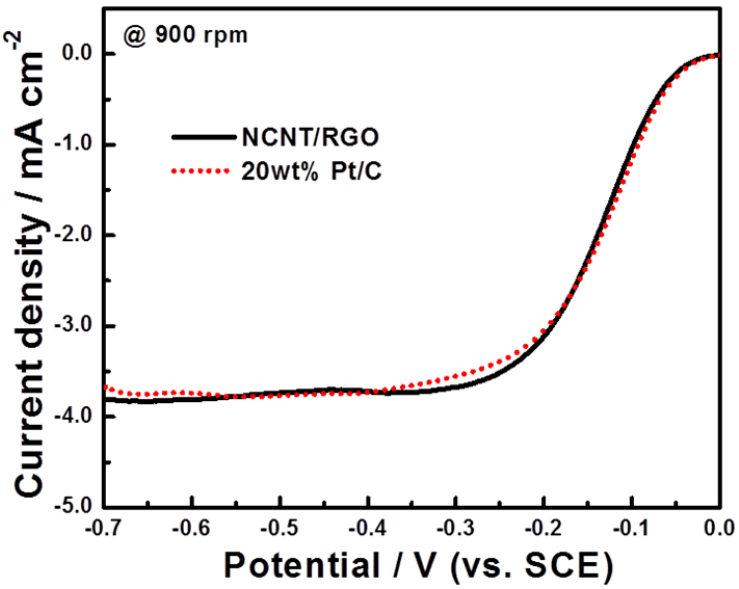


**Figure 6.8** 20 wt% Pt/C with NCNT/RGO at a rotation speed of 900 rpm and 10 mV $s^{-1}$ scan rate.

In addition to the ORR performance, oxygen evolution reaction (OER) capabilities and electrochemical durability of the composite have been tested to evaluate the rechargeability of metal-air batteries. OER activity can be evaluated by the current density at 1.0 V (vs. SCE) as presented in **Figure 6.9(a), (b) and (c)**. Among the NCNT/RGO, NCNT and Pt/C catalysts, the initial OER current density (27.8 mA $cm^{-2}$ at 1.0V) of NCNT/RGO demonstrates outstanding OER activity with 6.5% and 85% higher current density, compared to NCNT and Pt/C, respectively. This value in combination with the ORR result indicates that the NCNT/RGO is an excellent bi-functional OER and ORR catalyst, compare to other metal oxide-based catalysts.[63, 146] In addition to ORR and OER activities, electrochemical durability of the catalysts in the operating voltage range is also a significant parameter especially in evaluating battery cycleability. To examine the durability of the catalysts, a full range CV between -1.0 V and 1.0 V (vs. SCE) in $N_2$-saturated 0.1M KOH solution have been conducted and the summary of the initial and after 200 cycles OER current densities of NCNT/RGO, NCNT and Pt/C catalysts is shown in **Figure 6.9(d)**. The difference of the current densities represents the durability of the catalysts so that the smallest change in current of NCNT/RGO before and after cycle is a direct evidence of its excellent durability. Consequently, NCNT/RGO presents 2.8 and 7.6 times higher OER current density than those of NCNT and Pt/C, respectively, after 200 CV cycles. According to the literatures, Pt/C can be degraded due to platinum agglomeration and dissolution, formation of platinum oxide, or separation from the carbon support during battery operation. NCNT is known to be unstable for extended cycling, suffering from corrosion in the elevated potential.[147] However, the direct conductive network formed by NCNT bridges on RGO cannot only facilitate OER and possibly improve durability of the composite, but also the unique structure can provide outstanding reaction resistance.

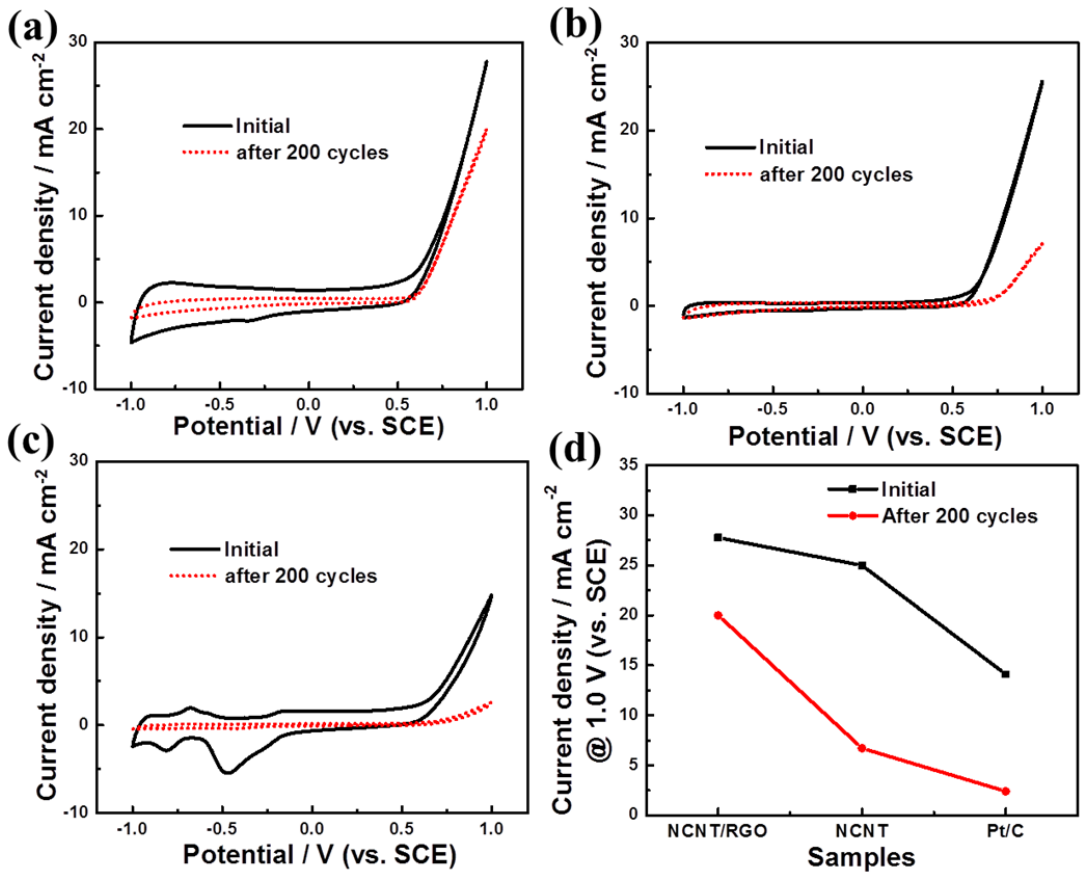


**Figure 6.9** Cyclic voltammograms at scan rate of 50 mV $sec^{-1}$ in $N_2$-saturated 0.1 M KOH solution of (a) NCNT/RGO, (b) NCNT, and (c) 20 wt% Pt/C for initial and after 200 cycles OER performances. (d) Comparison of the OER current density at 1.0 V (vs. SCE) of NCNT/RGO, NCNT and 20 wt.% Pt/C.

Lastly, RDE measurements at 900 rpm have been carried out to evaluate the retention of ORR activity after the full range CV cycling. **Figure 6.10** demonstrates that Pt/C and NCNT catalysts present significant degradation of ORR performance attributed to the change of the catalytic surface, whereas the NCNT/RGO composite outperforms the catalytic activity of Pt/C with twice higher limiting current density with 43 mV greater half-wave potential, confirming a long term catalytic effect of the proposed composite in this study for metal-air battery applications.

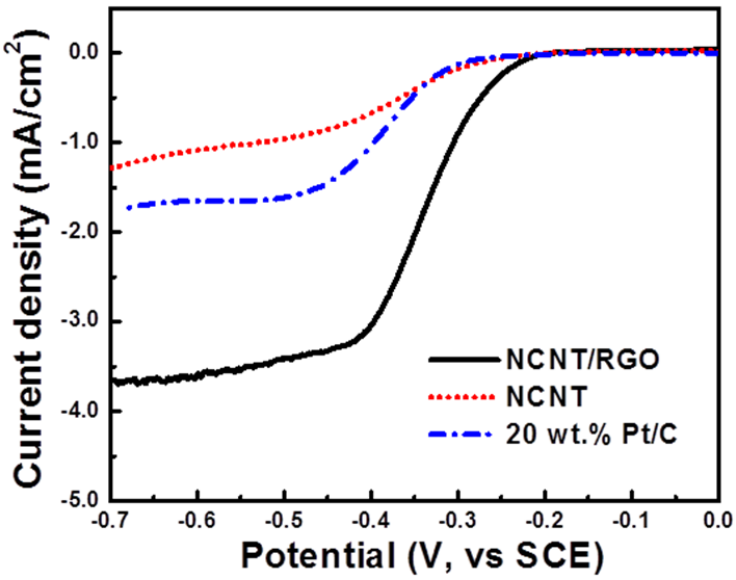


**Figure 6.10** ORR polarization curves of NCNT/RGO, NCNT and 20 wt.% Pt/C at a rotation speed of 900 rpm and 10 mV $s^{-1}$ scan rate after 200 full range CV cycles.

## 6.4 Summary

In this chapter, EDA-based NCNT was directly grown on RGO by the injection CVD method. RGO in this study was prepared via the facile thermal annealing method as introduced

in Chapter 4 but without using $NH_3$ gas. The novel morphology of the NCNT-bridged RGO composite was characterized by SEM and TEM, confirming NCNT synthesized on the surface of RGO. In addition, XPS results reveal chemical elements in NCNT/RGO, confirming nitrogen-doping of CNT during the CVD synthesis. The NCNT/RGO composite catalyst in half-cell testing not only showed excellent ORR activity illustrating a four electron reduction pathway, but also demonstrated certain degree of OER activity with good durability. Moreover, this study introduced that one dimensional nitrogen-containing carbon material is responsible for the ORR activity and the combination of two promising graphitic carbons with novel morphologies enhanced catalytic activity toward OER. Based on the results of excellent electrocatalytic activities with stability, it is revealed that the composite catalyst combined with NCNT can create promising catalysts for rechargeable metal-air batteries.

# 7. One-Pot Synthesis of Perovskite Oxide-Based Nitrogen-Doped Carbon Nanotube Composites as Bi-functional Catalysts for Rechargeable Lithium-Air Batteries

## 7.1 Introduction

As introduced in the previous chapters, metal oxides and heteroatom-doped RGO or CNT hybrid catalysts have demonstrated promise as bi-functional catalysts towards both ORR and OER.[6, 63, 65, 129] However, the directly grown CNT-based composite catalysts are more suitable for practical applications and large scale production since RGO is prepared from graphite oxide (GO) that must be produced by highly reactive chemicals and intricate processes. Chen et al. previously proposed the novel strategy to prepare directly grown-NCNTs on a metal oxide bi-functional catalyst using a perovskite oxide of $LaNiO_3$ as a core material.[63] The catalyst exhibited impressive performance in a rechargeable Zn-air battery, although its synthesis was still complex and the catalytic activities demonstrated limited synergy between the metal oxide and NCNT. In this chapter, a facile and one-pot synthesis of perovskite oxide of $La_{0.5}Sr_{0.5}Co_{0.8}Fe_{0.2}O_3$ nanoparticles (LSCF-NP) and NCNT composite (op-LN) is introduced as highly active and durable bi-functionally active catalyst. While solution-based LSCF-NP precursors are calcined at 700 $^{o}$C, NCNT is then directly synthesized on the surface of LSCF-NP by injection chemical vapor deposition (CVD), forming an NCNT-wrapped metal oxide composite by a fast and simple method. The composite demonstrates enhanced ORR and OER catalytic activities in alkaline medium, verifying their excellent combination by attaining synergistic performances. The unique elemental composition and morphology of the core metal

oxide are attributed to the enhancement of the catalytic activities, which outperforms those previously proposed.[63] In addition to the excellent activities, this work also emphasizes that this novel method offers the practical benefit of a facile process to prepare the bi-functional catalysts. Lastly, the developed catalyst has been tested using a practical rechargeable Li-air battery to examine its performance in a practical application. The performance of the catalyst in the battery consistently demonstrates outstanding results, as with the half-cell investigation in alkaline medium. These promising results are highly convincing for the use of this composite as a bi-functional catalyst for rechargeable Li-air batteries.

## 7.2 Experimental

One-pot synthesis of $La_{0.5}Sr_{0.5}Co_{0.8}Fe_{0.2}$ nanoparticle (LSCF-NP)-based NCNT composite (op-LN) was developed by combining a simple calcination method and an injection chemical vapor deposition (CVD) method, as described in **Figure 7.1**. First, the precursor solution for LSCF-NP was prepared by completely dissolving $La(NO_3)_3 \cdot 6H_2O$, $Sr(NO_3)_2$, $Co(NO_3)_2 \cdot 6H_2O$ and $Fe(NO_3)_3 \cdot 9H_2O$ in $H_2O$ and $C_2H_5OH$ at a 1:1 mass ratio along with 16.7 wt.% PVP. The solution (1.5 mL) was spread onto the interior of a small quartz tube and the tube was put into a bigger and longer quartz tube which was then placed in the center of a horizontal tube furnace. The calcination was conducted at 700 $^oC$ after ramping the temperature at a rate of 1 $^oC\ min^{-1}$. After 3 hr calcination, Ar gas was purged into the long tube while 2.5 wt.% ferrocene ($C_{10}H_{10}Fe$)-dissolved ethylenediamine ($C_2H_8N_2$) solution was loaded into a syringe for NCNT synthesis. The solution (2.0 mL) was injected at 0.05 mL $min^{-1}$ under Ar protection at 100 sccm.

After the injection, the furnace was cooled down to room temperature, and the final product op-LN was collected. To obtain only LSCF-NP, the injection steps were omitted. After 3 hr at 700 $^{o}$C, the furnace was cooled down to room temperature and LSCF-NP powder was collected and ground.

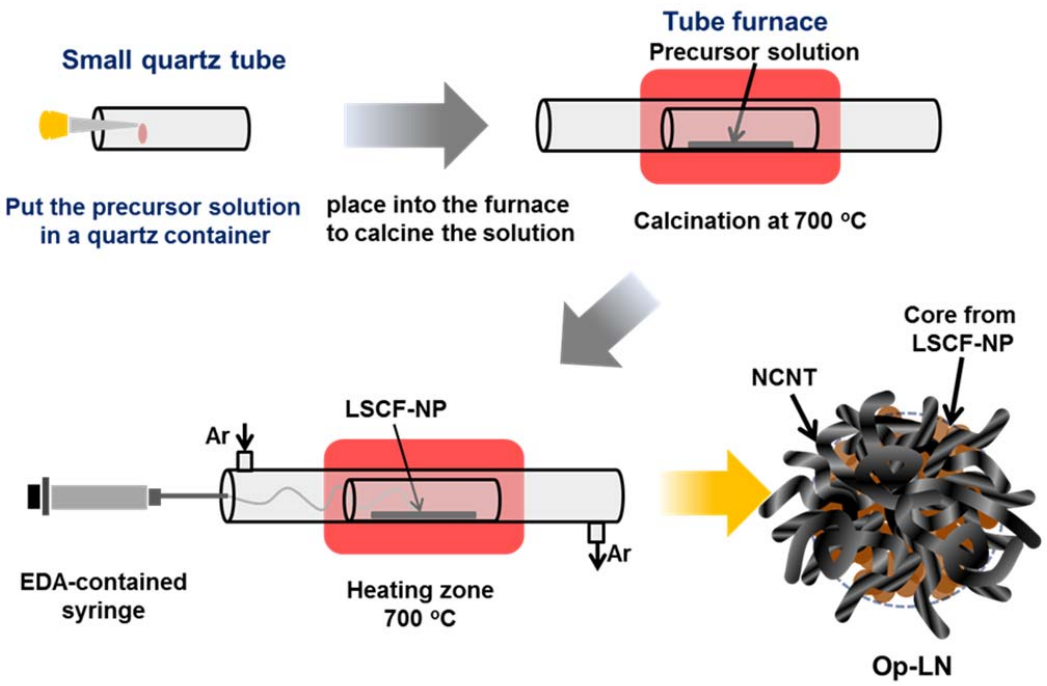


**Figure 7.1** Schematic diagrams of the synthesis of op-LN catalyst.

## 7.3 Results and Discussion

As described in **Figure 7.1**, the LSCF-NP-based NCNT composite (op-LN) catalyst was prepared through a simple calcination of the precursor solution for LSCF-NP, followed by injection CVD at the same temperature for NCNT. This approach has the advantage of simplifying the preparation steps and time to prepare the metal oxide and CNT hybrid materials. The progress of the reaction was stopped prior to the beginning the injection CVD to confirm the formation of perovskite oxide of LSCF-NP. It was found that the perovskite oxide LSCF-NP could be prepared by simple calcination using PVP and nitrate-based metal precursor dissolved in water and ethanol solution. The morphology and crystallite phase of the product, after calcination of the PVP-containing precursor solution at 700 $^{o}$C for 3hr, were examined by SEM, TEM and XRD, as shown in **Figure 7.2**. The SEM image (**Figure 7.2(a)**) shows nano-sized particles clustered together but not as oviously as in the TEM image (**Figure 7.2(b)**), which clearly reveal the nano-sized LSCF particles. TEM confirms the agglomeration of particles as well as the pore structures. The magnified image in **Figure 7.2(c)** shows the pores within the particles. It is assumed that the pores were generated by PVP in the precursor solution during the high temperature calcination. The XRD pattern in **Figure 7.2(d)** reveals that a pure perovskite phase of LSCF-NP was obtained, consistent with the pattern reported in the literature.[19, 125] The crystal phase in the XRD pattern is also supported by Selected Area Electron Diffraction (SAED) pattern **(Figure 7.2(c) inset)** obtained from the TEM image. Based on the main peak of (110) plane in the XRD pattern, a crystallite size is calculated to be 11.1 nm using the Scherrer equation:[148]

$$\mathbf{D} = \frac{\mathbf{0.9\lambda}}{\boldsymbol{B \times cos\theta}} \qquad (7.1)$$

where D is the crystallite size, λ is the wavelength of the X-ray source, B is the peak width at the half-maximum intensity, and θ is the diffraction angle. Furthermore, the elemental composition determined by EDS analysis from TEM yields each chemical element shown in **Figure 7.3**. The EDS element images confirm that a homogeneous dispersion off the components throughout the structure is obtained.

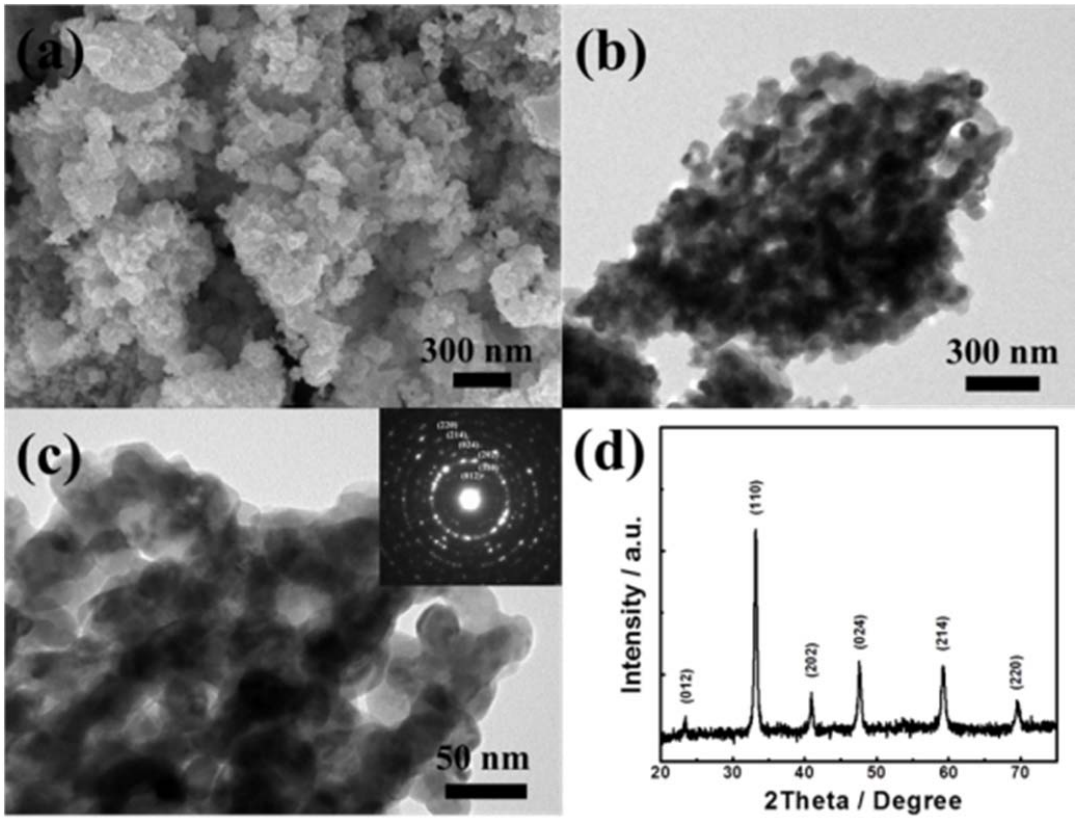


**Figure 7.2** (a) SEM image, (b) TEM image and (c) magnified TEM image of LSCF-NP (inset: SAED pattern). (d) XRD pattern of LSCF-NP.

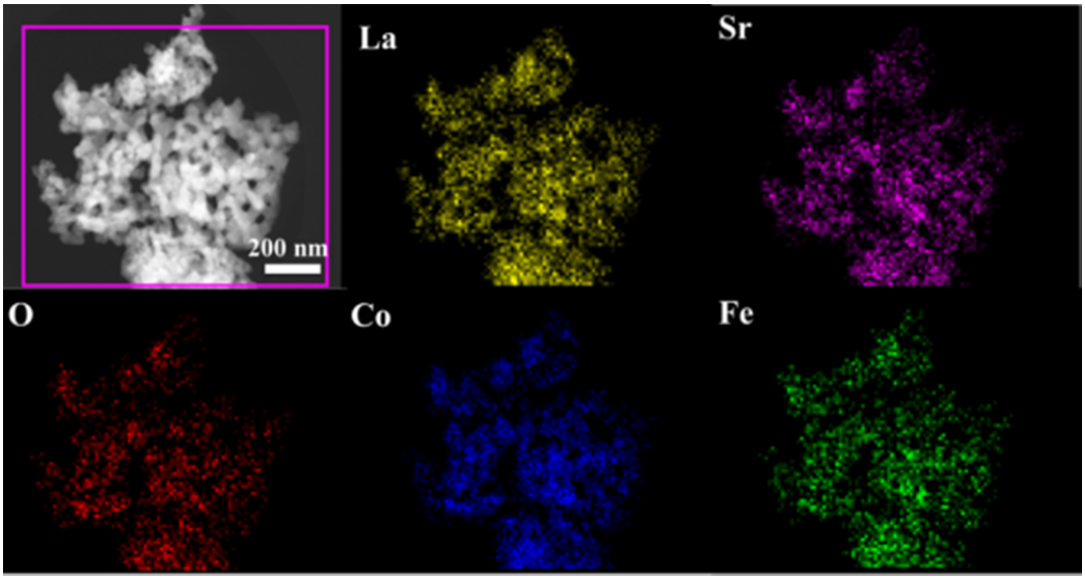


**Figure 7.3** Elemental mapping by EDS of LSCF-NP obtained by TEM analysis.

The electrocatalytic activities of LSCF-NP for ORR ($O_2 + 2H_2O + 4e^- \rightarrow 4OH^-$) and OER ($4OH^- \rightarrow O_2 + 2H_2O + 4e^-$) were evaluated in 0.1M KOH electrolyte with a rotating disk electrode (RDE) setup by electrochemical methods. Prior to the actual ORR measurements, linear sweep voltammetry (LSV) in the potential range from 0.1 V to - 1.0 V (vs. SCE) in $N_2$-saturated 0.1 M KOH electrolyte was conducted to obtain the background correct the ORR current. All current densities presented in this work are normalized by the surface area of the glassy carbon RDE. **Figure 7.4(a)** shows the results of cathodic LSV of LSCF-NP/Vulcan carbon (VC) and VC alone at 900 rpm rotation speed in $O_2$-saturated 0.1M KOH at 10 mV $s^{-1}$ scan rate. LSCF-NP exhibits superior ORR performance in terms of half-wave potential and limiting current density at 0.6 V, showing improvement by 30 mV and 1.8 mA $cm^{-2}$, respectively, compared to that achieved using Vulcan carbon alone. In addition to the ORR activity, **Figure 7.4(b)** shows the OER activity of LSCF-NP/VC at the rotation speed of 900 rpm in $O_2$-saturated 0.1 M KOH obtained by sweeping the potential between 0 V to 1.0 V at a rate of 10 mV $s^{-1}$. A

significant improvement in terms of the maximum current by 17..5 mA $cm^{-2}$ as well as a reduction in the potential at 1.0 mA $cm^{-2}$ by 60 mV, is obtained relative to that achieved using VC alone. The electrochemical results of these half-cell tests are summarized in **Table 7.1**. Although LSCF-NP alone demonstrates a certain degree of ORR and OER catalytic activity, the electrochemical results indicate that LSCF-NP does not seem to be as sufficiently good bi-functional catalyst toward both ORR and OER since the ORR activity is still much inferior to that of the Pt/C catalyst **(Figure 7.5(a))**. However, it is worth noting that the OER performance distinctively outperforms that of Pt/C catalyst **(Figure 7.5(b))**.

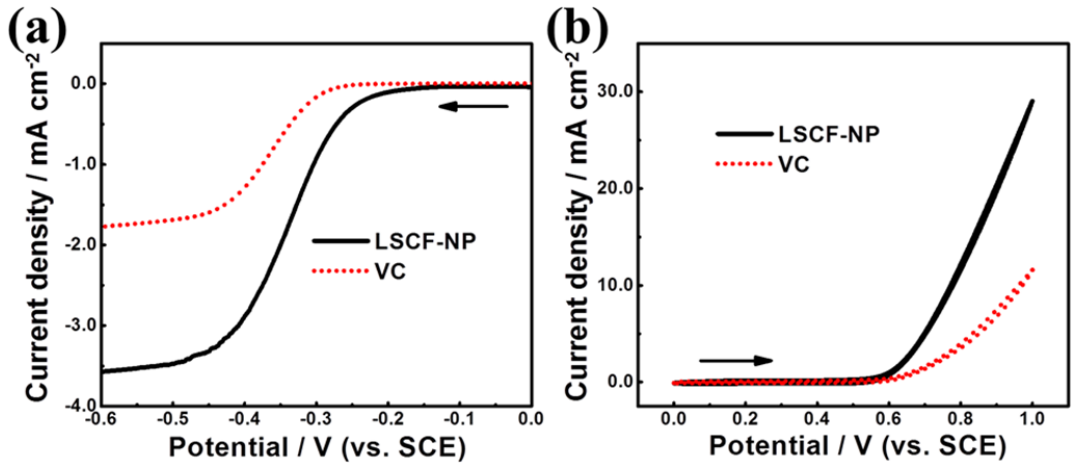


**Figure 7.4** (a) ORR and (b) OER polarization curves of LSCF-NP/VC and VC at rotation speed of 900 rpm and 10 mV $s^{-1}$ scan rate in $O_2$-saturated 0.1 M KOH solution..

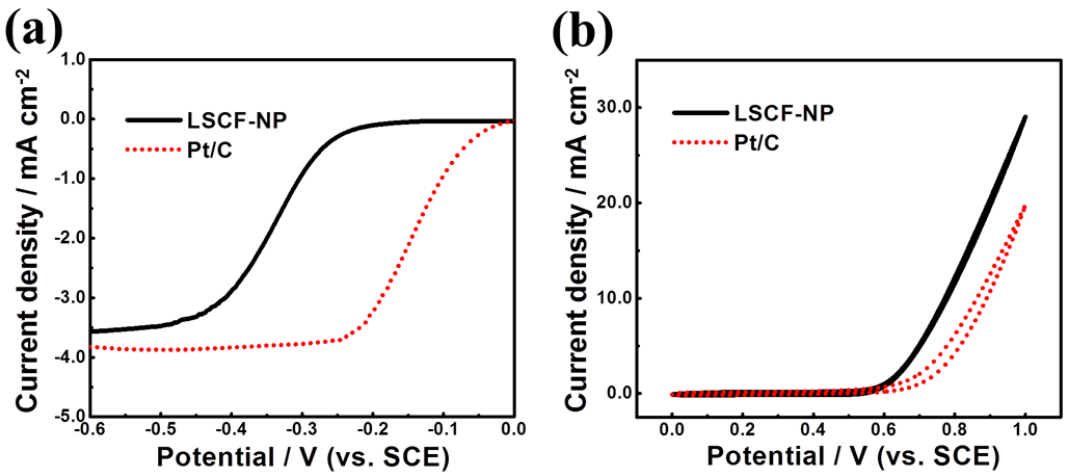


**Figure 7.5** (a) ORR and (b) OER polarization curves of LSCF-NP/VC and Pt/C at rotation speed of 900 rpm and 10 mV $s^{-1}$ scan rates in $O_2$-saturated 0.1 M KOH solution, respectively.

**Table 7.1** Summary of the half-cell test obtained for results LSCF-NP/VC and VC.

| | ORR | | OER | |
|---|---|---|---|---|
| | **Half-wave potential / V** | **Limiting current density / mA $cm^{-2}$** | **Potential at 1.0 mA $cm^{-2}$ / V** | **Max. current density / mA $cm^{-2}$** |
| **LSCF-NP/VC** | **-0.34** | **-3.57** | **0.60** | **29.1** |
| **VC** | **-0.37** | **-1.77** | **0.66** | **11.6** |

To produce a composite effective as a bi-functional catalyst, a facile one-pot synthesis method combining a simple calcination method for LSCF-NP and injection CVD method using EDA for NCNT has been utilized, as described in **Figure 7.1**. During the LSCF-NP synthesis, the metal precursor solution for LSCF-NP is spread in a small quartz tube, which is placed into a large quartz tube for the NCNT growth. Once the temperature reached 700 $^{o}$C and was

maintained for 3 hr, the injection CVD proceeded to initiate growth of NCNT on the metal oxide. After the preparation of the composite, NCNTs formed on the metal oxide as a corona structure, improving the ORR performance while maintaining the metal oxide OER activity. The prolific growth and excellent coverage of NCNT around the metal oxide core by NCNTs is observed in SEM images **(Figure 7.6(a) and (b))**. The morphology confirmed by TEM (**Figure 7.6(c))** clearly shows the composite of the core metal oxide that is well surrounded by NCNTs, most likely due to the strong interaction.[63] A magnified TEM image on the NCNT in **Figure 7.6(d)** clearly shows the typical bamboo-like structure of NCNT.[90, 91, 142]

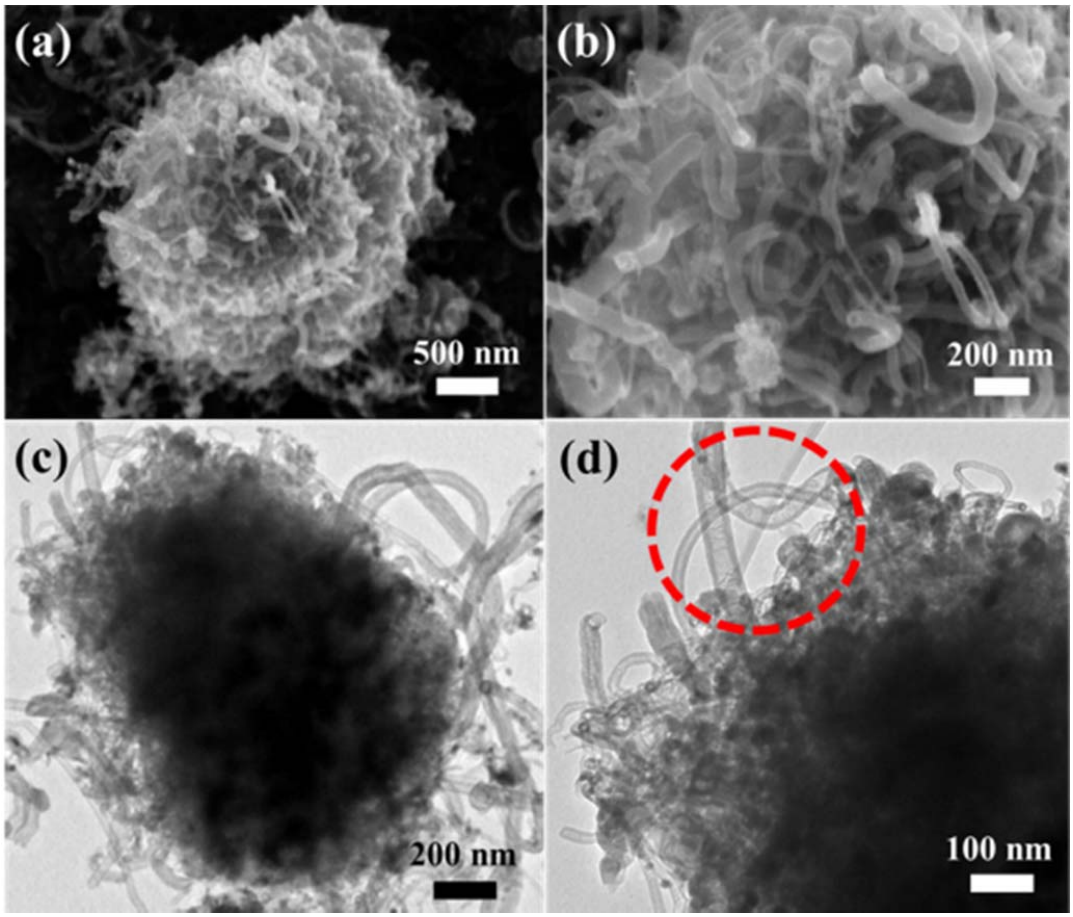


**Figure 7.6** (a) SEM image, (b) magnified SEM image, (c) TEM image and (d) magnified TEM image of op-LN catalyst.

XPS analysis has been utilized to investigate the composition of the composite and to confirm the heterogeneous nitrogen doping and its configurations in NCNT. A full XPS survey scan in **Figure 7.7(a)** shows the main peak of C 1s at 284.5 eV, which corresponds to graphitic carbon.[130] Another strong peak of N1s at ca.400.0 is observed, which confirms the incorporation of nitrogen species in the CNTs and only tiny La3d, Sr3d, Co2p and Fe2p peaks are detected. This corroborates the early microscopic analyses that the metal oxide is well covered by NCNT. The high resolution spectrum of the N 1s peak shown in **Figure 7.7(b)** provides clear evidence of nitrogen atoms in NCNT, which indicates the existence of nitrogen species dominantly in pyridinic form and three other configurations: pyrrolic, quaternary and oxidized pyridinic. These nitrogen configurations in the graphitic layer, which make up the NCNT walls, have been reported to directly contribute to the ORR activity.[62, 80, 91, 126, 149] Additionally, thermal gravimetric analysis (TGA) **(Figure 7.8)** was conducted to investigate the mass ratio of the metal oxide and NCNT showing that the composite consists of 78 % NCNT and 32 % of the metal oxide, supporting the hypothesis that the nano-core particles provide many sites for NCNT to grow.

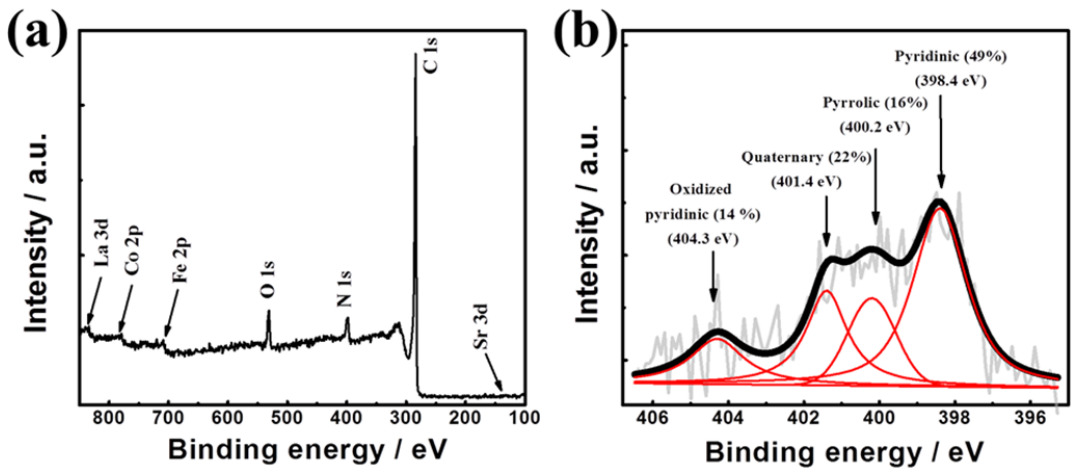


**Figure 7.7** (a) Full XPS spectra of op-LN, and (b) de-convoluted high resolution N1s XPS spectrum of NRGO.

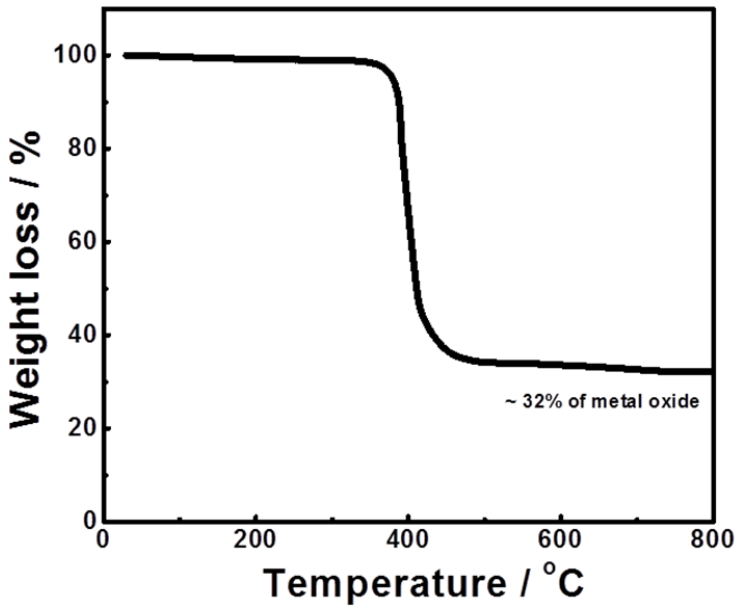


**Figure 7.8** Plot of the thermal behavior from the TGA of op-LN

After chemical and physical characterization of the op-LN composite, its electrochemical catalytic activities for ORR and OER were evaluated to prove the hypothesis of the study using half-cell RDE tests in a 0.1 M KOH solution. The measured reaction currents for ORR have been corrected by subtracting the background current obtained by carrying out the same measurement in $N_2$-saturated 0.1 M KOH solution and the measured currents for ORR and OER are normalized by the surface area of the glassy carbon RDE. **Figure 7.9(a)** shows the LSV data for op-LN, LSCF-NP and NCNT at a rotation speed of 900 rpm in $O_2$-saturated 0.1M KOH for ORR. The op-LN shows significant improvement of the onset and the half-wave potential, and the limiting current density for ORR compared to LSCF-NP. This is attributed to the incorporation of NCNT into LSCF-NP, which plays a significant role in enhancing the ORR catalysis of the composite due to the heterogeneous nitrogen atoms doped in the graphitic layer.[62, 142, 150] In addition, op-LN exhibits superior ORR performance in terms of the half-wave potential relative to NCNT alone, showing improvement by 34 mV. The number of electrons transferred in the ORR is analyzed by K-L plot obtained from RDE measurements at various rotation speeds **(Figure 7.9(b))**. Linear fitting of the K-L plots of $i^{-1}$ vs. $\omega^{-0.5}$ is used to determine the electron number (n) involved in the ORR at a given potential as shown in **Figure 7.9(c)**.[136, 151] The number of electrons is calculated to be n=3.8~3.9 at -0.40 -0.45, -0.50 and 0.55 V (vs. SCE). This result is indicative of the ORR occurring with a swift kinetics via the pseudo four-electron reduction pathway. The catalytic activity of the composite for OER is evaluated by cyclic voltammetry (CV) over the voltage range of 0 to 1.0 V (vs. SCE) in $O_2$-saturated 0.1M KOH solution. While ORR is related to the discharge process in a metal-air battery, OER is related to the charge process and is critical for recharging metal-air batteries. The enhanced catalytic activity of the composite for OER is also observed by the increase in the current compared to

that of LSCF-NP and NCNT as shown in **Figure 7.9(d)**.Op-LN shows an increase in current by 27% and 71% at 1.0 V when compared to LSCF-NP and NCNT, respectively. It is speculated that the significant OER improvement is not only due to the facilitated charge transfer by the conductive pathway provided by NCNT, but also the interaction between the metal core and the NCNT. This interaction may be a key factor for the synergistic effect of op-LN, which needs to be confirmed by further study. The op-LN has also been compared with the state-of-the-art Pt/C catalyst to assess its activities for ORR and OER. **Figure 7.10(a) and (b)** shows that op-LN demonstrate comparable ORR activity curve to that of the commercial Pt/C catalyst, and much superior OER capability, demonstrating its outstanding bi-functional activities. The results of these electrochemical in half-cell tests of op-LN, NCNT and Pt/C are summarized in **Table 7.2**.

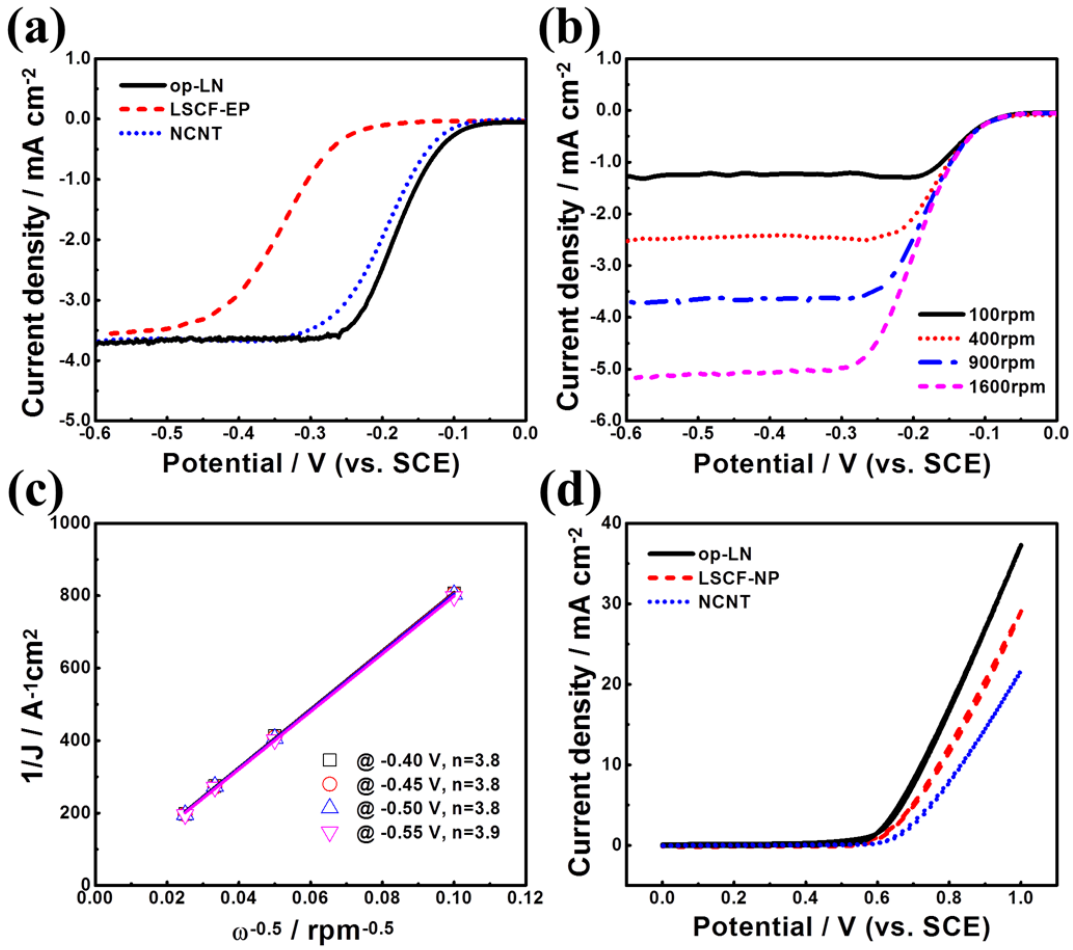


**Figure 7.9** (a) ORR polarization curves of op-LN, LSCF-NP/VC and NCNT at rotation speed of 900 rpm, (b) ORR polarization profiles of op-LN at various rotation speeds, (c) K-L plots at −0.40, −0.45, −0.50 and −055 V (vs. SCE)) and (d) OER polarization curves of op-LN, LSCF-NP/VC and NCNT at rotation speed of 900 rpm and 10 mV $s^{-1}$ scan rate in $O_2$-saturated 0.1 M KOH solution.

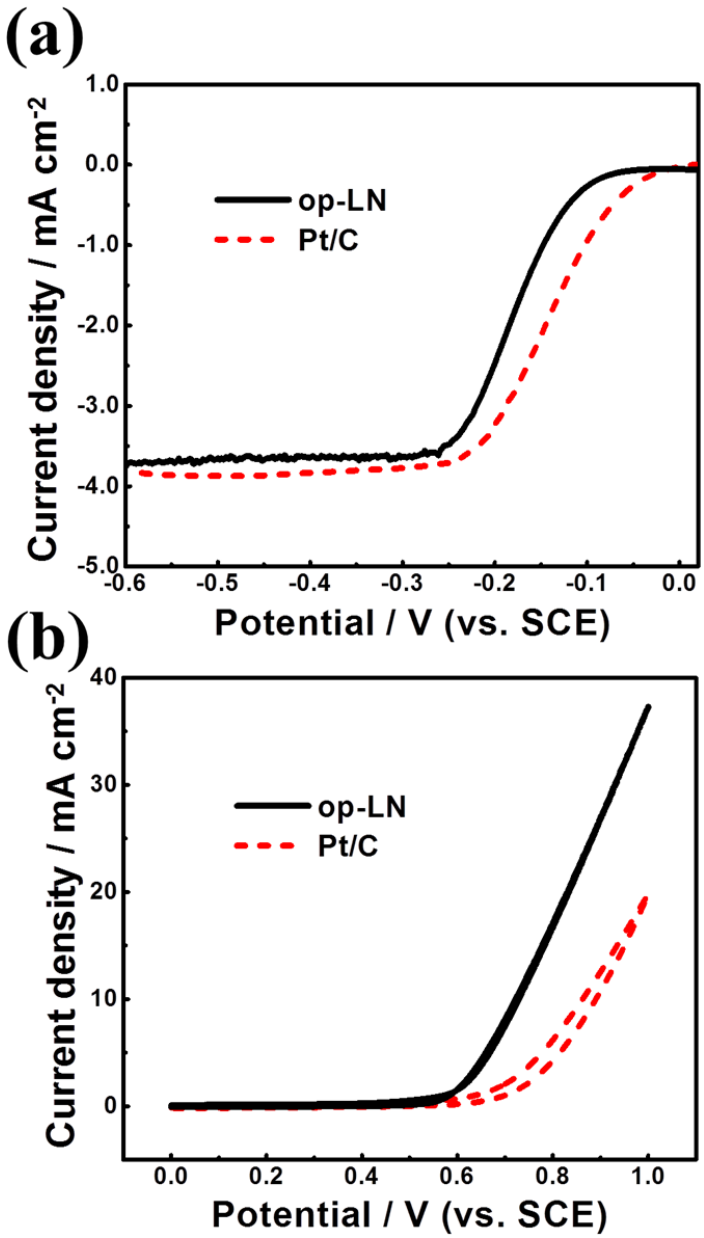


**Figure 7.10** (a) ORR and (b) OER polarization curves of op-LN and Pt/C at rotation speed of 900 rpm and 10 mV $s^{-1}$ scan rates in $O_2$-saturated 0.1 M KOH solution.

**Table 7.2** Summary of the half-cell test results of op-LN, NCNT and Pt/C catalysts.

| | ORR | | OER | |
|---|---|---|---|---|
| | **Half-wave potential / V** | **Limiting current density / mA cm$^{-2}$** | **Potential at 1.0 mA cm$^{-2}$ / V** | **Max. current density / mA cm$^{-2}$** |
| **op-LN** | **-0.16** | **-3.70** | **0.57** | **37.1** |
| **NCNT** | **-0.19** | **-3.68** | **0.65** | **21.7** |
| **Pt/C** | **-0.14** | **-3.82** | **0.64** | **19.8** |

In addition, the long-term durability of the catalyst is demonstrated as a commercially viable material for rechargeable metal-air batteries. **Figures 7.11(a) and (b)** show CVs obtained at a scan rate of 50 mV $s^{-1}$ in the OER potential rage of 0 to 1.0 V in $N_2$-saturatated 0.1 M KOH electrolyte before and after 500 cycles for op-LN and 300 cycles for Pt/C, respectively. This high positive potential range is employed as a severe condition for examining the catalyst durability in a short period of time. Although the reaction current obtained on Pt/C after 300 OER cycles is negligible, op-LN still generates 23.9 mA cm$^{-2}$ of OER current at 1.0 V, reflecting its high durability for OER. The current density of op-LN after 500 cycles is even higher than the initial OER current density of the Pt/C catalyst. Furthermore, retention of the ORR activity after the OER durability test was investigated by RDE measurements at a rotation speed of 900 rpm in $O_2$-satuarted 0.1 M KOH as shown in **Figure 7.11(c)**. The ORR activity of the op-LN also shows less deterioration than that of the Pt/C catalyst. As a result, op-LN surpasses Pt/C with a 120 mV positive shift in the half-wave potential and 0.91 mA cm$^{-2}$ increase in the current density at 0.6 V after the durability testing even though the initial performances of both catalysts have been comparable. This clearly confirms the long term stability of bi-functional activities of op-LN,

most likely due to the strongly coupled metal oxide core and NCNT as well as inter-particle interactions made possible through the NCNT network, resulting in excellent cycle stability.

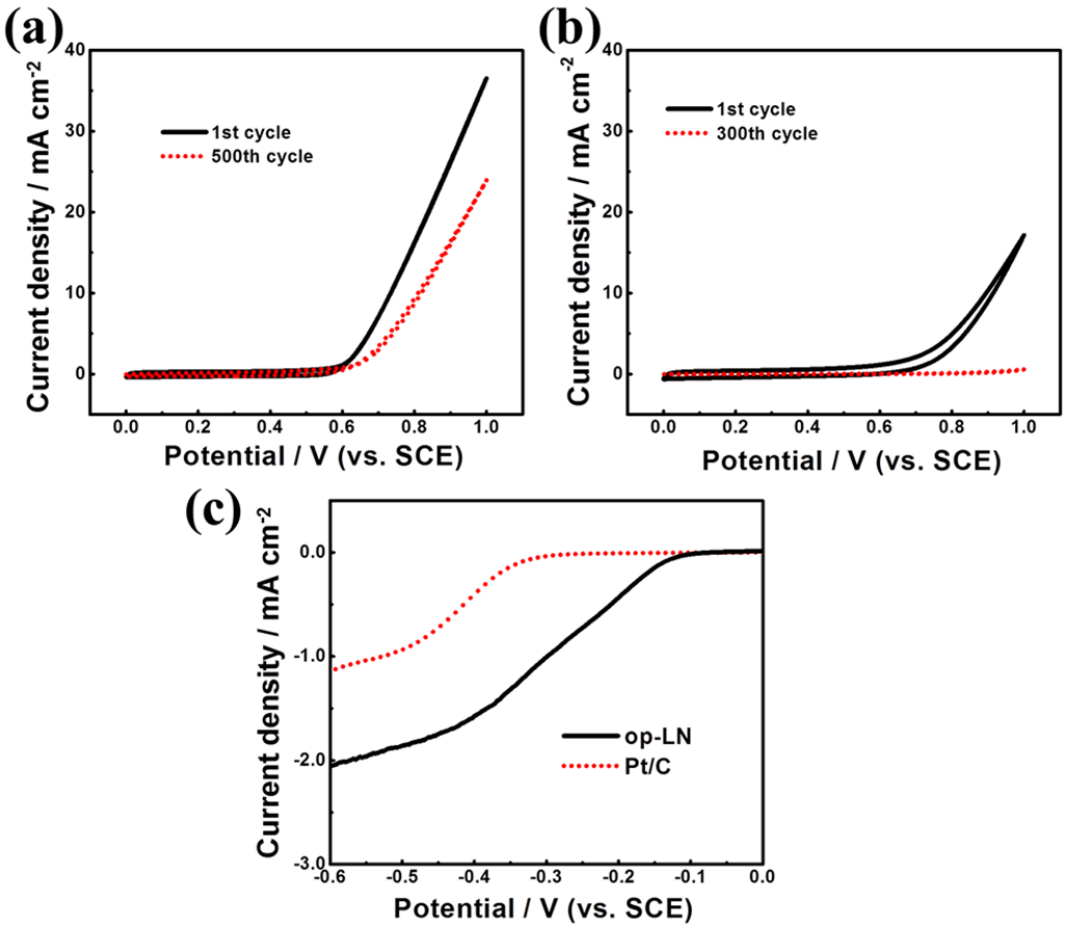


**Figure 7.11** Cyclic voltammograms of initial state and after 500 and 300 cycles of (a) op-LN and (b) Pt/C, respectively, between 0 and 1.0 V (vs. SCE) at a rotation speed of 900 rpm and 50 mV $s^{-1}$ scan rate in $N_2$-saturated 0.1 M KOH. (c) ORR polarization curves of op-LN and Pt/C after 500 cycles and 300 cycles, respectively, at rotation speed of 900 rpm and 10 mV $s^{-1}$ scan rate in $O_2$-saturated 0.1 M KOH.

Li-air battery performance was assessed for op-LN as an air cathode catalyst. An in-house designed rechargeable Li-air battery has made from a Li metal sheet and catalyst-coated gas diffusion layer (GDL) as an anode and cathode, respectively, as described in **Figure 3.7** (Chapter 3). In addition, two different types of electrolytes (carbonate-based non-aqueous solution on the anode side and LiOH-based aqueous solution on the cathode side) were utilized and divided by a LISICON membrane. **Figure 7.12(a)** shows the discharge and charge curves at various current densities obtained using op-LN. The stable profiles at applied current densities of 0.2 mA $cm^{-2}$ to 2 mA $cm^{-2}$ confirm that the developed catalyst in this study works as the bi-functional catalyst in a Li-air battery. At a current density of 0.5 mA $cm^{-2}$, the operating voltage is observed to remain a ~ 2.93 V and 3.86 V vs. $Li/Li^{+}$ for discharge and charge, respectively. Compared with the performance of LSCF-NP and NCNT catalysts in Li-air battery, this composite results in a significant improvement in the bi-functional catalytic activity as shown in **Figure 7.12(b)**. The voltage difference between discharge and charge processes of op-LN is 61 mV and 63 mV less than that obtained with LSCF-NP and NCNT, respectively.

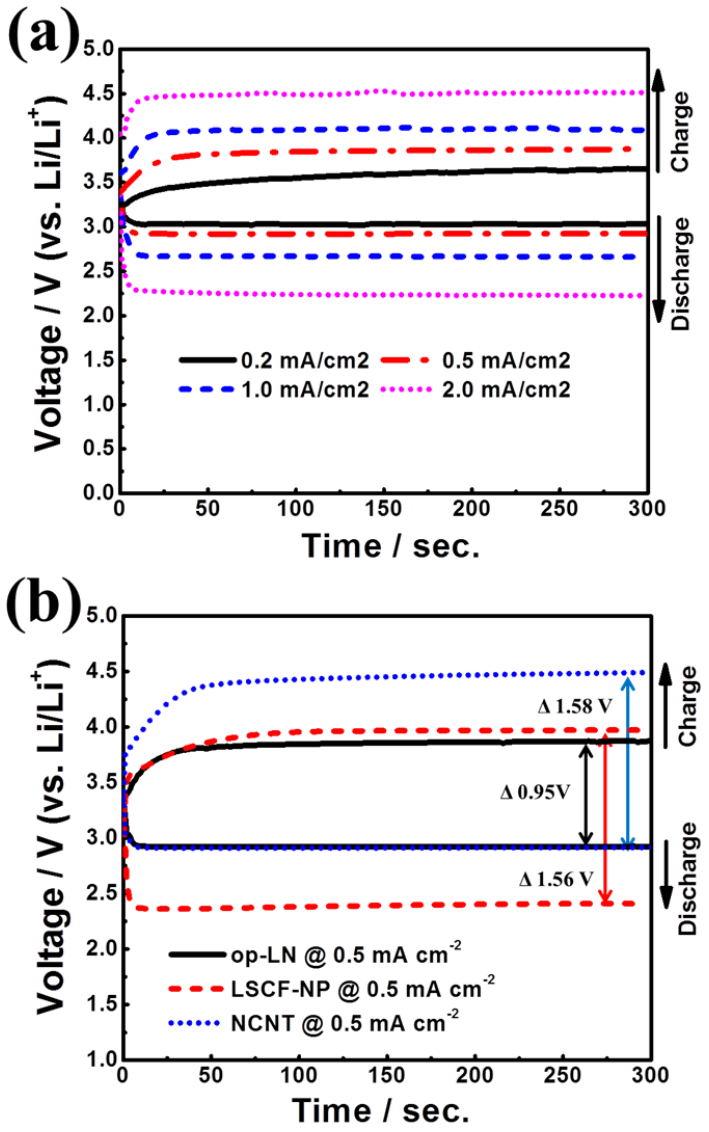


**Figure 7.12** Li-air battery performance using op-LN. (a) Discharge and charge (D/C) polarization curves at various applied current densities, (b) Comparison of D/C polarization curves obtained with op-LN, LSCF-NP and NCNT.

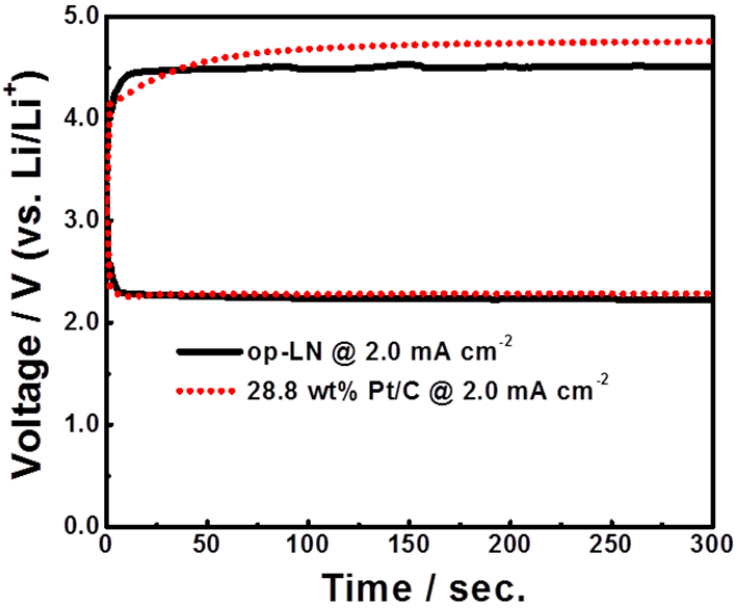


**Figure 7.13** Li-air battery performance. D/C polarization curves of op-LN and Pt/C.

Furthermore, the Li-air battery performance of op-LN is compared with that of Pt/C catalyst at an applied current density of 2.0 mA $cm^{-2}$ **(Figure 7.13)**. Even at this high current density, the discharge voltage profiles of both catalysts exhibit almost the same performances. However, the charge voltage profile of op-LN demonstrates lower overpotential than that of Pt/C catalyst, confirming its effective bi-functionality. To evaluate the rechargeablitiy of the catalyst, discharge and charge cycle tests have been carried out with two different test patterns as shown in **Figure 7.14(a) and (b)**. The cycle performance for 10 min. at 0.5 mA $cm^{-2}$ during each cycle demonstrates stable discharge and charge voltage over more than 80 cycles. The end voltages of each process at $100^{th}$ cycle are 2.86 V and 3.91 V which are very similar to 2.90 V and 3.84 V in the $1^{st}$ cycle, respectively **(Figure 7.14(a))**. In addition, the high energy cycle stability during 2 hr cycling at the current density of 0.3 mA $cm^{-2}$ was investigated, as shown in **Figure 7.14(b)**. The voltage differences of the discharge and charge process between the $1^{st}$ cycle and $15^{th}$ cycle

are only 0.09 V and 0.14 V, respectively. These results in a practical Li-air battery are consistent with the prior half-cell tests, confirming sufficient bi-functional catalytic activities of the developed catalyst. It also highlights the practical advantages of the facile one-pot synthesis for the LSCF-based NCNT composite catalyst and its effective composition and morphology as a highly promising bi-functional catalyst.

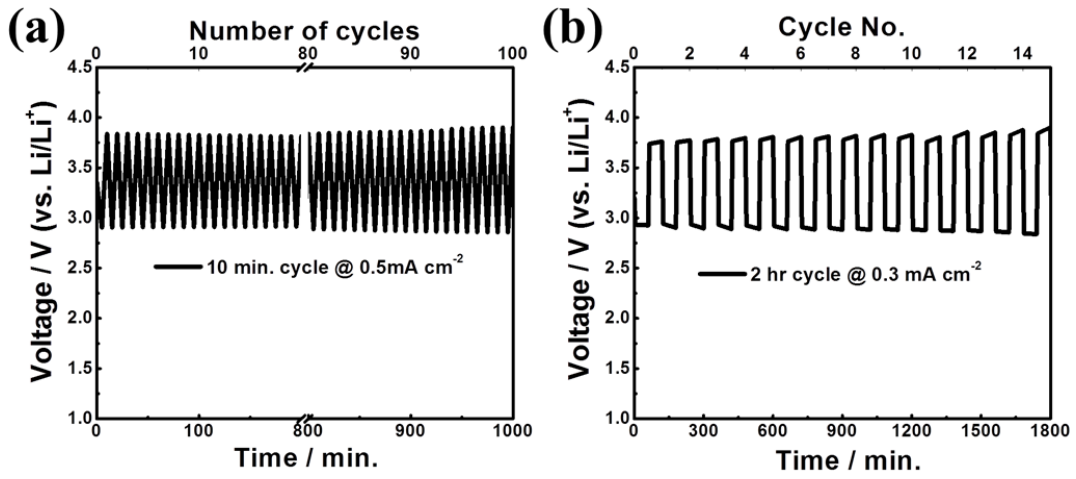


**Figure 7.14** Li-air battery performance of op-LN. D/C cycling profile of op-LN for (c) 10 min. at 0.5 mA $cm^{-2}$ and (d) 2 hr at 0.3 mA $cm^{-2}$.

## 7.4 Summary

In this study, a facile one-pot synthetic method was used to prepare a LSCF-based NCNT composite (op-LN) as a bi-functional catalyst in a Li-air battery. The method combines the simple calcination synthesis for LSCF-NP and injection CVD for NCNT as introduced in the previous chapter. The electron microscope images revealed the effectiveness of the novel morphology of the composite for the bi-functionality during the oxygen reactions. According to

the half-cell tests, the incorporation of NCNT into LSCF-NP not only dramatically enhances ORR performance, but also played a key role in improving the OER activity through a synergistic effect. It is speculated that the composition of the core material and the corona-structured NCNT on the metal oxide provide outstanding catalytic activities for both ORR and OER. To demonstrate its practicality for metal-air battery applications, the catalyst was tested as a cathode material in a realistic Li-air battery prototype. The performance shows that the catalyst exhibits excellent bi-functional activity with stable discharge and charge voltages at various applied current densities in addition to cycle stability for 2 hr at 0.3 mA $cm^{-2}$. This work demonstrates advancements in the development of a one-pot synthesis and a metal oxide/NCNT composite with effective structure for a bi-functional catalyst in alkaline electrolytes. With this facile synthesis technique and excellent electrochemical results, this approach to produce bi-functional catalysts promises to be an up-and-coming strategy for metal-air batteries.

# 8. Conclusions and Recommendations

## 8.1 Conclusions

In this study, highly-active, cost-effective and process-friendly electrochemical bi-functional catalysts active toward ORR and OER in alkaline media were developed using 1-D and 2-D graphitic carbon and perovskite oxide.

First, the research focused on the one-step synthesis of thermally reduced nitrogen-doped graphene sheets (NRGO) utilizing a rapid heating rate, which presented interesting 2-D morphology. The chemical properties and catalytic activities were controlled by the synthetic process primarily by changing the reaction temperature which resulted in highly active ORR performance of the catalyst. In a half-cell testing, NRGO produced at 1100 $^{o}$C showed comparable ORR activity to that of state-of-the-art Pt/C catalyst. This outstanding catalytic performance and unique morphology makes metal-free NRGO a promising candidate as practical ORR catalyst as well as elctrocatalytically active catalyst support material for metal-air batteries. Based on the study of the formation and the catalytic activity of NRGO, high surface area perovskite oxide/NRGO composite as highly active bi-functional catalysts for rechargeable metal-air battery applications was developed. Utilizing the electrospinning method, the novel porous nanorod morphology of LSCF-PR was prepared and confirmed by electron microscopes. The higher surface area and the enhanced catalytic activity toward OER of LSCF-PR were confirmed by the BET measurement and the half-cell testing, compared to those of LSCF nanoparticles. The uniform distribution of LSCF-PR throughout the network of NRGO sheets

created LSCF-PR/NRGO composite morphology as an efficient bi-functional catalyst. The electrochemical performances of the composite highlighted the excellent catalytic activity and better durability (compared to Pt/C) for both the ORR and OER in alkaline electrolyte. LSCF-PR was found to provide the majority of the OER activity, whereas NRGO provides the majority of the ORR active, resulting in a complementary bi-functional catalyst composite arrangement. Therefore, it is believed that the combination of the high surface area and highly active perovskite oxide, and effectively synthesized NRGO is a promising approach for the preparation of excellent bi-functional catalysts for rechargeable metal-air batteries.

Besides NRGO, the catalytic activity of 1-D graphitic carbon of nitrogen-doped carbon nanotube (NCNT) was studied, introducing the novel structure of NCNT and reduced graphene oxide (RGO) composite (NCNT/RGO). After growing NCNT on RGO by injection CVD method, the novel morphology of the NCNT-bridged RGO composite was characterized by the SEM and TEM images, and XPS results revealed chemical elements in NCNT/RGO which supported successful nitrogen-doping of CNT. NCNT/RGO in this study not only demonstrated comparable ORR activity to that of state-of-the-art Pt/C catalyst via four electron reduction pathway, but also presented good OER activity and durability in the full voltage range. Consequently, this study revealed NCNT as also a good candidate for preparing bi-functional catalyst by combining with other catalysts. It is worth noting that 1-D NCNT is not only simply synthesized via the one step method but also NCNT grows readily on desired surfaces, while 2-D NRGO needs complicated steps to be prepared such as the graphite oxidation. These merits of 1-D NCNT was the inspiration for designing a facile and one-pot synthetic method for the preparation of perovskite oxide-based NCNT composite as a bi-functional catalyst. Particularly, the simple calcination synthesis for LSCF-NP was combined with the injection CVD method for

NCNT to obtain the composite bi-functional catalyst. The electron microscope images revealed the novel and effective morphology of the composite for the bi-functionality toward oxygen reactions. According to the half-cell testing, the incorporation of NCNT on LSCF-NP not only enhanced ORR performance compared to the Pt/C catalyst but also improved OER activity by the synergistic combination. It is speculated that the composition of the core perovskite and corona-structured NCNT grown on the surface provide outstanding catalytic activities synergistically for both ORR and OER. In order to demonstrate its practical battery performance, the composite catalyst was applied into the cathode of a realistic Li-air battery prototype. The battery showed consistent performance with the result from the half-cell testing, demonstrating stable discharge and charge voltages at various applied current densities in addition to cycle stability for 2 hr at 0.3 mA $cm^{-2}$. This work directly demonstrates advancement in the development of one-pot synthesis and the composite of effective composition of a metal oxide and NCNT as a bi-functional catalyst in alkaline electrolytes.

## 8.2 Recommendations

In this study, the effective electrochemical bi-functional catalysts were developed using 1-D and 2-D heteroatom doped graphitic carbon and perovskite oxides, and these catalysts performed excellent catalytic activities for ORR and OER, which are associated with discharge and charge performances for rechargeable metal-air batteries, respectively. It is speculated that efficient interaction between carbon and perovskite oxide during preparation of the composite catalyst could be significant to improve their catalytic activities by synergetic effect. In addition,

the durability of catalysts still needs to be improved especially in the OER potential region for long term cycle stability in rechargeable metal-air batteries. Here, recommended works are proposed below for future studies.

**1.** Embedded perovskite oxide nanoparticle into porous carbon fiber for improved catalytic activities.

Most metal oxide catalysts suffer from their relatively poor electrical conductivity, which compels to employ carbon support. Continuously providing an electron pathway on metal oxide catalysts is significant to maximize their catalytic activities. Furthermore, incorporation of heteroatom into the carbon fiber will enhance reaction kinetics for ORR and OER. Specific suggestion for the composite catalyst is described as below:

- Perovskite oxide nanoparticles embedded nitrogen or sulfur doped porous carbon fibers can be prepared by the electrospinning method.
    - Synthesize perovskite oxide nanoparticles by hydrothermal reaction with proper surfactant and then disperse the nanoparticles into nitrogen or sulfur containing polymer solution to obtain the electrospun fibers.
    - Control the pyrolysis conditions of the electrospun fiber by ramping rate and temperature to produce the perovskite oxide embedded hetero atom-doped porous carbon fibers for the bi-functional catalyst.

**2.** Develop effective composite morphology of graphitic carbon materials and perovskite oxide composite reducing exposed surface area of carbon support to improve durability.

In general, the durability of carbon composite catalysts relies on the stability of carbon material since the high positive potential within the OER region accelerates carbon corrosion. Therefore, the effective way to prepare a highly durable catalyst is minimizing exposed surface area of a carbon support. In contrast, maximizing surface area of perovskite oxide is essentially needed to obtain a superior catalyst as studied in Chapter 5. Consequently, preparing high surface area perovskite oxide and covering NCNT by the perovskite oxide can be a promising strategy to create highly durable and active bi-functional catalysts.

Several recommendations could be proposed.

- High surface area and porous perovskite oxide with large pore size can be prepared by electrospinning method, hydrothermal (or solvothermal) synthesis, or highly ordered polymer template and then NCNT can be grown directly into the pores.
    - Control the concentration of metal precursor and polymer amount to produce larger pore size and longer diameter of the porous rod of perovskite oxide.
    - Develop hydrothermal (or solvothermal) synthetic procedures using polymeric surfactants to prepare porous perovskite oxide.
    - Using highly ordered polymer template (such as polystyrene beads), 3-dimensionally ordered porous perovskite oxide can be synthesized.

- Besides the CVD method, investigate a solution-based synthetic method to synthesize nitrogen-doped carbon nanotube (NCNT) into the pores of the perovskite oxide.

- Prepare nanoparticles of perovskite oxide smaller than the diameter of NCNT then deposit the nanoparticles onto the surface of NCNT.
  - Applying hydrothermal reaction with a long-chain hydrocarbon surfactant to synthesize perovskite oxide nanoparticles then deposit the nanoparticles onto NCNT utilizing hydrophobic-hydrophobic interaction.

Besides perovskite oxides, spinel structured metal oxides can be applied since the spinel oxides have also been reported as promising non-precious bi-functional catalysts for metal-air battery applications.

# References


[1] Cheng, F. Y.; Chen, J., Metal-air batteries: from oxygen reduction electrochemistry to cathode catalysts. *Chem. Soc. Rev.* **2012,** *41* (6), 2172.

[2] Girishkumar, G.; McCloskey, B.; Luntz, A. C.; Swanson, S.; Wilcke, W., Lithium - Air Battery: Promise and Challenges. *J. Phys. Chem. Lett.* **2010,** *1* (14), 2193.

[3] Lee, J. S.; Kim, S. T.; Cao, R.; Choi, N. S.; Liu, M.; Lee, K. T.; Cho, J., Metal-Air Batteries with High Energy Density: Li-Air versus Zn-Air. *Adv. Energy Mater.* **2011,** *1* (1), 34.

[4] Bruce, P. G.; Freunberger, S. A.; Hardwick, L. J.; Tarascon, J. M., Li-$O_2$ and Li-S batteries with high energy storage. *Nat. Mater.* **2012,** *11* (1), 19.

[5] Hamdani, M.; Singh, R. N.; Chartier, P., $Co_3O_4$ and Co-Based Spinel Oxides Bifunctional Oxygen Electrodes. *Int. J. Electrochem. Sci.* **2010,** *5* (4), 556.

[6] Li, Y. G.; Gong, M.; Liang, Y. Y.; Feng, J.; Kim, J. E.; Wang, H. L.; Hong, G. S.; Zhang, B.; Dai, H. J., Advanced zinc-air batteries based on high-performance hybrid electrocatalysts. *Nat. Commun.* **2013,** *4*.

[7] Muller, S.; Holzer, F.; Arai, H.; Haas, O., A study of carbon-catalyst interaction in bifunctional air electrodes for zinc-air batteries. *J. New Mater. Electrochem. Syst.* **1999,** *2* (4), 227.

[8] Zhang, S. S.; Yuan, X. Z.; Hin, J. N. C.; Wang, H. J.; Friedrich, K. A.; Schulze, M., A review of platinum-based catalyst layer degradation in proton exchange membrane fuel cells. *J. Power Sources* **2009,** *194* (2), 588.

[9] Morozan, A.; Jousselme, B.; Palacin, S., Low-platinum and platinum-free catalysts for the oxygen reduction reaction at fuel cell cathodes. *Energy Environ. Sci.* **2011,** *4* (4), 1238.

[10] Seo, M. H.; Choi, S. M.; Kim, H. J.; Kim, W. B., The graphene-supported Pd and Pt catalysts for highly active oxygen reduction reaction in an alkaline condition. *Electrochem. Commun.* **2011,** *13* (2), 182.

[11] Norskov, J. K.; Rossmeisl, J.; Logadottir, A.; Lindqvist, L.; Kitchin, J. R.; Bligaard, T.; Jonsson, H., Origin of the overpotential for oxygen reduction at a fuel-cell cathode. *J. Phys. Chem. B* **2004,** *108* (46), 17886.

[12] Sheng, W. C.; Chen, S.; Vescovo, E.; Shao-Horn, Y., Size Influence on the Oxygen Reduction Reaction Activity and Instability of Supported Pt Nanoparticles. *J. Electrochem. Soc.* **2012,** *159* (2), B96.

[13] Lu, Y. C.; Xu, Z. C.; Gasteiger, H. A.; Chen, S.; Hamad-Schifferli, K.; Shao-Horn, Y., Platinum-Gold Nanoparticles: A Highly Active Bifunctional Electrocatalyst for Rechargeable Lithium-Air Batteries. *J. Am. Chem. Soc.* **2010,** *132* (35), 12170.

[14] Li, L.; Chai, S.-H.; Dai, S.; Manthiram, A., Advanced hybrid Li-air batteries with high-performance mesoporous nanocatalysts. *Energy Environ. Sci.* **2014,** *7* (8), 2630.

[15] Suntivich, J.; Gasteiger, H. A.; Yabuuchi, N.; Nakanishi, H.; Goodenough, J. B.; Shao-Horn, Y., Design principles for oxygen-reduction activity on perovskite oxide catalysts for fuel cells and metal-air batteries (vol 3, pg 546, 2011). *Nat. Chem.* **2011,** *3* (8), 647.

[16] Grimaud, A.; May, K. J.; Carlton, C. E.; Lee, Y. L.; Risch, M.; Hong, W. T.; Zhou, J. G.; Yang, S. H., Double perovskites as a family of highly active catalysts for oxygen evolution in alkaline solution. *Nat. Commun.* **2013,** *4*.

[17] Zhao, Y. L.; Xu, L.; Mai, L. Q.; Han, C. H.; An, Q. Y.; Xu, X.; Liu, X.; Zhang, Q. J., Hierarchical mesoporous perovskite $La_{0.5}Sr_{0.5}CoO_{2.91}$ nanowires with ultrahigh capacity for Li-air batteries. *Proc. Natl. Acad. Sci. USA* **2012,** *109* (48), 19569.

[18] Xu, J. J.; Xu, D.; Wang, Z. L.; Wang, H. G.; Zhang, L. L.; Zhang, X. B., Synthesis of Perovskite-Based Porous $La_{0.75}Sr_{0.25}MnO_3$ Nanotubes as a Highly Efficient Electrocatalyst for Rechargeable LithiumOxygen Batteries. *Angew. Chem. Int. Ed.* **2013,** *52* (14), 3887.

[19] Garcia, E. M.; Taroco, H. A.; Matencio, T.; Domingues, R. Z.; dos Santos, J. A. F., Electrochemical study of $La_{0.6}Sr_{0.4}Co_{0.8}Fe_{0.2}O_3$ during oxygen evolution reaction. *Int. J. Hydrogen Energy* **2012,** *37* (8), 6400.

[20] Jin, C.; Cao, X. C.; Lu, F. L.; Yang, Z. R.; Yang, R. Z., Electrochemical study of $Ba_{0.5}Sr_{0.5}Co_{0.8}Fe_{0.2}O_3$ perovskite as bifunctional catalyst in alkaline media. *Int. J. Hydrogen Energy* **2013,** *38* (25), 10389.

[21] Suntivich, J.; May, K. J.; Gasteiger, H. A.; Goodenough, J. B.; Shao-Horn, Y., A Perovskite Oxide Optimized for Oxygen Evolution Catalysis from Molecular Orbital Principles. *Science* **2011,** *334* (6061), 1383.

[22] Reddy, T. B., Linden's Handbook of Batteries. *McGraw-hill* **2010,** *4th Edition*.

[23] Christensen, J.; Albertus, P.; Sanchez-Carrera, R. S.; Lohmann, T.; Kozinsky, B.; Liedtke, R.; Ahmed, J.; Kojic, A., A Critical Review of Li/Air Batteries. *J. Electrochem. Soc.* **2012,** *159* (2), R1.

[24] Galbraith, A. D., The lithium-water-air battery for automotive propulsion. *Union Internationale des Producteurs et Distributeurs d'Energie Electrique and Electric Vehicle Council, International Electric Vehicle Symposium, 4th, Duesseldorf, West Germany* **1976**, 23.

[25] Abraham, K. M.; Jiang, Z., A polymer electrolyte-based rechargeable lithium/oxygen battery. *J. Electrochem. Soc.* **1996,** *143* (1), 1.

[26] Ogasawara, T.; Debart, A.; Holzapfel, M.; Novak, P.; Bruce, P. G., Rechargeable $Li_2O_2$ electrode for lithium batteries. *J. Am. Chem. Soc.* **2006,** *128* (4), 1390.

[27] Crowther, O.; Keeny, D.; Moureau, D. M.; Meyer, B.; Salomon, M.; Hendrickson, M., Electrolyte optimization for the primary lithium metal air battery using an oxygen selective membrane. *J. Power Sources* **2012,** *202*, 347.

[28] Debart, A.; Paterson, A. J.; Bao, J.; Bruce, P. G., alpha-$MnO_2$ nanowires: A catalyst for the $O_2$ electrode in rechargeable lithium batteries. *Angew. Chem. Int. Ed.* **2008,** *47* (24), 4521.

[29] Lee, J.-H.; Black, R.; Popov, G.; Pomerantseva, E.; Nan, F.; Botton, G. A.; Nazar, L. F., The role of vacancies and defects in $Na_{0.44}MnO_2$ nanowire catalysts for lithium/oxygen batteries. *Energy & Environmental Science* **2012**, *5*, 9558.

[30] Debart, A.; Bao, J.; Armstrong, G.; Bruce, P. G., An $O_2$ cathode for rechargeable lithium batteries: The effect of a catalyst. *J. Power Sources* **2007,** *174* (2), 1177.

[31] Lu, Y. C.; Gasteiger, H. A.; Shao-Horn, Y., Catalytic Activity Trends of Oxygen Reduction Reaction for Nonaqueous Li-Air Batteries. *J. Am. Chem. Soc.* **2011,** *133* (47), 19048.

[32] Cheng, H.; Scott, K., Carbon-supported manganese oxide nanocatalysts for rechargeable lithium-air batteries. *J. Power Sources* **2010,** *195* (5), 1370.

[33] Lu, Y. C.; Gasteiger, H. A.; Crumlin, E.; McGuire, R.; Shao-Horn, Y., Electrocatalytic Activity Studies of Select Metal Surfaces and Implications in Li-Air Batteries. *J. Electrochem. Soc.* **2010,** *157* (9), A1016.

[34] Laoire, C. O.; Mukerjee, S.; Abraham, K. M.; Plichta, E. J.; Hendrickson, M. A., Elucidating the Mechanism of Oxygen Reduction for Lithium-Air Battery Applications. *J. Phys. Chem. C* **2009,** *113* (46), 20127.

[35] Xiao, J.; Mei, D. H.; Li, X. L.; Xu, W.; Wang, D. Y.; Graff, G. L.; Bennett, W. D.; Nie, Z. M.; Saraf, L. V.; Aksay, I. A.; Liu, J.; Zhang, J. G., Hierarchically Porous Graphene as a Lithium-Air Battery Electrode. *Nano Lett.* **2011,** *11* (11), 5071.

[36] Wang, Z. L.; Xu, D.; Xu, J. J.; Zhang, L. L.; Zhang, X. B., Graphene Oxide Gel-Derived, Free-Standing, Hierarchically Porous Carbon for High-Capacity and High-Rate Rechargeable Li-$O_2$ Batteries. *Adv. Funct. Mater.* **2012,** *22* (17), 3699.

[37] Li, Y. L.; Wang, J. J.; Li, X. F.; Geng, D. S.; Banis, M. N.; Li, R. Y.; Sun, X. L., Nitrogen-doped graphene nanosheets as cathode materials with excellent electrocatalytic activity for high capacity lithium-oxygen batteries. *Electrochem. Commun.* **2012,** *18*, 12.

[38] Li, Y. L.; Wang, J. J.; Li, X. F.; Geng, D. S.; Li, R. Y.; Sun, X. L., Superior energy capacity of graphene nanosheets for a nonaqueous lithium-oxygen battery. *Chem. Commun.* **2011,** *47* (33), 9438.

[39] Wang, L.; Zhao, X.; Lu, Y. H.; Xu, M. W.; Zhang, D. W.; Ruoff, R. S.; Stevenson, K. J.; Goodenough, J. B., $CoMn_2O_4$ Spinel Nanoparticles Grown on Graphene as Bifunctional Catalyst for Lithium-Air Batteries. *J. Electrochem. Soc.* **2011,** *158* (12), A1379.

[40] Wang, H. L.; Yang, Y.; Liang, Y. Y.; Zheng, G. Y.; Li, Y. G.; Cui, Y.; Dai, H. J., Rechargeable Li-$O_2$ batteries with a covalently coupled $MnCo_2O_4$-graphene hybrid as an oxygen cathode catalyst. *Energy Environ. Sci.* **2012,** *5* (7), 7931.

[41] Thapa, A. K.; Saimen, K.; Ishihara, T., Pd/$MnO_2$ Air Electrode Catalyst for Rechargeable Lithium/Air Battery. *Electrochem. Soid-State Lett.* **2010,** *13* (11), A165.

[42] Freunberger, S. A.; Chen, Y. H.; Peng, Z. Q.; Griffin, J. M.; Hardwick, L. J.; Barde, F.; Novak, P.; Bruce, P. G., Reactions in the Rechargeable Lithium-$O_2$ Battery with Alkyl Carbonate Electrolytes. *J. Am. Chem. Soc.* **2011,** *133* (20), 8040.

[43] McCloskey, B. D.; Bethune, D. S.; Shelby, R. M.; Girishkumar, G.; Luntz, A. C., Solvents' Critical Role in Nonaqueous Lithium-Oxygen Battery Electrochemistry. *J. Phys. Chem. Lett.* **2011,** *2* (10), 1161.

[44] McCloskey, B. D.; Scheffler, R.; Speidel, A.; Bethune, D. S.; Shelby, R. M.; Luntz, A. C., On the Efficacy of Electrocatalysis in Nonaqueous Li-$O_2$ Batteries. *J. Am. Chem. Soc.* **2011,** *133* (45), 18038.

[45] Laoire, C. O.; Mukerjee, S.; Abraham, K. M.; Plichta, E. J.; Hendrickson, M. A., Influence of Nonaqueous Solvents on the Electrochemistry of Oxygen in the Rechargeable Lithium-Air Battery. *J. Phys. Chem. C* **2010,** *114* (19), 9178.

[46] Cecchetto, L.; Salomon, M.; Scrosati, B.; Croce, F., Study of a Li-air battery having an electrolyte solution formed by a mixture of an ether-based aprotic solvent and an ionic liquid. *J. Power Sources* **2012,** *213*, 233.

[47] Freunberger, S. A.; Chen, Y. H.; Drewett, N. E.; Hardwick, L. J.; Barde, F.; Bruce, P. G., The Lithium-Oxygen Battery with Ether-Based Electrolytes. *Angew. Chem. Int. Ed.* **2011,** *50* (37), 8609.

[48] Visco, S. J.; Nimon, Y. S., Active Metal/Aqueous Electrochemical Cells and Systems. *U.S. Patent* **2010,** *7,666*, 233.

[49] Wang, Y. G.; Zhou, H. S., A lithium-air battery with a potential to continuously reduce $O_2$ from air for delivering energy. *J. Power Sources* **2010,** *195* (1), 358.

[50] Zhou, H. S.; Wang, Y. G.; Li, H. Q.; He, P., The Development of a New Type of Rechargeable Batteries Based on Hybrid Electrolytes. *Chemsuschem* **2010,** *3* (9), 1009.

[51] Neburchilov, V.; Wang, H. J.; Martin, J. J.; Qu, W., A review on air cathodes for zinc-air fuel cells. *J. Power Sources* **2010,** *195* (5), 1271.

[52] Linden, D.; Thomas, B. R., *Hnadbook of batteries, 3rd edition, McGraw-Hill* **2001**.

[53] Jorissen, L., Bifunctional oxygen/air electrodes. *J. Power Sources* **2006,** *155* (1), 23.

[54] Bockris, J. O.; Otagawa, T., The Electrocatalysis of Oxygen Evolution on Perovskites. *J. Electrochem. Soc.* **1984,** *131* (2), 290.

[55] Lee, Y.; Suntivich, J.; May, K. J.; Perry, E. E.; Shao-Horn, Y., Synthesis and Activities of Rutile $IrO_2$ and $RuO_2$ Nanoparticles for Oxygen Evolution in Acid and Alkaline Solutions. *J. Phys. Chem. Lett.* **2012,** *3* (3), 399.

[56] Gorlin, Y.; Jaramillo, T. F., A Bifunctional Nonprecious Metal Catalyst for Oxygen Reduction and Water Oxidation. *J. Am. Chem. Soc.* **2010,** *132* (39), 13612.

[57] Ishihara, T., Perovskite Oxide for Solid Oxide Fuel Cells. *Springer* **2009**.

[58] Zhou, W.; Ran, R.; Shao, Z.; Zhuang, W.; Jia, J.; Gu, H.; Jin, W.; Xu, N., Barium- and strontium-enriched $(Ba_{0.5}Sr_{0.5})_{1+x}Co_{0.8}Fe_{0.2}O_{3-\delta}$ oxides as high-performance cathodes for intermediate-temperature solid-oxide fuel cells. *Acta Mater.* **2008,** *56* (12), 2687.

[59] Du, J.; Zhang, T.; Cheng, F.; Chu, W.; Wu, Z.; Chen, J., Nonstoichiometric Perovskite $CaMnO_{3-\delta}$ for Oxygen Electrocatalysis with High Activity. *Inorg. Chem.* **2014,** *53* (17), 9106.

[60] Yang, W.; Salim, J.; Li, S.; Sun, C.; Chen, L.; Goodenough, J. B.; Kim, Y., Perovskite $Sr_{0.95}Ce_{0.05}CoO_{3-\delta}$ loaded with copper nanoparticles as a bifunctional catalyst for lithium-air batteries. *J. Mater. Chem.* **2012,** *22* (36), 18902.

[61] Xu, J.-J.; Wang, Z.-L.; Xu, D.; Meng, F.-Z.; Zhang, X.-B., 3D ordered macroporous $LaFeO_3$ as efficient electrocatalyst for Li-O2 batteries with enhanced rate capability and cyclic performance. *Energy Environ. Sci.* **2014**, DOI: 10.1039/c3ee42934b.

[62] Park, H. W.; Lee, D. U.; Liu, Y.; Wu, J.; Nazar, L. F.; Chen, Z., Bi-Functional N-Doped CNT/Graphene Composite as Highly Active and Durable Electrocatalyst for Metal Air Battery Applications. *J. Electrochem. Soc.* **2013,** *160* (11), A2244.

[63] Chen, Z.; Yu, A. P.; Higgins, D.; Li, H.; Wang, H. J.; Chen, Z. W., Highly Active and Durable Core-Corona Structured Bifunctional Catalyst for Rechargeable Metal-Air Battery Application. *Nano Lett.* **2012,** *12* (4), 1946.

[64] Lambert, T. N.; Davis, D. J.; Lu, W.; Limmer, S. J.; Kotula, P. G.; Thuli, A.; Hungate, M.; Ruan, G.; Jin, Z.; Tour, J. M., Graphene-Ni-α-$MnO_2$ and -Cu-α-$MnO_2$ nanowire blends as highly active non-precious metal catalysts for the oxygen reduction reaction. *Chem. Commun.* **2012,** *48* (64), 7931.

[65] Liang, Y. Y.; Li, Y. G.; Wang, H. L.; Zhou, J. G.; Wang, J.; Regier, T.; Dai, H. J., $Co_3O_4$ nanocrystals on graphene as a synergistic catalyst for oxygen reduction reaction. *Nat. Mater.* **2011,** *10* (10), 780.

[66] Pei, S. F.; Cheng, H. M., The reduction of graphene oxide. *Carbon* **2012,** *50* (9), 3210.

[67] Liu, J. Q.; Tang, J. G.; Gooding, J. J., Strategies for chemical modification of graphene and applications of chemically modified graphene. *J. Mater. Chem.* **2012,** *22* (25), 12435.

[68] Zhu, Y. W.; Stoller, M. D.; Cai, W. W.; Velamakanni, A.; Piner, R. D.; Chen, D.; Ruoff, R. S., Exfoliation of Graphite Oxide in Propylene Carbonate and Thermal Reduction of the Resulting Graphene Oxide Platelets. *Acs Nano* **2010,** *4* (2), 1227.

[69] Wu, Z.-S.; Zhou, G.; Yin, L.-C.; Ren, W.; Li, F.; Cheng, H.-M., Graphene/metal oxide composite electrode materials for energy storage. *Nano Energy* **2012,** *1* (1), 107.

[70] http://manojkumars.wordpress.com/2011/04/14/graphene/.

[71] Liao, K. H.; Mittal, A.; Bose, S.; Leighton, C.; Mkhoyan, K. A.; Macosko, C. W., Aqueous Only Route toward Graphene from Graphite Oxide. *Acs Nano* **2011,** *5* (2), 1253.

[72] Zhou, T. N.; Chen, F.; Liu, K.; Deng, H.; Zhang, Q.; Feng, J. W.; Fu, Q. A., A simple and efficient method to prepare graphene by reduction of graphite oxide with sodium hydrosulfite. *Nanotechnology* **2011,** *22* (4).

[73] Xu, C.; Wang, X.; Yang, L. C.; Wu, Y. P., Fabrication of a graphene-cuprous oxide composite. *J. Solid State Chem.* **2009,** *182* (9), 2486.

[74] Ma, Y.-w.; Liu, Z.-r.; Wang, B.-l.; Zhu, L.; Yang, J.-p.; Li, X.-a., Preparation of graphene-supported Pt-Co nanoparticles and their use in oxygen reduction reactions. *New Carbon Mater.*. **2012,** *27* (4), 250.

[75] Choi, S. M.; Seo, M. H.; Kim, H. J.; Kim, W. B., Synthesis of surface-functionalized graphene nanosheets with high Pt-loadings and their applications to methanol electrooxidation. *Carbon* **2011,** *49* (3), 904.

[76] Yang, S. B.; Zhi, L. J.; Tang, K.; Feng, X. L.; Maier, J.; Mullen, K., Efficient Synthesis of Heteroatom (N or S)-Doped Graphene Based on Ultrathin Graphene Oxide-Porous Silica Sheets for Oxygen Reduction Reactions. *Adv. Funct. Mater.* **2012,** *22* (17), 3634.

[77] Sheng, Z. H.; Gao, H. L.; Bao, W. J.; Wang, F. B.; Xia, X. H., Synthesis of boron doped graphene for oxygen reduction reaction in fuel cells. *J. Mater. Chem.* **2012,** *22* (2), 390.

[78] Liang, J.; Jiao, Y.; Jaroniec, M.; Qiao, S. Z., Sulfur and Nitrogen Dual-Doped Mesoporous Graphene Electrocatalyst for Oxygen Reduction with Synergistically Enhanced Performance. *Angew. Chem. Int. Ed.* **2012,** *51* (46), 11496.

[79] Yang, Z.; Yao, Z.; Li, G.; Fang, G.; Nie, H.; Liu, Z.; Zhou, X.; Chen, X. a.; Huang, S., Sulfur-Doped Graphene as an Efficient Metal-free Cathode Catalyst for Oxygen Reduction. *Acs Nano* **2011,** *6* (1), 205.

[80] Qu, L. T.; Liu, Y.; Baek, J. B.; Dai, L. M., Nitrogen-Doped Graphene as Efficient Metal-Free Electrocatalyst for Oxygen Reduction in Fuel Cells. *Acs Nano* **2010,** *4* (3), 1321.

[81] Yoo, E.; Zhou, H. S., Li-Air Rechargeable Battery Based on Metal-free Graphene Nanosheet Catalysts. *Acs Nano* **2011,** *5* (4), 3020.

[82] Lee, J. S.; Lee, T.; Song, H. K.; Cho, J.; Kim, B. S., Ionic liquid modified graphene nanosheets anchoring manganese oxide nanoparticles as efficient electrocatalysts for Zn-air batteries. *Energy Environ. Sci.* **2011,** *4* (10), 4148.

[83] Prasek, J.; Drbohlavova, J.; Chomoucka, J.; Hubalek, J.; Jasek, O.; Adam, V.; Kizek, R., Methods for carbon nanotubes synthesis-review. *J. Mater. Chem.* **2011,** *21* (40), 15872.

[84] Sharma, S.; Pollet, B. G., Support materials for PEMFC and DMFC electrocatalysts—A review. *J. Power Sources* **2012,** *208* (0), 96.

[85] Park, S.; Shao, Y.; Kou, R.; Viswanathan, V. V.; Towne, S. A.; Rieke, P. C.; Liu, J.; Lin, Y.; Wang, Y., Polarization Losses under Accelerated Stress Test Using Multiwalled Carbon Nanotube Supported Pt Catalyst in PEM Fuel Cells. *J. Electrochem. Soc.* **2011,** *158* (3), B297.

[86] Yang, L.; Jiang, S.; Zhao, Y.; Zhu, L.; Chen, S.; Wang, X.; Wu, Q.; Ma, J.; Ma, Y.; Hu, Z., Boron-Doped Carbon Nanotubes as Metal-Free Electrocatalysts for the Oxygen Reduction Reaction. *Angew. Chem. Int. Ed.* **2011,** *50* (31), 7132.

[87] Gong, K. P.; Du, F.; Xia, Z. H.; Durstock, M.; Dai, L. M., Nitrogen-Doped Carbon Nanotube Arrays with High Electrocatalytic Activity for Oxygen Reduction. *Science* **2009,** *323* (5915), 760.

[88] Sharifi, T.; Nitze, F.; Barzegar, H. R.; Tai, C. W.; Mazurkiewicz, M.; Malolepszy, A.; Stobinski, L.; Wagberg, T., Nitrogen doped multi walled carbon nanotubes produced by CVD-correlating XPS and Raman spectroscopy for the study of nitrogen inclusion. *Carbon* **2012,** *50* (10), 3535.

[89] Mabena, L.; Sinha Ray, S.; Mhlanga, S.; Coville, N., Nitrogen-doped carbon nanotubes as a metal catalyst support. *Appl. Nanosci.* **2011,** *1* (2), 67.

[90] Chen, Z.; Higgins, D.; Tao, H.; Hsu, R. S.; Chen, Z., Highly Active Nitrogen-Doped Carbon Nanotubes for Oxygen Reduction Reaction in Fuel Cell Applications. *J. Phys. Chem. C* **2009,** *113* (49), 21008.

[91] Zhu, S. M.; Chen, Z.; Li, B.; Higgins, D.; Wang, H. J.; Li, H.; Chen, Z. W., Nitrogen-doped carbon nanotubes as air cathode catalysts in zinc-air battery. *Electrochim. Acta* **2011,** *56* (14), 5080.

[92] Hummers, W. S.; Offeman, R. E., Preparation of Graphitic Oxide. *Journal of the American Chemical Society* **1958,** *80* (6), 1339.

[93] Marcano, D. C.; Kosynkin, D. V.; Berlin, J. M.; Sinitskii, A.; Sun, Z. Z.; Slesarev, A.; Alemany, L. B.; Lu, W.; Tour, J. M., Improved Synthesis of Graphene Oxide. *Acs Nano* **2010,** *4* (8), 4806.

[94] Cavaliere, S.; Subianto, S.; Savych, I.; Jones, D. J.; Roziere, J., Electrospinning: designed architectures for energy conversion and storage devices. *Energy Environ. Sci.* **2011,** *4* (12), 4761.

[95] Thavasi, V.; Singh, G.; Ramakrishna, S., Electrospun nanofibers in energy and environmental applications. *Energy Environ. Sci.* **2008,** *1* (2), 205.

[96] Teo, W. E.; Ramakrishna, S., A review on electrospinning design and nanofibre assemblies. *Nanotechnology* **2006,** *17* (14), R89.

[97] Flegler, S. L.; Heckman Jr., J. W.; Klomparens, K. L., Scanning and Transmission Electron Microscopy. *W.H. Freeman and Company* **1993**.

[98] Brunauer, S.; Emmett, P. H.; Teller, E., Adsorption of Gases in Multimolecular Layers. *J. Am. Chem. Soc.* **1938,** *60* (2), 309.

[99] Beller, M.; Renken, A.; Santen, R. A. v., Catalysis: From Principles to Applications. *Wiley-VCH* **2012**.

[100] Barrett, E. P.; Joyner, L. G.; Halenda, P. P., The Determination of Pore Volume and Area Distributions in Porous Substances. I. Computations from Nitrogen Isotherms. *J. Am. Chem. Soc.* **1951,** *73* (1), 373.

[101] de Boer, J. H.; Lippens, B. C.; Linsen, B. G.; Broekhoff, J. C. P.; van den Heuvel, A.; Osinga, T. J., Thet-curve of multimolecular $N_2$-adsorption. *J. Colloid Interface Sci.* **1966,** *21* (4), 405.

[102] Bard, A. J., Electrochemical Methods. *John Wiley & Sons* **1980**.

[103] Gileadi, E., Physical Electrochemistry. *Wiley-VCH* **2011**.

[104] Xiao, W.; Wang, D. L.; Lou, X. W., Shape-Controlled Synthesis of $MnO_2$ Nanostructures with Enhanced Electrocatalytic Activity for Oxygen Reduction. *J. Phys. Chem. C* **2010,** *114* (3), 1694.

[105] Qiao, J. L.; Xu, L.; Ding, L.; Shi, P. H.; Zhang, L.; Baker, R.; Zhang, J. J., Effect of KOH Concentration on the Oxygen Reduction Kinetics Catalyzed by Heat-Treated Co-Pyridine/C Electrocatalysts. *Int. J. Electrochem. Sci.* **2013,** *8* (1), 1189.

[106] Wu, G.; Cui, G. F.; Li, D. Y.; Shen, P. K.; Li, N., Carbon-supported $Co_{1.67}Te_2$ nanoparticles as electrocatalysts for oxygen reduction reaction in alkaline electrolyte. *J. Mater. Chem.* **2009,** *19* (36), 6581.

[107] Usachov, D.; Vilkov, O.; Gruneis, A.; Haberer, D.; Fedorov, A.; Adamchuk, V. K.; Preobrajenski, A. B.; Dudin, P.; Barinov, A.; Oehzelt, M.; Laubschat, C.; Vyalikh, D. V.,

Nitrogen-Doped Graphene: Efficient Growth, Structure, and Electronic Properties. *Nano Lett.* **2011,** *11* (12), 5401.

[108] Wang, H.; Wang, Q.; Cheng, Y.; Li, K.; Yao, Y.; Zhang, Q.; Dong, C.; Wang, P.; Schwingenschlögl, U.; Yang, W.; Zhang, X. X., Doping Monolayer Graphene with Single Atom Substitutions. *Nano Letters* **2011,** *12* (1), 141.

[109] Lee, S.; Cho, D.; Drzal, L. T., Real-time observation of the expansion behavior of intercalated graphite flake. *Journal of Materials Science* **2005,** *40* (1), 231.

[110] Celzard, A.; Mareche, J. F.; Furdin, G., Modelling of exfoliated graphite. *Progress in Materials Science* **2005,** *50* (1), 93.

[111] McAllister, M. J.; Li, J.-L.; Adamson, D. H.; Schniepp, H. C.; Abdala, A. A.; Liu, J.; Herrera-Alonso, M.; Milius, D. L.; Car, R.; Prud'homme, R. K.; Aksay, I. A., Single Sheet Functionalized Graphene by Oxidation and Thermal Expansion of Graphite. *Chemistry of Materials* **2007,** *19* (18), 4396.

[112] Geng, D.; Chen, Y.; Chen, Y.; Li, Y.; Li, R.; Sun, X.; Ye, S.; Knights, S., High oxygen-reduction activity and durability of nitrogen-doped graphene. *Energy & Environmental Science* **2011,** *4* (3).

[113] Dai, G.-P.; Zhang, J.-M.; Deng, S., Synthesis and characterization of nitrogen-doped monolayer and multilayer graphene on TEM copper grids. *Chemical Physics Letters* **2011,** *516* (4–6), 212.

[114] Qu, L.; Liu, Y.; Baek, J.-B.; Dai, L., Nitrogen-Doped Graphene as Efficient Metal-Free Electrocatalyst for Oxygen Reduction in Fuel Cells. *ACS Nano* **2010,** *4* (3), 1321.

[115] Jin, Z.; Yao, J.; Kittrell, C.; Tour, J. M., Large-Scale Growth and Characterizations of Nitrogen-Doped Monolayer Graphene Sheets. *ACS Nano* **2011,** *5* (5), 4112.

[116] Kudin, K. N.; Ozbas, B.; Schniepp, H. C.; Prud'homme, R. K.; Aksay, I. A.; Car, R., Raman Spectra of Graphite Oxide and Functionalized Graphene Sheets. *Nano Letters* **2007,** *8* (1), 36.

[117] Geng, D.; Yang, S.; Zhang, Y.; Yang, J.; Liu, J.; Li, R.; Sham, T.-K.; Sun, X.; Ye, S.; Knights, S., Nitrogen doping effects on the structure of graphene. *Applied Surface Science* **2011,** *257* (21), 9193.

[118] Jaouen, F. d. r.; Herranz, J.; Lefèvre, M.; Dodelet, J.-P.; Kramm, U. I.; Herrmann, I.; Bogdanoff, P.; Maruyama, J.; Nagaoka, T.; Garsuch, A.; Dahn, J. R.; Olson, T.; Pylypenko, S.;

Atanassov, P.; Ustinov, E. A., Cross-Laboratory Experimental Study of Non-Noble-Metal Electrocatalysts for the Oxygen Reduction Reaction. *ACS Applied Materials & Interfaces* **2009,** *1* (8), 1623.

[119] Matter, P. H.; Zhang, L.; Ozkan, U. S., The role of nanostructure in nitrogen-containing carbon catalysts for the oxygen reduction reaction. *Journal of Catalysis* **2006,** *239* (1), 83.

[120] Li, X.; Wang, H.; Robinson, J. T.; Sanchez, H.; Diankov, G.; Dai, H., Simultaneous Nitrogen Doping and Reduction of Graphene Oxide. *Journal of the American Chemical Society* **2009,** *131* (43), 15939.

[121] Iwazaki, T.; Obinata, R.; Sugimoto, W.; Takasu, Y., High oxygen-reduction activity of silk-derived activated carbon. *Electrochemistry Communications* **2009,** *11* (2), 376.

[122] Ozaki, J.-i.; Kimura, N.; Anahara, T.; Oya, A., Preparation and oxygen reduction activity of BN-doped carbons. *Carbon* **2007,** *45* (9), 1847.

[123] Sidik, R. A.; Anderson, A. B.; Subramanian, N. P.; Kumaraguru, S. P.; Popov, B. N., O2 Reduction on Graphite and Nitrogen-Doped Graphite: Experiment and Theory. *The Journal of Physical Chemistry B* **2006,** *110* (4), 1787.

[124] Sunarso, J.; Torriero, A. A. J.; Zhou, W.; Howlett, P. C.; Forsyth, M., Oxygen Reduction Reaction Activity of La-Based Perovskite Oxides in Alkaline Medium: A Thin-Film Rotating Ring-Disk Electrode Study. *J. Phys. Chem. C* **2012,** *116* (9), 5827.

[125] Singh, R. N.; Lal, B., High surface area lanthanum cobaltate and its A and B sites substituted derivatives for electrocatalysis of $O_2$ evolution in alkaline solution. *Int. J. Hydrogen Energy* **2002,** *27* (1), 45.

[126] Lee, D. U.; Park, H. W.; Higgins, D.; Nazar, L.; Chen, Z., Highly Active Graphene Nanosheets Prepared via Extremely Rapid Heating as Efficient Zinc-Air Battery Electrode Material. *J. Electrochem. Soc.* **2013,** *160* (9), F910.

[127] Liu, J. B.; Co, A. C.; Paulson, S.; Birss, V. I., Oxygen reduction at sol-gel derived $La_{0.8}Sr_{0.2}Co_{0.8}Fe_{0.2}O_3$ cathodes. *Solid State Ionics* **2006,** *177* (3-4), 377.

[128] Rousseau, S.; Loridant, S.; Delichere, P.; Boreave, A.; Deloume, J. P.; Vernoux, P., $La_{(1-x)}Sr_xCo_{1-y}Fe_yO_3$ perovskites prepared by sol-gel method: Characterization and relationships with catalytic properties for total oxidation of toluene. *Appl. Catal. B: Environ.* **2009,** *88* (3-4), 438.

[129] Park, H. W.; Lee, D. U.; Nazar, L. F.; Chen, Z., Oxygen Reduction Reaction Using MnO2 Nanotubes/Nitrogen-Doped Exfoliated Graphene Hybrid Catalyst for Li-$O_2$ Battery Applications. *J. Electrochem. Soc.* **2013,** *160* (2), A344.

[130] Wei, D.; Liu, Y.; Wang, Y.; Zhang, H.; Huang, L.; Yu, G., Synthesis of N-Doped Graphene by Chemical Vapor Deposition and Its Electrical Properties. *Nano Lett.* **2009,** *9* (5), 1752.

[131] Geng, D. S.; Chen, Y.; Chen, Y. G.; Li, Y. L.; Li, R. Y.; Sun, X. L.; Ye, S. Y.; Knights, S., High oxygen-reduction activity and durability of nitrogen-doped graphene. *Energy Environ. Sci.* **2011,** *4* (3), 760.

[132] Lee, J. H.; Paik, U.; Choi, J. Y.; Kim, K. K.; Yoon, S. M.; Lee, J.; Kim, B. K.; Kim, J. M.; Park, M. H.; Yang, C. W.; An, K. H.; Lee, Y. H., Dispersion stability of single-walled carbon nanotubes using Nafion in bisolvent. *J. Phys. Chem. C* **2007,** *111* (6), 2477.

[133] Liu, Y. Q.; Gao, L.; Sun, J.; Wang, Y.; Zhang, J., Stable Nafion-functionalized graphene dispersions for transparent conducting films. *Nanotechnology* **2009,** *20* (46).

[134] Lee, D. U.; Kim, B. J.; Chen, Z., One-pot synthesis of a mesoporous $NiCo_2O_4$ nanoplatelet and graphene hybrid and its oxygen reduction and evolution activities as an efficient bi-functional electrocatalyst. *J. Mater. Chem. A* **2013,** *1* (15), 4754.

[135] Liang, Y.; Li, Y.; Wang, H.; Zhou, J.; Wang, J.; Regier, T.; Dai, H., $Co_3O_4$ nanocrystals on graphene as a synergistic catalyst for oxygen reduction reaction. *Nat Mater* **2011,** *10* (10), 780.

[136] Ma, Y.; Sun, L.; Huang, W.; Zhang, L.; Zhao, J.; Fan, Q.; Huang, W., Three-Dimensional Nitrogen-Doped Carbon Nanotubes/Graphene Structure Used as a Metal-Free Electrocatalyst for the Oxygen Reduction Reaction. *J. Phys. Chem. C* **2011,** *115* (50), 24592.

[137] Park, H. W.; Lee, D. U.; Nazar, L. F.; Chen, Z., Oxygen Reduction Reaction Using $MnO_2$ Nanotubes/Nitrogen-Doped Exfoliated Graphene Hybrid Catalyst for Li-$O_2$ Battery Applications. *Journal of The Electrochemical Society* **2013,** *160* (2), A344.

[138] Wang, H.; Maiyalagan, T.; Wang, X., Review on Recent Progress in Nitrogen-Doped Graphene: Synthesis, Characterization, and Its Potential Applications. *Acs Catal.* **2012,** *2* (5), 781.

[139] Chew, S. Y.; Ng, S. H.; Wang, J.; Novak, P.; Krumeich, F.; Chou, S. L.; Chen, J.; Liu, H. K., Flexible free-standing carbon nanotube films for model lithium-ion batteries. *Carbon* **2009,** *47*, 2976

[140] Yu, A.; Park, H. W.; Davies, A.; Higgins, D. C.; Chen, Z.; Xiao, X., Free-Standing Layer-By-Layer Hybrid Thin Film of Graphene-$MnO_2$ Nanotube as Anode for Lithium Ion Batteries. *J. Phys. Chem. Lett.* **2011,** *2* (15), 1855.

[141] Choi, J.-Y.; Higgins, D.; Chen, Z., Highly Durable Graphene Nanosheet Supported Iron Catalyst for Oxygen Reduction Reaction in PEM Fuel Cells. *J. Electrochem. Soc.* **2011,** *159* (1), B86.

[142] Li, Y. L.; Wang, J. J.; Li, X. F.; Liu, J.; Geng, D. S.; Yang, J. L.; Li, R. Y.; Sun, X. L., Nitrogen-doped carbon nanotubes as cathode for lithium-air batteries. *Electrochem. Commun.* **2011,** *13* (7), 668.

[143] Sun, Y. Q.; Li, C.; Shi, G. Q., Nanoporous nitrogen doped carbon modified graphene as electrocatalyst for oxygen reduction reaction. *J. Mater. Chem.* **2012,** *22* (25), 12810.

[144] Duong, H. T.; Rigsby, M. A.; Zhou, W. P.; Wieckowski, A., Oxygen reduction catalysis of the $Pt_3Co$ alloy in alkaline and acidic media studied by x-ray photoelectron Spectroscopy and electrochemical methods. *J. Phys. Chem. C* **2007,** *111* (36), 13460.

[145] Lima, F. H. B.; Sanches, C. D.; Ticianelli, E. A., Physical characterization and electrochemical activity of bimetallic platinum-silver particles for oxygen reduction in alkaline electrolyte. *J. Electrochem. Soc.* **2005,** *152* (7), A1466.

[146] Cheng, F. Y.; Shen, J. A.; Peng, B.; Pan, Y. D.; Tao, Z. L.; Chen, J., Rapid room-temperature synthesis of nanocrystalline spinels as oxygen reduction and evolution electrocatalysts. *Nat. Chem.* **2011,** *3* (1), 79.

[147] Chen, Z.; Yu, A. P.; Ahmed, R.; Wang, H. J.; Li, H.; Chen, Z. W., Manganese dioxide nanotube and nitrogen-doped carbon nanotube based composite bifunctional catalyst for rechargeable zinc-air battery. *Electrochim. Acta* **2012,** *69*, 295.

[148] Hassan, F. M.; Chen, Z. W.; Yu, A. P.; Chen, Z.; Xiao, X. C., $Sn/SnO_2$ embedded in mesoporous carbon nanocomposites as negative electrode for lithium ion batteries. *Electrochim. Acta* **2013,** *87*, 844.

[149] Ma, G. X.; Zhao, J. H.; Zheng, J. F.; Zhu, Z. P., Synthesis of nitrogen-doped graphene and its catalytic activity for the oxygen reduction reaction in fuel cells. *New Carbon Mater.* **2012,** *27* (4), 258.

[150] Li, H.; Liu, H.; Jong, Z.; Qu, W.; Geng, D. S.; Sun, X. L.; Wang, H. J., Nitrogen-doped carbon nanotubes with high activity for oxygen reduction in alkaline media. *Int. J. Hydrogen Energy* **2011,** *36* (3), 2258.

[151] Kondo, S.; Nakamura, M.; Maki, N.; Hoshi, N., Active Sites for the Oxygen Reduction Reaction on the Low and High Index Planes of Palladium. *J. Phys. Chem. C* **2009,** *113* (29), 12625.